Measurement of the (e,e′) cross section for ^{12}C, ^{48}Ti, ^{27}Al and ^{40}Ar

Hongxia Dai

Dissertation submitted to the Faculty of the

Virginia Polytechnic Institute and State University

in partial fulfillment of the requirements for the degree of

Doctor of Philosophy

in

Physics

Camillo Mariani, Chair

Jean Heremans

Jonathan Link

Mark Pitt

August 30, 2019

Blacksburg, Virginia

Keywords: neutrino oscillation experiment, electron scattering

Copyright 2019, Hongxia Dai

Measurement of the (e,e′) cross section for ^{12}C, ^{48}Ti, ^{27}Al and ^{40}Ar

Hongxia Dai

(ABSTRACT)

Many experiments have found that neutrinos have three different flavors, and they can transform from each other. Each flavor is a mixture of three nonzero mass states. In neutrino oscillation experiments, the uncertainty of the extracted oscillation parameters is dependent on the neutrino-nucleus cross section. In recent years various experiments provided precise neutrino and anti-neutrino cross section measurements and they have shown the inability of current Monte Carlo simulations to reproduce the data. A more accurate nuclear structure model of the target employed in neutrino detector is urgently needed to improve the precision of long baseline neutrino experiments. Electron scattering has been one of the most powerful methods of obtaining information about cross sections in the past. In the upcoming deep underground neutrino experiment (DUNE), Liquid Argon Time Projection Chambers (LArTPCs) will be used as the detector technology and argon will be used as the nuclear target. There are very few data available on argon and there is not an accurate nuclear model that describes them accurately, at ∼5% level. We have performed an electron-argon scattering experiment at Jefferson Lab (E12-14-012) to provide accurate data that will help build a reliable nuclear model for describing neutrino-argon scattering.

The JLab E12-14-012 experiment has successfully taken data in Hall A at the Thomas Jefferson National Accelerator Facility between February and March of 2017. We collected data for the inclusive (e,e′) and exclusive (e,e′p) processes for a variety of targets (argon, titanium, aluminum, carbon) at a wide range of kinematic settings. This thesis will present the results of the inclusive double differential cross sections for carbon, titanium, aluminum and argon at beam energy $E = 2.222$ GeV and scattering angle $\theta = 15.541°$ with total uncertainties

smaller than 5%. The kinematic settings covered a broad range of energy transfers, including deep inelastic scattering (DIS), delta production, and quasielastic scattering.

Measurement of the (e,e′) cross section for ^{12}C, ^{48}Ti, ^{27}Al and ^{40}Ar

Hongxia Dai

(GENERAL AUDIENCE ABSTRACT)

In the upcoming deep underground neutrino experiment (DUNE), Liquid Argon Time Projection Chambers (LArTPCs) will be used as the detector technology, and argon will be used as the nuclear target. In order to reduce the systematic uncertainties on the extracted oscillation parameters, a more precise description of the argon nuclear structure is needed. Electron scattering has been one of the most powerful methods of studying the nuclear structure of a target. Therefore we performed an electron scattering experiment E12-14-012 in Hall A at the Thomas Jefferson National Accelerator Facility (Jefferson Lab). In the E12-14-012 experiment, we collected data for the inclusive (e,e′) and exclusive (e,e′p) processes for a variety of targets (argon, titanium, aluminum, carbon) at a wide range of kinematics. This thesis presents the measurements of the double differential cross sections for carbon, titanium, aluminum and argon at beam energy $E = 2.222$ GeV and scattering angle $\theta = 15.541°$.

Acknowledgments

First and foremost, I would like to express my sincere appreciation to my Advisor, Prof. Camillo Mariani, who has been providing precious guidance and support to me since the first day I started my PhD. I learned so much from our countless inspirational discussions, both on physics and technical details in programming.

I would also like to thank my committee members, including Prof. Mark Pitt, Prof. Jean Joseph Heremans, and Prof. Jonathan Link. The constructive discussions we had in the prelim and the pre-defense exams were very beneficial to strengthen my understandings in physics and my research topic, and their valuable encouragement and advice substantially built up my self-confidence in surviving my PhD.

It was a great honor for me to getting involved in the experiment in JLab. Mainly, I would like to thank Douglas Higinbotham for hosting me, showing me around and introducing the great tritium people to me.

I can still remember taking night shifts at JLab with Vishvas Pandey, a former postdoc member in my research group, and all the good conversations we had together. His help on my presentations and all the discussions we had is priceless.

I want to thank the argon collaboration. First Prof. Omar Benhar, who invited me to the NuInt workshop; and then Artur Ankowski, who always patiently answered my questions and provided a lot of help in the analysis. I also want to thank other graduate students: Daniel Abrams from UVa, Matt Murphy, and Linjie Gu at VT.

I would like to thank my dear colleagues and friends at JLab: Florian Hauenstein and R.Evan McClellan, who put great effort in our experiment and provided constructive advice; Jixie Zhang, my officemate at JLab who offered helpful discussions; Other graduate students, in-

cluding Dien Nguyen, Shujie Li, Hanjie Liu, Sheren Alsalmi, Nathaly Santiesteban, Tong Su, Tyler Hague, Mike Nycz, Jason Bane, and Longwu Ou, who were not only great coworkers but also great friends, with whom I shared great memories.

I would also like to thank my friends and officemates at VT: Lin Ju, Tianran Chen, Linghua Zhu, Shengchao Li, Tulasi Subedi, Joseph Hor, whose support and accompany I will never forget.

Finally, I want to say thank you to my parents and my cousin Jinjin Li, for their unconditional love and support. Special thanks to my boyfriend, Junkai Zeng, for all his love, encouragement, and company.

Contents

List of Figures **xi**

List of Tables **xviii**

1 Introduction **1**

1.1 Neutrino Oscillations 1

1.1.1 Two flavor oscillations 2

1.1.2 Three flavor oscillations 3

1.2 Neutrino oscillation experiments 5

1.2.1 Neutrino-nucleus cross section 8

1.2.2 Neutrino Energy Reconstruction 10

1.2.3 Past Experimental Oscillation Results 14

1.2.4 DUNE - Deep Underground Neutrino Experiment 15

1.3 Electron scattering 18

1.3.1 Inclusive cross section (e,e′) 19

1.3.2 Exclusive cross section (e,e′p) 22

1.3.3 PWIA - Plane Wave Impulse Approximation 26

1.3.4 DWIA - Distorted Wave Impulse Approximation 28

2 Experimental Setup **30**

2.1 Jefferson Lab Hall A - Overview 30

2.2 Hall A Beamline 31

2.2.1 Beam Energy Measurements 31

2.2.2 Beam Current Monitors 33

2.2.3 Beam Position Monitors 35

2.3 Target System 36

2.4 High Resolution Spectrometers (HRSs) 38

2.5 Detector Package 40

2.5.1 Vertical Drift Chambers 40

2.5.2 Scintillators 43

2.5.3 Gas Čerenkov 44

2.5.4 Lead Glass Calorimeter 45

2.6 Trigger Design 47

2.7 E12-14-012 Data Taking Summary 49

3 First Measurement of the Ti$(e, e')X$ Cross Section at JLab **51**

3.1 Introduction 51

3.2 Experimental Setup 54

3.3 Data Analysis 55

3.4 Experimental Results and Discussion 56

3.5 Summary and Conclusions 61

4 First Measurement of the Ar$(e, e')X$ Cross Section at JLab 64

4.1 Introduction 64

4.2 Experimental Setup 67

4.3 Data Analysis 68

4.4 Experimental Results and Sacling Analysis 70

4.5 Summary 76

5 Measurement of the cross sections for inclusive electron scattering in the E12-14-012 experiment at JLab 77

5.1 Introduction 77

5.2 Experimental Setup 81

5.3 Data Analysis 85

5.3.1 Yield-Ratio Method 85

5.3.2 Acceptance Method 85

5.4 Uncertainty Analysis 91

5.5 Experimental Results 94

5.6 Scaling and A-dependence 100

5.7 Summary and Conclusions 104

6 Summary **106**

Bibliography **107**

List of Figures

1.1 Contributions to the uncertainties in the Δm^2_{32}measurement in the $No\nu A$ [16] long baseline neutrino experiment. 7

1.2 Reconstructed neutrino energy distributions using the FG model and SF model. The plot on the top shows the results at $E_\mu = 600$ MeV and $\theta_\mu = 60°$, on the bottom is at $E_\mu = 1$ GeV and $\theta_\mu = 35°$ [5]. 12

1.3 1σ confidence regions of (θ_{13}, δ_{CP}) using data from simulation. The results are shown when the migration matrices accounting for 90%, 80%, and 70% of the missing energy, while the green area shows the case for all of the missing energy. The true values of θ_{13} and δ_{CP} are shown as the black dot in the center of the green area [30]. 13

1.4 Mass hierarchies: normal ordering (NO) and inverted ordering (IO) [7]. . . . 14

1.5 Schematic of the Deep Underground Neutrino Experiment [10]. 16

1.6 The top left plot shows the neutrino oscillation probability $P(\nu_\mu \to \nu_e)$ as a function of L and E_ν with $\delta_{CP} = 0$ and the mass hierarchy in normal ordering. The top right plot shows $P(\nu_\nu \to \nu_e)$ as a function of E_ν at a fixed baseline $L = 1,300$ km, for $\delta_{CP} = 0$, $-\pi/2$, and $\pi/2$. The bottom plots show the same probabilities but for antineutrinos $\bar{\nu}_\mu \to \bar{\nu}_e$ [10]. 17

1.7 The top left plot shows the neutrino oscillation probability $P(\nu_\mu \to \nu_e)$ as a function of L and E_ν with $\delta_{CP} = 0$ and the mass hierarchy in inverted ordering, the top right plot shows $P(\nu_\mu \to \nu_e)$ as a function of E_ν at a fixed baseline $L = 1,300$ km, for $\delta_{CP} = 0$, $-\pi/2$, and $\pi/2$. The bottom plots show the same probabilities but for antineutrinos $\bar{\nu}_\mu \to \bar{\nu}_e$ [10]. 18

1.8 General (e,e′) energy spectrum 20

1.9 A diagram of the (e,e′p) reaction 23

1.10 A diagram of the PWIA in (e,e′p) reaction [13]. 26

1.11 A diagram of the DWIA in (e,e′p) reaction [13]. 29

2.1 A picture of Hall A [15]. 31

2.2 The CEBAF ARC section [24]. 32

2.3 Schematic layout of the eP energy measurement system [17]. 33

2.4 Schematic diagram of the Hall A beam current monitor system. 34

2.5 Diagram of a BPM. Left view is along the beam axis [24]. 35

2.6 Design of the gas cell, units are in cm [27]. 36

2.7 A photo of the argon target installed on the standard Hall A cryogenic target ladder, at the bottom is the optical target, the Dummy target is right above the optical target. 37

2.8 Shell model structures of argon and titanium. 38

2.9 Picture of the Hall A target ladder system. 39

2.10 Schematic layout of the spectrometer magnet configuration (QQDQ) [17]. . . 40

2.11 Sideview of the detector stacks, on the top(bottom) is the left(right) arm. . . 41

2.12 Schematic diagram of the Hall A spectrometers VDCs [17]. 42

2.13 A typical VDC track example resulting in a five-cell event [22]. 43

2.14 Schematic of the S2m scintillator plane, only 6 out of 16 paddles are shown here. 44

2.15 A diagram showing the spherical mirrors and PMTs inside the Gas Čerenkov [29]. 46

2.16 Schematic layout of the calorimeters in both the LHRS and the RHRS [17]. . 47

2.17 Layout of the trigger design for the E12-14-012 experiment. 48

3.1 (color online). Comparison between the scaling function $F(y)$ obtained from the E12-14-012 data on C, represented by diamonds, and those obtained from the data of O'Connell *et al.* [65], Sealock *et al.* [66], and Day *et al.* [67]. The inset shows the momentum transfer dependence of $F(y)$ at fixed $y = -0.2$ GeV. The data sets are labeled by the value of Q^2 corresponding to the top of the quasielastic peak. 56

3.2 (color online). Double differential cross section for the C(e, e') process measured at beam energy of 2.222 GeV and scattering angle of 15.541 deg. The inner and outer uncertainty bars correspond to statistical and total uncertainties, respectively. The solid line represents the theoretical results obtained within the formalism described in Refs. [40, 42, 43, 72]. 58

3.3 (color online). Double differential cross section for the Ti(e, e') process measured at beam energy of 2.222 GeV and fixed scattering angle of 15.541 deg. The inner and outer uncertainty bars correspond to statistical and total uncertainties, respectively. The maximum uncertainties in the full kinematical range are provided. 60

3.4 (color online). Ratios defined by Eq.(5.6), computed using the measured carbon and titanium cross sections. 61

3.5 (color online). Comparison between the scaling function of 2nd kind, $f(\psi)$, obtained from the E12-14-012 data on C and Ti, represented by diamonds and circles, respsctively. The Fermi momentum of carbon has been fixed to the value obtained by Moniz *et al.* [75]. The data analysis for Ti sets the Ti Fermi momentum at ∼240 MeV. 62

4.1 (color online). Double differential cross section for the Ar(e, e') process, extracted with two different methods, at beam energy of 2.222 GeV and scattering angle of 15.541 deg. The inner and outer bars correspond to the statistical and total uncertainty, respectively. The dotted curve represents the quasielastic calculations obtained within the relativistic Green's function (RGF) formalism described in Ref. [85]. 69

4.2 (color online). Comparison of Ar(e, e') cross section of Fig. 4.1, and Ti(e, e') and C(e, e') cross sections of Ref. [83], all in the same kinematics, presented in terms of the ratio defined by Eq.(5.6). 72

4.3 (color online). Comparison between the scaling function of the second kind, $f(\psi)$, obtained from E12-14-012 data on Ar, Ti, and C. The k_F of C is fixed to the value obtained by Moniz *et al.* [75] while the data analysis of Ti and Ar sets k_F at 240 MeV and 245 MeV, respectively. The circles are the Ar data from LNF [35], which turn out to prefer an inconsistently higher value of k_F. 74

4.4 (color online). Comparison between the scaling function $F(y)$ obtained from the E12-14-012 data on argon, titanium and carbon, and the argon data obtained at LNF [35]. 75

5.1 (color online). Distribution along the beam direction of reconstructed events for the multi-foil carbon target. The shaded regions represent the data selected to identify the events coming from individual carbon foils. 88

5.2 (color online). Event yields from carbon foils at different positions along the beam direction, normalized to the yield for the central foil, for the uncorrected data and the Monte Carlo simulation. The dependence of the cross section on the scattering angle, correctly taken into account in the Monte Carlo simulation, introduces a linear trend in the data that needs to be corrected for. All uncertainties are purely statistical. 89

5.3 (color online). Event yields in the corrected data for the multi-foil carbon target surviving the z-position selection, normalized to the yield for the central foil. The outcomes of two correction procedures are compared. The error bars are symmetric and represent the total uncertainties, being the statistical and systematic uncertainties added in quadrature. 90

5.4 (color online). Double-differential cross section extracted for inclusive electron scattering off the Al-7075 target at beam energy 2.222 GeV and scattering angle 15.54°. The inner and outer uncertainty bands correspond to statistical and total uncertainties, respectively. 94

5.5 (color online). Comparison of the Al(e, e') cross sections extracted using the yield-ratio and acceptance methods. The inner (outer) bands for the yield-method show statistical (total) uncertainties. For the acceptance method only statistical uncertainties are shown. 95

5.6 (color online). Comparison of the cross sections per nucleon for aluminum, argon [92], titanium [83], and carbon [83] measured at beam energy 2.222 GeV and scattering angle 15.54°. The average nucleon number for every target is calculated according to the natural abundances of isotopes, see details in the text. The bands represent the total uncertainties. 97

5.7 (color online). Same as in Fig. 5.6 but for the cross sections normalized by the combination of the elementary cross sections according to Eq. (5.6). . . . 98

5.8 (color online) Comparison between the scaling function of aluminum obtained from the E12-14-012 data (this work), represented by diamonds, and those obtained from the data of Day *et al.* [67]. The data are labeled according to the value of Q^2 corresponding to quasi elastic kinematics. 101

5.9 (color online) Q^2-dependence of the scaling functions $F(y, Q^2)$ obtained from the cross section displayed in Fig. 5.4 and from the data reported in Ref. [67]. The meaning of the symbols is the same as in Fig. 5.8. 102

5.10 (color online) Scaling functions of second kind, obtained from the inclusive cross sections measured by the E12-14-012 experiment using carbon, aluminum, argon and titanium targets. 103

List of Tables

1.1 Best fit values of the 3ν oscillation parameters obtained from a global analysis from Ref. [8]. The latter column shows the formal "1σ accuracy" for each parameter, defined as 1/6 of the 3σ range divided by the best-fit value (in percent). 15

2.1 Main characteristics of the Hall A HRSs [17]. 39

2.2 Data taking summary 49

2.3 Kinematic settings for (e,e′p) measurements, the central kinematic variables include beam energy (E_e), central momenta ($E_{e'}$, P_p), central angles (θ_e, θ_p), momentum transfer ($|\vec{q}|$) and central missing momentum (p_m). 50

2.4 Kinematic settings for (e,e′) measurements, the central kinematic variables include beam energy (E_e),central momentum ($E_{e'}$), central angle (θ_e). . . . 50

3.1 Contributions to the uncertainties associated with the measured C(e, e') cross sections. Numbers represents upper limit or range for the uncertainties that vary between kinematical regions. 57

4.1 Uncertainties associated with the presented Ar(e, e') cross section. Numbers represent upper limits or the range for the uncertainties that vary between different kinematical regions. 71

5.1 Composition of the Al-7075 alloy. For each element, we provide the number of protons Z and the average number of neutrons N calculated according to the isotopic abundances [93]. 83

5.2 Contributions to systematic uncertainties in the yield-ratio method for aluminum and argon. 92

Chapter 1

Introduction

In this chapter, we briefly review the basic theory on neutrino oscillations and the electron and neutrino scattering theory. In part one we will review the two-flavor and three-flavor neutrino oscillations, in part two we will describe the neutrino-nucleus cross section theory and we will present a summary of the results from the neutrino oscillation experiments performed in the past few decades. In part three we will describe and characterize the electron scattering processes.

1.1 Neutrino Oscillations

Neutrinos are one of the elementary particles in nature. In the standard model of particle physics(SM), neutrinos are described as neutrally-charged and extremely light particles that come in three different flavors, ν_e, ν_μ, and ν_τ, corresponding to three types of charged leptons, electron, muon, and tau, respectively. For a long time, neutrinos have been assumed to be massless and travel at the speed of light [1, 2]. Previous experimental results aiming at searching the mass of neutrinos, including β-decay experiments, as well as cosmological observation, set up the upper limit of neutrino mass to be smaller than 2 eV [6]. However, neutrino oscillation, which mixes neutrino mass eigenstates and flavor eigenstates, has been observed in a series of experiments, which is a sign that neutrinos have finite masses.

1.1.1 Two flavor oscillations

A 2-neutrino oscillation model is a useful approximation of the more generic 3-neutrino oscillation, where only one mass splitting and one mixing angle are involved. The weak (flavor) eigenstates can be denoted by $|\alpha\rangle$ and $|\beta\rangle$. The two mass eigenstates, indicated by $|1\rangle$ and $|2\rangle$, can be viewed as the mixture of weak eigenstates. Generically, the relationship between the two eigenstates can be written by the linear equation below:

$$\begin{pmatrix} |\nu_\alpha\rangle \\ |\nu_\beta\rangle \end{pmatrix} = \begin{pmatrix} \cos\theta & \sin\theta \\ -\sin\theta & \cos\theta \end{pmatrix} \begin{pmatrix} |\nu_1\rangle \\ |\nu_2\rangle \end{pmatrix} = U \begin{pmatrix} |\nu_1\rangle \\ |\nu_2\rangle \end{pmatrix}, \tag{1.1}$$

where U is the mixing matrix and θ is the mixing angle.

Consider the mass eigenstates $|\nu_k\rangle (k = 1, 2)$ with mass m_k, momentum p and energy $E_k = \sqrt{p^2 + m_k^2}$. In the Schrödinger picture, we have

$$|\nu_k(t)\rangle = e^{-iE_k t}|\nu_k(0)\rangle. \tag{1.2}$$

The oscillation probability $P(\nu_\alpha \to \nu_\beta)$ can be therefore calculated from the square of the quantum mechanical amplitude

$$\begin{aligned} P(\nu_\alpha \to \nu_\beta) &= |\langle\nu_\alpha(0)|\nu_\beta(t)\rangle|^2 \\ &= |-\sin\theta\cos\theta(e^{-iE_1 t} - e^{-iE_2 t})|^2 \\ &= \sin^2(2\theta)\sin^2\left(\frac{E_2 - E_1}{2}t\right) \end{aligned} \tag{1.3}$$

Since the mass of the neutrino is tiny compared to the kinetic energy, we at this moment

use the relativistic approximation, $E_k \approx p + \frac{m_k^2}{2p}$. Thus, Eq. (1.12) becomes

$$P(\nu_\alpha \to \nu_\beta) = \sin^2(2\theta)\sin^2\left(\frac{\Delta m^2}{4p}t\right), \tag{1.4}$$

where $\Delta m^2 = |m_1^2 - m_2^2|$.

Since the neutrinos travel approximately at the speed of light, we could continue the approximation by using $p \approx E$ and the travel distance $L \approx t$, where we have already let $c = 1$:

$$P(\nu_\alpha \to \nu_\beta) = \sin^2(2\theta)\sin^2\left(\Delta m^2 \frac{L}{4E}\right). \tag{1.5}$$

Since in the above discussion we have used natural units, to put the formula into practical use we shall convert it by substitute $\hbar c$ with 197 eV·nm, so that the equation becomes

$$P(\nu_\alpha \to \nu_\beta) = \sin^2(2\theta)\sin^2\left(1.27\Delta m^2 \frac{L}{E}\right). \tag{1.6}$$

where L is in meters, E is in MeV, and Δm^2 is in eV^2.

1.1.2 Three flavor oscillations

In the more generic scenario, we need a 3-neutrino oscillation model. The underlying theory describing the 3-neutrino oscillation model was first proposed by Pontecorvo in 1957 [3] and later developed by Maki, Nakagawa, and Sakata in a more formal way in 1962 [4]. In this model, $|\nu_\alpha\rangle$ and $|\nu_k\rangle$ where $\alpha \in \{e, \mu, \tau\}$ and $i \in \{1, 2, 3\}$, namely the flavor and mass eigenstates, respectively, are related by

$$|\nu_\alpha\rangle = \sum_k U_{\alpha k}|\nu_k\rangle \tag{1.7}$$

where the mixing matrix U, known as the "PMNS matrix", can be generally expressed as the form:

$$\begin{pmatrix} c_{12}c_{13} & c_{13}s_{12} & e^{-i\delta}s_{13} \\ -c_{23}s_{12} - e^{i\delta}c_{12}s_{13}s_{23} & c_{12}c_{23} - e^{i\delta}s_{12}s_{13}s_{23} & c_{13}s_{23} \\ s_{12}s_{23} - e^{i\delta}c_{12}c_{23}s_{13} & -e^{i\delta}c_{23}s_{12}s_{13} - c_{12}s_{23} & c_{13}c_{23} \end{pmatrix} \tag{1.8}$$

Here δ is the CP-violating phase, and c_{ij} and s_{ij} are abbreviations of $\cos\theta_{ij}$ and $\sin\theta_{ij}$ functions, where θ_{ij} $(i, j = 1, 2, 3)$ are mixing angles. Using Eq. (1.2) we can write Eq. (1.7) as

$$|\nu_\alpha(t)\rangle = \sum_k U_{\alpha k}e^{-iE_k t}|\nu_k(0)\rangle \tag{1.9}$$

In order to determine the oscillation probability $P(\nu_\beta \to \nu_\alpha)$, we can first write Eq. (1.7) as

$$|\nu_k(0)\rangle = \sum_\beta U^*_{\beta k}|\nu_\beta(0)\rangle, \tag{1.10}$$

and using Eq. (1.10) and Eq. (1.11), we derive:

$$\begin{aligned} |\nu_\alpha(t)\rangle &= \sum_{k,\beta} U_{\alpha k}e^{-iE_k t}U^*_{\beta k}|\nu_\beta(0)\rangle \\ &= e^{-ipt}\sum_{k,\beta} U_{\alpha k}e^{-i\frac{m_k^2}{2p}t}U^*_{\beta k}|\nu_\beta(0)\rangle \end{aligned} \tag{1.11}$$

where the relativistic approximation $E_k \approx p + \frac{m_k^2}{2p}$ is used.

Then the oscillation probability can be cast as follows:

$$
\begin{aligned}
P(\nu_\beta \to \nu_\alpha) &= |\langle \nu_\beta(0)|\nu_\alpha(t)\rangle|^2 \\
&= |\sum_i U_{\alpha k} e^{-i\frac{m_k^2}{2p}t} U^*_{\beta k}|^2 \\
&= Re \sum_{k,j} U^*_{\alpha k} U_{\beta k} U_{\alpha k} U^*_{\beta k} e^{-i\frac{m_k^2 - m_j^2}{2p}t} \\
&= \delta_{\alpha\beta} - Re \sum_{k,j} U^*_{\alpha k} U_{\beta k} U_{\alpha k} U^*_{\beta k} \left(1 - e^{-i\frac{\Delta m_{kj}^2}{2p}t}\right) \\
&= \delta_{\alpha\beta} - 4 \sum_{k>j} U^*_{\alpha k} U_{\beta k} U_{\alpha k} U^*_{\beta k} \sin^2\left(\frac{\Delta m_{kj}^2}{4p} t\right),
\end{aligned}
\tag{1.12}
$$

where the travel distance L is approximately equal to the time period t in natural unit:

$$
P(\nu_\beta \to \nu_\alpha) = \delta_{\alpha\beta} - 4 \sum_{k>j} U^*_{\alpha k} U_{\beta k} U_{\alpha k} U^*_{\beta k} \sin^2\left(\frac{\Delta m_{kj}^2 L}{4p}\right). \tag{1.13}
$$

1.2 Neutrino oscillation experiments

The neutrino oscillation formula (Eq. (1.13)) can be used to extract the oscillation parameters. Long and short baseline neutrino oscillation experiments typically measure the oscillation probability by comparing the neutrino event rates between a near and a far detector. There are two types of oscillation searches, ”appearance” and ”disappearance”. An ”appearance” experiment looks, for example, for the appearance of ν_e or ν_τ in a pure ν_μ beam, while a ”disappearance” experiment searches for a ν_μ flux suppression between the near and the far detectors. For a $\nu_\alpha \to \nu_\beta$ oscillation, the event rates at near and far detectors can be

written as the following [81]:

$$N^{\alpha}_{\mathrm{ND}}(\boldsymbol{p}_{\mathrm{reco}}) = \sum_i \phi_\alpha(E_{\mathrm{true}}) \times \sigma^i_\alpha(\boldsymbol{p}_{\mathrm{true}}) \times \epsilon_\alpha(\boldsymbol{p}_{\mathrm{true}}) \times R_i(\boldsymbol{p}_{\mathrm{true}}; \boldsymbol{p}_{\mathrm{reco}}) \tag{1.14}$$

$$N^{\alpha\to\beta}_{\mathrm{FD}}(\boldsymbol{p}_{\mathrm{reco}}) = \sum_i \phi_\alpha(E_{\mathrm{true}}) \times P_{\alpha\beta}(E_{\mathrm{true}}) \times \sigma^i_\beta(\boldsymbol{p}_{\mathrm{true}}) \times \epsilon_\beta(\boldsymbol{p}_{\mathrm{true}}) \times R_i(\boldsymbol{p}_{\mathrm{true}}; \boldsymbol{p}_{\mathrm{reco}}). \tag{1.15}$$

Here $N^{\alpha}_{\mathrm{ND}}(\boldsymbol{p}_{\mathrm{reco}})(N^{\alpha}_{\mathrm{FD}}(\boldsymbol{p}_{\mathrm{reco}}))$ represents the event rate at the near (far) detector as a function of the reconstructed variable $\boldsymbol{p}_{\mathrm{reco}} \equiv (E_{\mathrm{reco}}, \vec{p}_{\mathrm{reco}})$, ϕ_α is the flux of α neutrino at the near detector, $P_{\alpha\beta}(E_{\mathrm{true}})$ is the oscillation probability, σ^i_α is the neutrino cross section for flavor α at interaction i, ϵ_α is the detector efficiency for a neutrino of flavor α interacting in the detector, and $R_i(\boldsymbol{p}_{\mathrm{true}}; \boldsymbol{p}_{\mathrm{reco}})$ is the probability that an event with $\boldsymbol{p}_{\mathrm{true}}$ is reconstructed with a different value of its momentum ($\boldsymbol{p}_{\mathrm{reco}}$) due to nuclear or detector effects.

The oscillation probability $P(\nu_\alpha \to \nu_\beta)$ can be calculated by simply taking the ratio of Eq. (1.15) and Eq. (1.14), knowing the distance L between the far and near detectors. However, since neutrinos are neutrally charged and extremely light, we can not measure the neutrino energy E directly, instead, we reconstruct the neutrino energy using the information of the particles created by the interactions of the neutrinos and the detector target. More details of the neutrino energy reconstruction will be described in Sec. (1.2.2). One important remark is that event rate here means the convolution of neutrino flux, cross sections, detector effects and all of those are strongly dependent upon the neutrino energy. Once we have the ratio of events as function of the reconstructed neutrino energy, we can extract the oscillation parameters θ and Δm^2. Cross section uncertainties are a great source of uncertainty in the oscillation measurements (see Fig. 1.1) because they will change substantially how well the neutrino energy is reconstructed, nuclear effects can modify the number and energy of the particles reconstructed in final state. Therefore the uncertainties of the extracted oscillation parameters can be effectively reduced if we can build a more accurate neutrino-nucleus cross

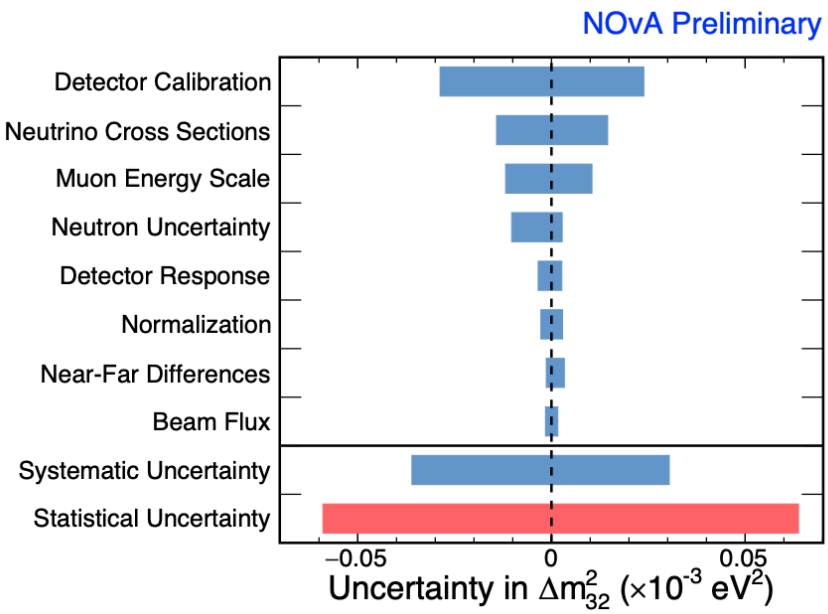

Figure 1.1: Contributions to the uncertainties in the Δm^2_{32}measurement in the $NO\nu A$ [16] long baseline neutrino experiment.

section model and therefore reconstruct the neutrino energy more precisely.

The upcoming neutrino oscillation experiment DUNE (Deep Underground Neutrino Experiment) will use a LArTPC (Liquid Argon Time Projection Chamber) with a mass of 40 kton [11], and argon as the neutrino target. Argon is a non-isospin symmetric nucleus (numbers of protons and neutrons are not the same) and currently there is not a reliable cross section model for argon, thus we performed an electron scattering experiment at Jefferson Lab, the E12-14-012 experiment. The E12-14-012 data will provide the benchmark to develop and test new nuclear models. Electron and neutrino scattering are very similar. The vector part of the current is the same but neutrino scattering also has a component from the axial part of the current. Performing an electron scattering experiment will allow to measure the vector part of the current, while the axial can be either computed theoretically or measured using neutrino scattering experiments like MicroBooNE. We will describe electron and neutrino scattering in more details in the following.

1.2.1 Neutrino-nucleus cross section

In charge-current neutrino-nucleus interaction, the interaction process can be written as

$$\nu_\ell(k) + A(p) \to \ell^-(k') + X(p') \ , \tag{1.16}$$

where a neutrino ν_ℓ scatters off a nuclear target A, and in the final state, there is an outgoing lepton ℓ and a hadronic state X. The four-momenta can be defined as

$$k = (E_\nu, \mathbf{k}), k' = (E_\ell, \mathbf{k}'), p = (E_p, \mathbf{p}), p' = (E_{p'}, \mathbf{p}'). \tag{1.17}$$

The double differential cross section of the process can then be written in the form [30, 40, 41, 44]

$$\frac{d^2\sigma}{d\Omega_\ell dE_\ell} = \frac{G_F^2\, V_{ud}^2}{16\,\pi^2}\,\frac{|\mathbf{k}_\ell|}{|\mathbf{k}_\nu|}\,L_{\lambda\mu}\,W^{\lambda\mu} \ , \tag{1.18}$$

where G_F is the Fermi constant, and $|V_{ud}|$ is the coupling of the quarks u and d in the Cabibbo-Kobayashi-Maskawa (CKM) matrix V. $L_{\lambda\mu}$ and $W^{\lambda\mu}$ are respectively the leptonic tensor and hadronic tensor. The leptonic tensor can be defined as

$$L_{\lambda\mu} = 8(k_\ell^\lambda k_\nu^\mu + k_\mu^\lambda k_\ell^\nu - g^{\lambda\mu} k_\ell \cdot k_\nu - i\epsilon^{\lambda\mu\alpha\beta} k_{\ell\beta} k_{\nu\alpha}), \tag{1.19}$$

where all masses of leptons are neglected. $g_{\lambda\nu}$ is the metric tensor and $\epsilon_{\lambda\nu\alpha\beta}$ is the fully antisymmetric Levi-Civita tensor. The hadronic tensor is defined by

$$W^{\lambda\nu} = \sum_X \frac{1}{2E_p} \langle 0(p)|J^\lambda|X(p')\rangle\langle X(p')|J^\nu|0(p)\rangle \delta((p+q)^2 - m_N'^2), \tag{1.20}$$

where m'_N is the mass of the final state and q is the four-momentum transferred, $q = p' - p$. In the most general case, $W_{\lambda\nu}$ can be written as a function of five different structure functions [30]:

$$W^{\lambda\mu} = -g^{\lambda\mu}W_1 + \frac{p^\lambda p^\mu}{m_N^2}W_2 - i\epsilon^{\lambda\mu\varrho\sigma}\frac{p_\varrho q_\sigma}{m_N^2}W_3 + \frac{q^\lambda q^\mu}{m_N^2}W_4 + \frac{p^\lambda q^\mu + q^\lambda p^\mu}{m_N^2}W_5 \ . \tag{1.21}$$

From Eq. (1.19) and Eq. (1.21), we obtain [44]

$$L^{\lambda\mu}W_{\lambda\mu} = 16\sum_i W_i\left(\frac{A_i}{m_N^2}\right), \tag{1.22}$$

where the A_i's are:

$$\begin{aligned}
A_1 &= m_N^2(k\cdot k'),\\
A_2 &= (k\cdot p)(k'\cdot p) - \frac{A_1}{2},\\
A_3 &= (k\cdot p)(k'\cdot q) - (k\cdot q)(k'\cdot p),\\
A_4 &= (k\cdot q)(k'\cdot q) - \frac{q^2}{2}\frac{A_1}{m_N^2},\\
A_5 &= (k\cdot p)(k'\cdot q) + (k'\cdot p)(k\cdot q) - (q\cdot p)\frac{A_1}{m_N^2},
\end{aligned} \tag{1.23}$$

in the quasi-elastic channel, the structure functions W_i's are given by :

$$\begin{aligned} W_1 &= 2[F_A^2(1+\tau) + \tau(F_1+F_2)^2], \\ W_2 &= 2[F_A^2 + F_1^2 + \tau F_2^2], \\ W_3 &= 2[F_A(F_1+F_2)], \\ W_4 &= [F_2^2(1+\tau) - 2F_2(F_1+F_2)]/2, \\ W_5 &= W_2/2, \end{aligned} \tag{1.24}$$

with $\tau = \frac{-q^2}{4m_N^2}$, where F_1 and F_2 are vector form factors, and F_A is the axial-vector form factor. Ref. [44] contains a more detail and complete derivation of the above equations.

The expressions for the structure functions for the resonance production and deep inelastic scattering channels can be found in Ref. [30].

1.2.2 Neutrino Energy Reconstruction

In neutrino oscillation experiments, in order to extract the oscillation parameters, the neutrino energy needs to be reconstructed event by event since the neutrino beam is not monochromatic. Neutrinos are produced by 3-body decay of charged pions and kaons, that are respectively produced by interactions of the proton beam with the neutrino target. A pulsing magnetic field (horn) focus positively(negatively) charged pions and defocus negatively(positively) charged pions in case of the neutrino(antineutrino) beam. As a result the energy spectrum of a neutrino beam is quite broad. The neutrino energy can be determined by measuring the kinematics of the outgoing particles.

Consider the simplest case, the charged current quasielastic scattering (CCQE) of a neutrino

off a nuclear target

$$\nu_\ell + A \rightarrow \ell^- + X \ , \tag{1.25}$$

where a neutrino with four momentum $k = (E_\nu, \mathbf{k})$ scatters off a nuclear target A, and in the final state, there is an outgoing lepton with four momentum $k' = (E_\ell, \mathbf{k}')$ and an hadronic state X.

By applying the energy and momentum conservations, the kinematic energy reconstruction for charged current quasielastic (CCQE) is given by [81]

$$E_\nu = \frac{m_p^2 - m_\ell^2 - E_n^2 + 2E_\ell E_n - 2\mathbf{k}_n \cdot \mathbf{p}_n + |\mathbf{p}_n^2|}{2(E_n - E_\ell + |\mathbf{k}_\ell| \cos\theta_\ell - |\mathbf{p}_n| \cos\theta_n)}, \tag{1.26}$$

where $|\mathbf{k}_\ell|$ and $|\theta_\ell|$ can be measured by detectors and $\mathbf{p}_n$ and E_n are the unknown momentum and energy of the interacting neutrons.

The spectral function $P(P_m, E_m)$ describes the probability of finding a nucleon with initial momentum P_m and energy E_m in the nucleus. In order to obtain accurate incoming neutrino and antineutrino energies, measuring the spectral function of the target nucleus and get the energy and momentum distributions of protons and neutrons, is significantly important.

The existing simulation codes use the following approximation:

$$|p_n| = 0, E_n = m_n - \epsilon, \tag{1.27}$$

or the Fermi Gas (FG) model. In the FG model, each nucleon is regarded as isolated and does not interact with other nucleons. The initial momentum of all nucleons is uniformly distributed and less than the Fermi momentum K_F. The removal energy is considered constant. Both K_F and the removal energy depend on the target nucleus.

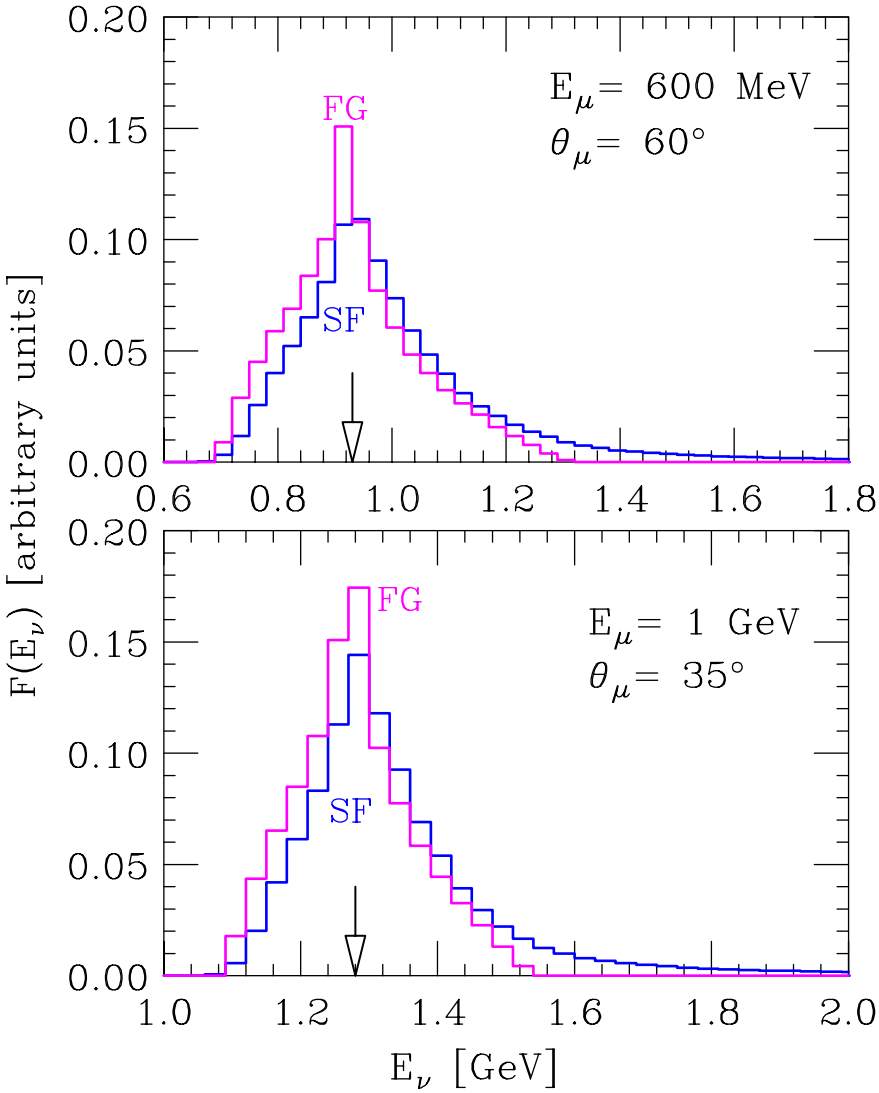

Figure 1.2: Reconstructed neutrino energy distributions using the FG model and SF model. The plot on the top shows the results at $E_\mu = 600$ MeV and $\theta_\mu = 60°$, on the bottom is at $E_\mu = 1$ GeV and $\theta_\mu = 35°$ [5].

In the Spectral Function (SF) model, the nucleon-nucleon (N-N) interaction is included therefore the momentum distribution is not a step function like in the FG model, the removal energy is correlated to the initial momentum of nucleons and hence not a constant.

In Fig. 1.2, the neutrino energy is reconstructed from Eq. (1.26) using 2×10^4 $(|\mathbf{p}_n|, E_n)$ values sampled from the probability distributions associated with the SF model and FG

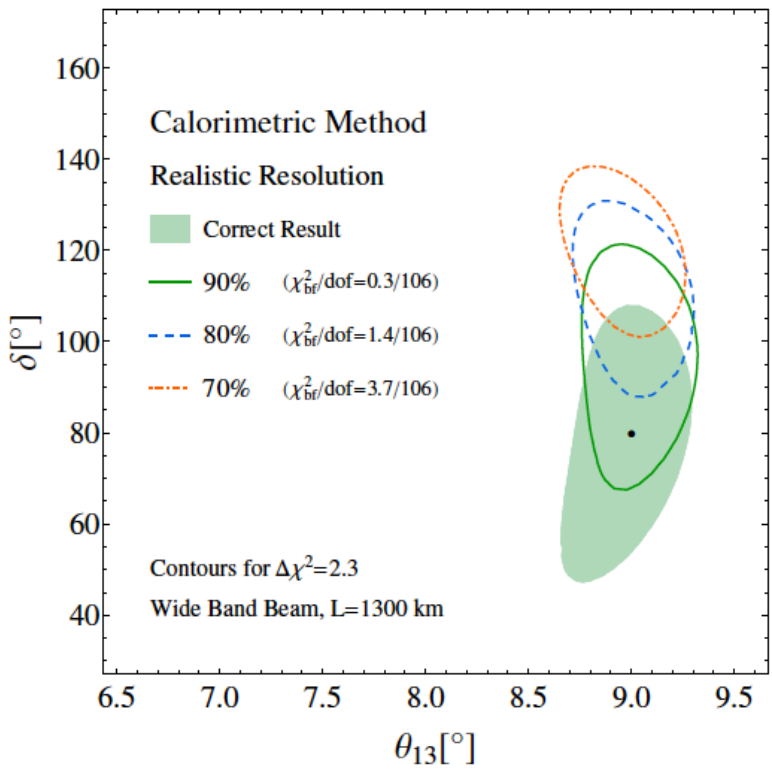

Figure 1.3: 1σ confidence regions of (θ_{13}, δ_{CP}) using data from simulation. The results are shown when the migration matrices accounting for 90%, 80%, and 70% of the missing energy, while the green area shows the case for all of the missing energy. The true values of θ_{13} and δ_{CP} are shown as the black dot in the center of the green area [30].

model of oxygen. In the top plot of Fig. 1.2, $E_\mu = 600$ MeV and $\theta_\mu = 60°$, the average reconstructed neutrino energy using the SF model is shifted to higher energy by ~ 20 MeV, while in the plot on bottom of Fig. 1.2 with $E_\mu = 1$ GeV, the shift is bigger, $\sim$70 MeV or 10% [5].

Figure 1.3 shows for a DUNE-like experiment, that if the reconstructed neutrino energy is underestimated by $\sim$ 20%, there would be a significant bias in the extracted δ_{CP} phase. With a 30% energy underestimation, the extracted δ_{CP} would exclude the true value at a confidence level between 2 and 3σ [30].

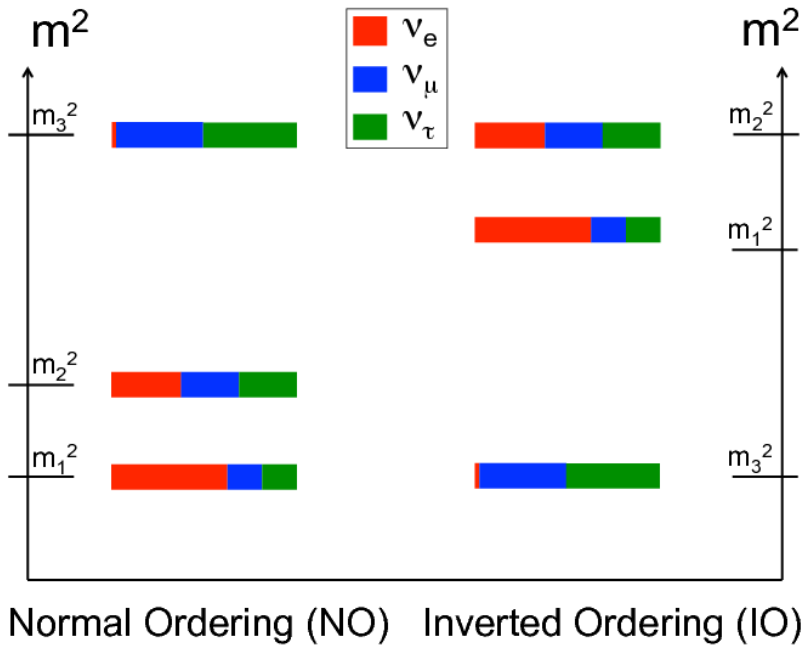

Figure 1.4: Mass hierarchies: normal ordering (NO) and inverted ordering (IO) [7].

1.2.3 Past Experimental Oscillation Results

Table 1.1 shows the global fit results of the oscillation parameters. This analysis used various data sets, including solar and long-baseline reactor neutrinos, long-baseline accelerator neutrinos, short-baseline reactor neutrinos, and atmospheric neutrinos [8].

In Table (1.1), the δm^2 and Δm^2 are defined as

$$\delta m^2 = m_2^2 - m_1^2 > 0, \Delta m^2 = m_3^2 - \frac{m_1^2 + m_2^2}{2}, \tag{1.28}$$

since oscillation experiments can only determine the squared difference of the neutrino masses, so there are two possible mass hierarchies, if $\Delta m^2 > 0$, we call it normal ordering (NO), otherwise inverted ordering (IO). OI and IO are shown in Fig. 1.4.

Table 1.1: Best fit values of the 3ν oscillation parameters obtained from a global analysis from Ref. [8]. The latter column shows the formal "1σ accuracy" for each parameter, defined as 1/6 of the 3σ range divided by the best-fit value (in percent).

Parameter	Ordering	Best fit	1σ range	2σ range	3σ range	"1σ" (%)
$\delta m^2/10^{-5}$ eV^2	NO	7.34	7.20 – 7.51	7.05 – 7.69	6.92 – 7.91	2.2
	IO	7.34	7.20 – 7.51	7.05 – 7.69	6.92 – 7.91	2.2
$\sin^2\theta_{12}$	NO	3.04	2.91 – 3.18	2.78 – 3.32	2.65 – 3.46	4.4
	IO	3.03	2.90 – 3.17	2.77 – 3.31	2.64 – 3.45	4.4
$\sin^2\theta_{13}/10^{-2}$	NO	2.14	2.07 – 2.23	1.98 – 2.31	1.90 – 2.39	3.8
	IO	2.18	2.11 – 2.26	2.02 – 2.35	1.95 – 2.43	3.7
$\lvert\Delta m^2\rvert/10^{-3}$ eV^2	NO	2.455	2.423 – 2.490	2.390 – 2.523	2.355 – 2.557	1.4
	IO	2.441	2.406 – 2.474	2.372 – 2.507	2.338 – 2.540	1.4
$\sin^2\theta_{23}/10^{-1}$	NO	5.51	4.81 – 5.70	4.48 – 5.88	4.30 – 6.02	5.2
	IO	5.57	5.33 – 5.74	4.86 – 5.89	4.44 – 6.03	4.8
δ/π	NO	1.32	1.14 – 1.55	0.98 – 1.79	0.83 – 1.99	14.6
	IO	1.52	1.37 – 1.66	1.22 – 1.79	1.07 – 1.92	9.3

1.2.4 DUNE - Deep Underground Neutrino Experiment

The DUNE [11] experiment is the next big US long baseline neutrino experiment. DUNE will focus on neutrino science, nucleon decay, and supernova physics. Over 1,200 collaborators from over 30 countries are involved in this experiment. It is hosted by the Fermi National Accelerator Laboratory (Fermilab) and it is currently under construction. It is expected to start taking data in 2026.

DUNE will use a two neutrino detectors setup. The near detector will be installed at the Fermilab, while a much larger far detector will be located 4,850 feet underground at the Sanford Laboratory, which is 1,300 km far from Fermilab (see Fig. 1.5). The near detector will provide measurements of the neutrino flux, neutrino energy, and the neutrino cross sections on a variety of targets. The far detector will use a Liquid Argon Time Projection Chamber (LArTPC), which can (1) provide high precision identification of neutrino flavors, (2) enable to find CP violation, and (3) advance proton-decay lifetime limits [10, 11].

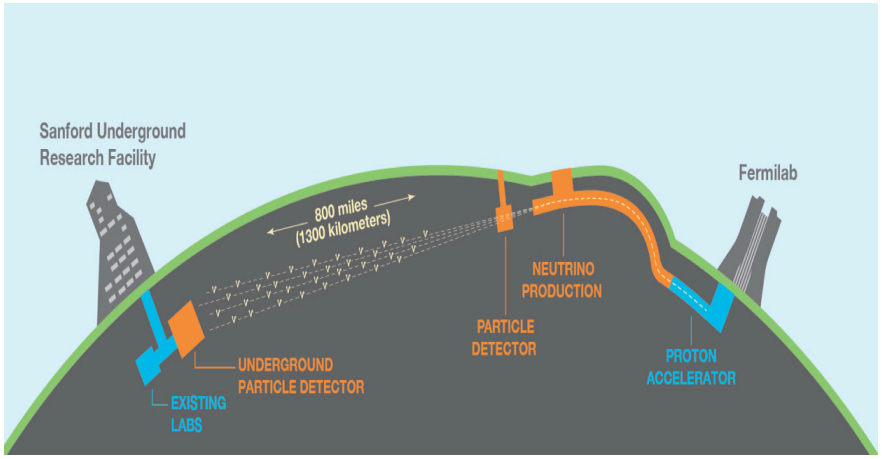

Figure 1.5: Schematic of the Deep Underground Neutrino Experiment [10].

The Long-Baseline Neutrino Facility will provide the neutrino beamline for DUNE, and the beamline can generate a muon neutrino/antineutrino beam with wide-band and high-purity, the proton energy will spread from 60 to 120 GeV, corresponding to a neutrino energy between 1 and 8 GeV.

DUNE will be able to perform many high precision measurements. For example, by measuring the $\nu_\mu \to \nu_e$ and $\bar{\nu_\mu} \to \bar{\nu_e}$ oscillation probabilities, DUNE can provide precision measurement of the third mixing angle θ_{13}, measurement of the charge-parity (CP) violation phase δ_{CP}, and determination of the sign of Δm^2_{31}. In addition, the mixing angle θ_{23} and the value of the mass difference $|\Delta m^2_{32}|$ will be determined in $\nu_\mu \to \nu_{e,\mu}$ oscillations [10, 11].

The CP violation phase δ_{CP} will be measured through the "appearance" searches, and we will look for oscillations of $\nu_\mu \to \nu_e$ and $\bar{\nu}_\mu \to \bar{\nu}_e$. We will not measure the $\nu_\mu \to \nu_\tau$ or $\bar{\nu}_\mu \to \bar{\nu}_\tau$ because it's difficult to detect ν_τ's. Observation of an asymmetry between the oscillation probabilities $P(\nu_\mu \to \nu_e)$ and $P(\bar{\nu}_\mu \to \bar{\nu}_e)$ will imply CP violation. Recall that the oscillation probability depends on E_ν and the baseline L. For the DUNE with a fixed baseline of $L = 1,300$ km, the dependences of the oscillation probability on E_ν are shown on the right in Fig. 1.6 and 1.7, different colors are for different values of δ_{CP} [10]. The

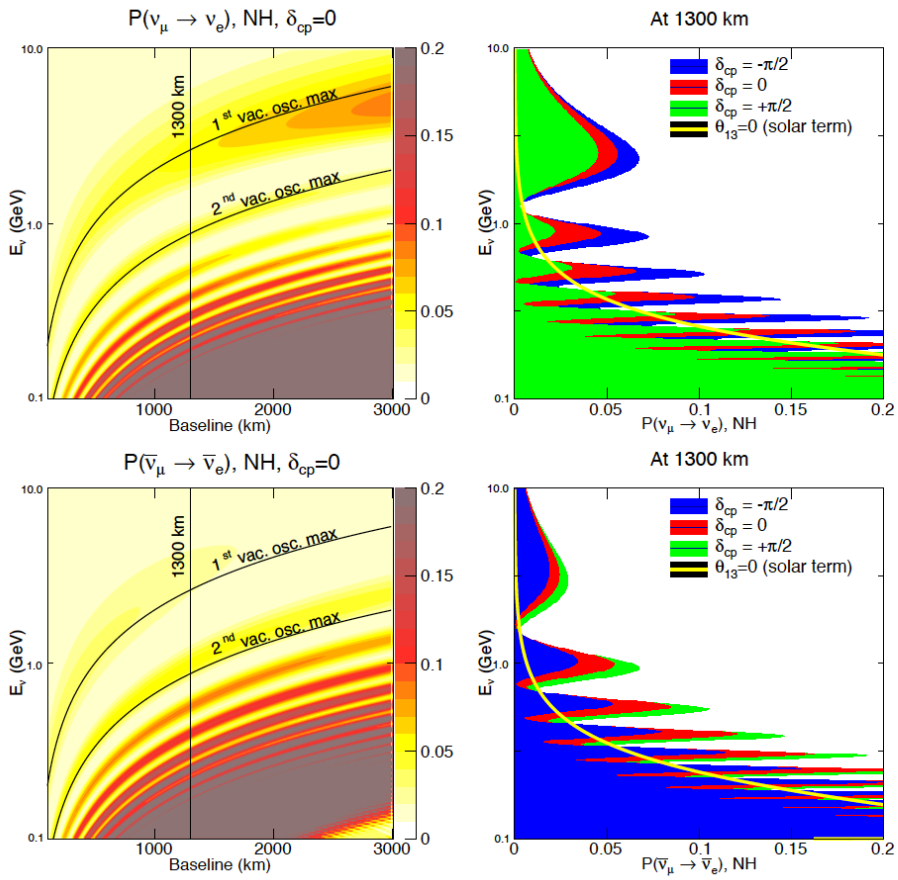

Figure 1.6: The top left plot shows the neutrino oscillation probability $P(\nu_\mu \to \nu_e)$ as a function of L and E_ν with $\delta_{CP} = 0$ and the mass hierarchy in normal ordering. The top right plot shows $P(\nu_\nu \to \nu_e)$ as a function of E_ν at a fixed baseline $L = 1,300$ km, for $\delta_{CP} = 0$, $-\pi/2$, and $\pi/2$. The bottom plots show the same probabilities but for antineutrinos $\bar{\nu}_\mu \to \bar{\nu}_e$ [10].

neutrino energy range for DUNE is between 1 and 8 GeV, by measuring the shape of the oscillation probabilities in that energy range and comparing it to the plots on the right of Fig. 1.6 and 1.7, it is possible to determine the value of δ_{CP}.

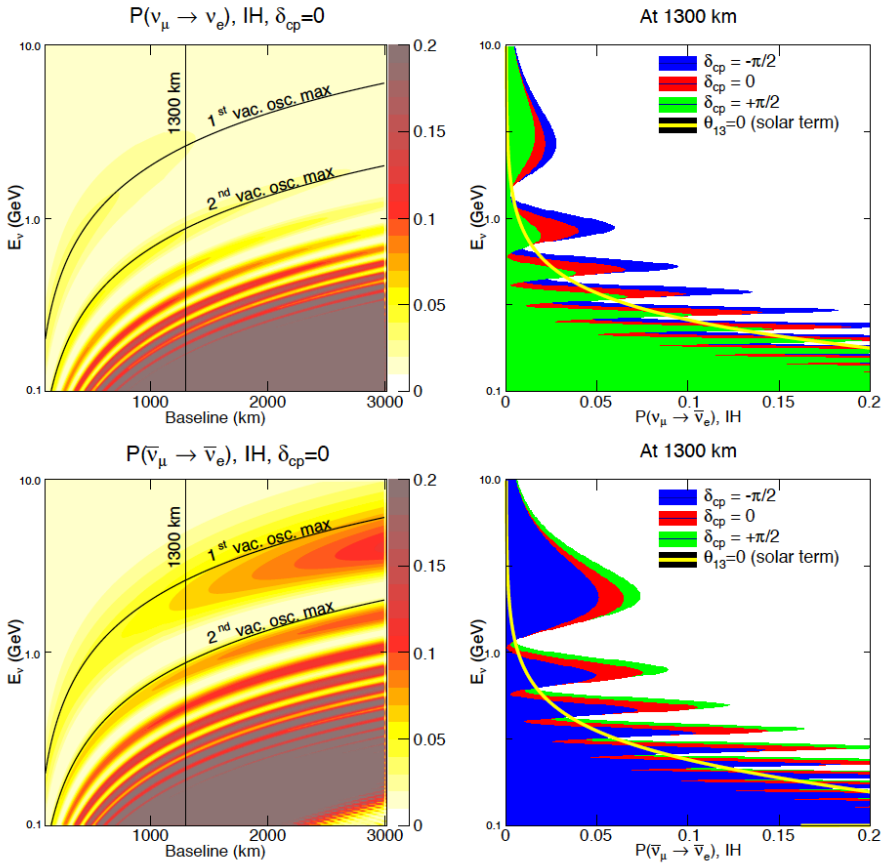

Figure 1.7: The top left plot shows the neutrino oscillation probability $P(\nu_\mu \to \nu_e)$ as a function of L and E_ν with $\delta_{CP} = 0$ and the mass hierarchy in inverted ordering, the top right plot shows $P(\nu_\mu \to \nu_e)$ as a function of E_ν at a fixed baseline $L = 1,300$ km, for $\delta_{CP} = 0$, $-\pi/2$, and $\pi/2$. The bottom plots show the same probabilities but for antineutrinos $\bar{\nu}_\mu \to \bar{\nu}_e$ [10].

1.3 Electron scattering

Electron scattering has been one of the most powerful methods of studying the nuclear structure of a nucleus. The high energy electron beam can be thought of a clean probe of the target nucleus. The electron scattering process can be described by the exchange of virtual photons. The virtual photon with energy ω and 3-momentum q can interact with charge density and electromagnetic currents of the target nucleus, by measuring the cross

section of electron scattering at different kinematics, one can get more detailed information on the nuclear structure.

The main goal of the E12-14-012 experiment is to measure the exclusive Ar(e,e′p) and Ti(e,e′p) cross sections and furthermore extract the proton and neutron spectral functions of argon. However, we took data on both inclusive (e,e′) and exclusive (e,e′p) processes, these two processes will be described in detail in this section. The inclusive cross section is also of great importance because it is the integral of the spectral function, so it contains contributions from all possible reactions, it gives less specific information than the exclusive scattering but it samples the spectral function over a broader range of momentum and energy.

1.3.1 Inclusive cross section (e,e′)

In an inclusive electron scattering experiment, after the electron beam hit the target, a spectrometer is set at a fixed angle to detect the scattered electron of a specific momentum. This measurement doesn't select a particular reaction channel, instead, it includes all of the processes that can produce an electron being detected by the spectrometer, so this is called an "inclusive" measurement.

Figure 1.8 shows the (e,e′) cross section as a function of the energy transfer ω for a fixed value of $Q^2 = q^2 - \omega^2$ [12]. The first peak is called elastic peak, at this peak, the energy transfer $\omega = \frac{Q^2}{2m_A}$ (where m_A is the nuclear mass) is low, and the virtual photon interacts with the entire nucleus. When the ω gets a bit higher, the target nucleus is excited to higher energy bound states, that is why we can see a few sharp peaks after the elastic peak. The broad bump after the sharp peaks corresponds to the collective mode of excitation of the nucleus, which is called the "Giant Resonances". The quasielastic peak is a broad bump and centered

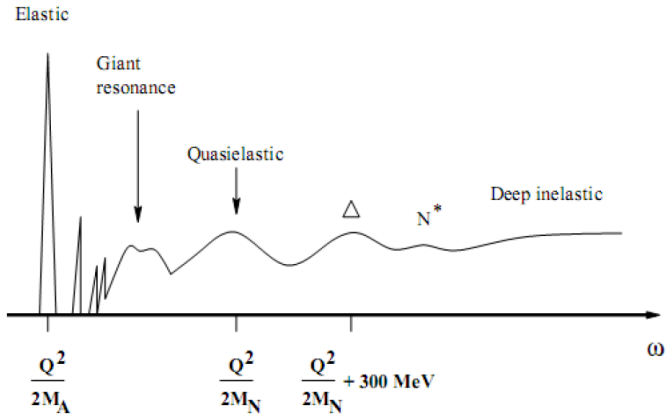

Figure 1.8: General (e,e′) energy spectrum

.

near $\omega = \frac{Q^2}{2m}$ (m is the mass of the nucleon), which corresponds to the virtual photon being absorbed by a single nucleon. Then comes the Δ and N^* resonances, in this region, the quarks inside the nucleon absorb the virtual photons, and the nucleon gets excited. If the energy transfer ω gets even higher, we get to the region called "Deep Inelastic Scattering", where the electron scattering off the constituent quarks leads to the breakup of the nucleon.

For an inclusive process

$$e(k_e) + A(p) \rightarrow e'(k_{e'}) + X(p') \ , \tag{1.29}$$

where an electron scatters off a nuclear target A, and only the scattered electron gets detected, the four-momenta are defined as

$$k_e = (E_e, \mathbf{k}_e), k_{e'} = (E_{e'}, \mathbf{k}_{e'}), p = (E_p, \mathbf{p}), p' = (E_{p'}, \mathbf{p}'). \tag{1.30}$$

With the one-photon exchange approximation, the differential cross section can be written as

$$\frac{d^2\sigma}{d\Omega_{e'} dE_{e'}} = \frac{\alpha^2}{Q^4} \frac{E_{e'}}{E_e} \ L_{\lambda\mu} W^{\lambda\mu} \ , \tag{1.31}$$

where $d\Omega_{e'}$ is the differential solid angle into where the electron scatters, $Q^2 = -q^2$ and $q = k_e - k_{e'} \equiv (\omega, \mathbf{q})$ is the four momentum transfer.

The tensor $L_{\lambda\mu}$ can be written in the form

$$L_{\lambda\mu} = 2[k_e^\lambda k_e^\mu + k_{e'}^\mu k_{e'}^\lambda - g^{\lambda\mu}(k_e k_{e'})], \tag{1.32}$$

where the electron mass is neglected and $g^{\lambda\mu} = diag(1, -1, -1, -1)$.

The tensor $W^{\lambda\mu}$ is defined by

$$W^{\lambda\mu} = \sum_X \langle 0|J^\lambda|X\rangle\langle X|J^\mu|0\rangle\delta^{(4)}(p + q - p'). \tag{1.33}$$

In the most general case, $W^{\lambda\mu}$ can be written as a function of two structure functions:

$$W^{\lambda\mu} = W_1\left(-g^{\lambda\mu} + \frac{q^\lambda q^\mu}{q^2}\right) + \frac{W_2}{m_A^2}\left(p^\lambda - \frac{(pq)}{q^2}q^\lambda\right)\left(p^\mu - \frac{(pq)}{q^2}q^\mu\right), \tag{1.34}$$

where m_A is the target mass.

With Eq. (1.32) and Eq. (1.32), Eq. (1.31) becomes

$$\frac{d^2\sigma}{d\Omega_{e'}dE_{e'}} = \left(\frac{d\sigma}{d\Omega_{e'}}\right)_{\mathrm{M}}\left[W_2(|\mathbf{q}|, \omega) + \mathbf{2W_1}(|\mathbf{q}|, \omega)\tan^{\mathbf{2}}\frac{\theta_{\mathbf{e}}}{\mathbf{2}}\right], \tag{1.35}$$

where $\left(\frac{d\sigma}{d\Omega_{e'}}\right)_{\mathrm{M}}$ is the Mott cross section

$$\left(\frac{d\sigma}{d\Omega_{e'}}\right)_{\mathrm{M}} = \frac{\alpha^2\cos^2(\frac{\theta_e}{2})}{4E_e^2\sin^4(\frac{\theta_e}{2})}. \tag{1.36}$$

The virtual photon exchanged in electron scattering has both longitudinal and transverse

polarizations. Thus we can also rewrite the cross section in terms of the longitudinal and transverse structure functions, R_L and R_T:

$$\frac{d^2\sigma}{d\Omega_{e'}dE_{e'}} = \left(\frac{d\sigma}{d\Omega_{e'}}\right)_{\mathrm{M}} \left[\left(\frac{Q^2}{|\mathbf{q}|^2}\right)^2 R_L(|\mathbf{q}|,\omega) + \left(\frac{1}{2}\frac{Q^2}{|\mathbf{q}|^2} + \tan^2\frac{\theta}{2}\right) R_T(|\mathbf{q}|,\omega)\right] . \tag{1.37}$$

1.3.2 Exclusive cross section (e,e′p)

In an exclusive (e,e′p) electron scattering experiment, we detect both the scattered electron and the knocked out proton using two different spectrometers, simultaneously.

Figure 1.9 shows a diagram of the (e,e′p) reaction, where $k_i = (E_i, \mathbf{k}_i)$ and $k_f = (E_f, \mathbf{k}_f)$ are the initial and final 4 momenta of the beam electron, $p_p = (E_p, \mathbf{p}_p)$ is the 4 momentum of the scattered proton, $\mathbf{k}_i$, $\mathbf{k}_f$ and $\mathbf{p}_p$ can be measured from experiments. Since electrons are light and their mass can be neglected, $E_i \approx |\mathbf{k}_i|$ and $E_f \approx |\mathbf{k}_f|$. E_p can be calculated from $E_p = \sqrt{M_p^2 + \mathbf{p}_p^2}$, where M_p is the rest mass of proton. The 4-momentum transfer is given by $q = k_i - k_f = (\omega, \mathbf{q})$.

The invariant cross section is given by [12]

$$d\sigma = \frac{1}{(2\pi)^3}\frac{E_f}{E_i}\frac{\alpha^2}{Q^4}\eta_{\mu\nu}W_{\mu\nu}dE_f d\Omega_e d^3\mathbf{p}_p, \tag{1.38}$$

where $d\Omega_e$ is the solid angle that covers the momentum of the electron in the laboratory, $\eta_{\mu\nu}$ and $W_{\mu\nu}$ are the electron and nuclear response tensors, respectively. With

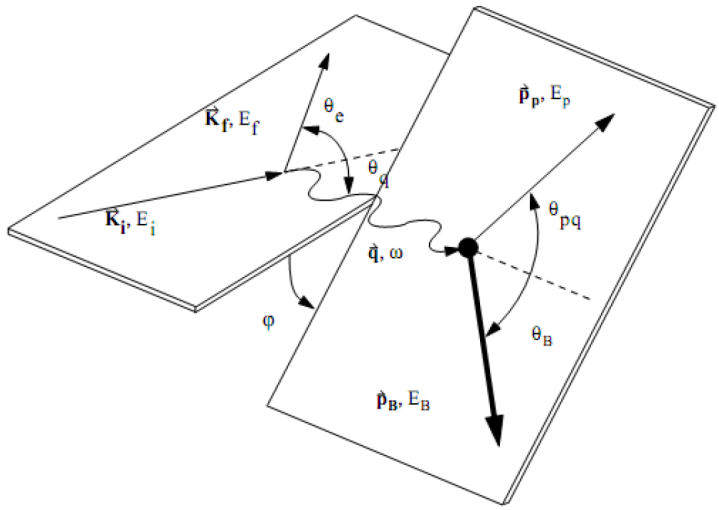

Figure 1.9: A diagram of the (e,e′p) reaction

.

$$d^3\mathbf{p}_p = E_p p_p dE_p d\Omega_p \tag{1.39}$$

where $d\Omega_p$ describes the solid angle covers the proton momentum in the laboratory, and we can write the six fold differential cross section as below:

$$\frac{d^6\sigma}{dE_f d\Omega_e dE_p d\Omega_p} = \frac{E_p p_p}{(2\pi)^3}\frac{E_f}{E_i}\frac{\alpha^2}{Q^4}\eta_{\mu\nu}W_{\mu\nu}. \tag{1.40}$$

For an ultra-relativistic electron, the speed of which is close to that of light, we can treat it as a massless particle and write the electron response tensor $\eta_{\mu\nu}$ as

$$\eta_{\mu\nu} = 2(k_{i\mu}k_{f\nu} + k_{f\mu}k_{i\nu} - k_i k_f g_{\mu\nu}) \tag{1.41}$$

or the alternative form

$$\eta_{\mu\nu} = K_\mu K_\nu - q_\mu q_\nu - Q^2 g_{\mu\nu} \tag{1.42}$$

where $K_\mu = k_{i\mu} + k_{f\mu}$, and $q_\mu = k_{i\mu} - k_{f\mu}$.

The nuclear response tensor is the bilinear products of the nuclear current operator matrix elements:

$$W_{\mu\nu} = \langle J_\mu J_\nu^\dagger \rangle. \tag{1.43}$$

where $\langle .. \rangle$ denotes averaging over initial states and summed over final states.

By applying the nuclear current conservation constraint, as well as continuity requirement, which is written as:

$$\begin{aligned} q_\mu W^{\mu\nu} = W^{\mu\nu} q_\nu = 0 \\ J_z = \frac{\omega}{\vec{q}} \rho \end{aligned} \tag{1.44}$$

After some tedious math derivation, we obtain the form of the contraction between the electron and nuclear tensors:

$$\eta_{\mu\nu} W_{\mu\nu} = 4 E_i E_f \cos^2 \frac{\theta_e}{2} [V_L R_L + V_T R_T + V_{LT} R_{LT} cos\phi + V_{TT} R_{TT} \cos 2\phi]. \tag{1.45}$$

The kinematic factors are expressed as

$$
\begin{aligned}
V_L &= \frac{Q^4}{\vec{q}^4} \\
V_T &= \frac{Q^2}{2\vec{q}^2} + \tan^2(\frac{\theta_e}{2}) \\
V_{LT} &= \frac{Q^2}{\vec{q}^2} + \left[\frac{Q^2}{\vec{q}^2} + \tan^2(\frac{\theta_e}{2})\right]^{\frac{1}{2}} \\
V_{TT} &= \frac{Q^2}{2\vec{q}^2},
\end{aligned}
\tag{1.46}
$$

the response functions can be written in terms of nuclear current tensor

$$
\begin{aligned}
R_L &= \langle W_{00} \rangle = \langle \rho\rho^\dagger \rangle \\
R_T &= \langle W_{xx} + W_{yy} \rangle = \langle J_\parallel J_\parallel^\dagger + J_\perp J_\perp^\dagger \rangle \\
R_{LT}\cos\phi &= -\langle W_{0x} + W_{x0} \rangle = -\langle \rho J_\parallel^\dagger + J_\parallel \rho^\dagger \rangle \\
R_{TT}\cos 2\phi &= \langle W_{xx} - W_{yy} \rangle = \langle J_\parallel J_\parallel^\dagger - J_\perp J_\perp^\dagger \rangle,
\end{aligned}
\tag{1.47}
$$

where ρ is the charge component of the nuclear current.

$J_\parallel$ and $J_\perp$ are the transverse components of the nuclear current, and R_L, R_T, R_{TL}, and R_{TT} are the response functions of kinematic variables which can obtained from the (e,e′p) reaction. $J_\parallel$ and $J_\perp$ are respectively inside the scattering plane and orthogonal to the scattering plane, while both are also orthogonal to $\mathbf{q}$.

R_L arises from the charge and longitudinal component of the nuclear current, R_T is the incoherent sum of the contributions from the two transverse components of the nuclear current. R_{TL} is the interference of the transverse component with the longitudinal component of the nuclear current in the scattering plane, while R_{TT} is the interference between the two transverse components of the nuclear current.

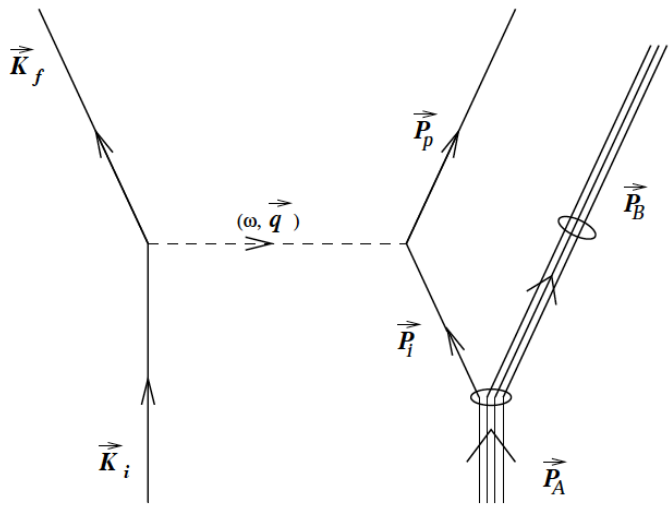

Figure 1.10: A diagram of the PWIA in (e,e′p) reaction [13].

In the special case of parallel kinematics, ($\mathbf{p}_p \parallel \mathbf{q}$), the orientation of the reaction plane (the azimuthal angle ϕ) becomes undefined, and only R_T and R_L contribute to the cross section expression.

1.3.3 PWIA - Plane Wave Impulse Approximation

In the Plane Wave Impulse Approximation(PWIA) [37], the virtual photon is totally absorbed by the proton, and the outcome proton doesn't interact with the residual nucleus. Fig. 1.10 shows the diagram of this process.

We are interested in two quantities, namely the missing momentum $\mathbf{p}_{miss}$, and the missing energy E_{miss}. The missing energy is defined by

$$E_{miss} = \omega - T_p - T_B, \tag{1.48}$$

where T_p and T_B are respectively the kinetic energies of the scattered proton and the recoil

nucleus. By definition T_p and T_B can be written as

$$T_p = \sqrt{\mathbf{p_p}^2 + m_p^2} - m_p \tag{1.49}$$

$$T_B = \sqrt{\mathbf{p_B}^2 + M_B^2} - M_B. \tag{1.50}$$

With the momentum conservation law, the missing momentum is given by

$$\mathbf{p}_{miss} = \mathbf{p}_p - \mathbf{q} = -\mathbf{p}_B. \tag{1.51}$$

The energy conservation law also applies here,

$$E_i + M_A = E_f + E_P + E_B \tag{1.52}$$

$$\omega = E_p + E_B - M_A = (m_p + T_p) + (M_B + T_B) - M_A \tag{1.53}$$

By plugging Eq. (1.53) into Eq. (1.48), one can get

$$E_{miss} = m_p - M_A + M_B, \tag{1.54}$$

From Eq. (1.51) we can see that the missing momentum is the initial momentum of the proton inside the nucleus, and Eq. (1.54) implies that the missing energy describes the difference between the initial and final state in terms of nuclear binding energy.

Going forward, we can rewrite the M_B as

$$\begin{aligned} M_B &= \sqrt{E_B^2 - \mathbf{p}_B^2} \\ &= \sqrt{E_B^2 - \mathbf{p}_{miss}^2} \\ &= \sqrt{(\omega + M_A - E_p)^2 - \mathbf{p}_{miss}^2} \end{aligned} \tag{1.55}$$

Then the missing energy is defined as:

$$E_{miss} = m_p - M_A + \sqrt{(\omega + M_A - E_p)^2 - \mathbf{p}_{miss}^2}. \tag{1.56}$$

In non-relativistic PWIA, we can factorize the cross section [37]:

$$\frac{d\sigma}{dE_f d\Omega_e dE_p d\Omega_p} = \frac{E_p p_p}{(2\pi)^3} \sigma_{ep} S(E_{miss}, \mathbf{p}_{miss}), \tag{1.57}$$

where σ_{ep} is the off-shell cross section [86] and S is the spectral function, which is the probability of finding a proton having momentum $\mathbf{p}_{miss}$ and binding energy E_{miss} in the nucleus.

1.3.4 DWIA - Distorted Wave Impulse Approximation

In PWIA, the Final State Interaction (FSI) between the outgoing nucleon and the residual nucleus, while known as non-negligible, is actually not taken into account. To include FSI, we use the Distorted Wave Impulse Approximation (DWIA).

Figure 1.11 shows the diagram of the DWIA.

We can write the (e,e′p) cross section by replacing the spectral function by a distorted one, denoted as S^D,

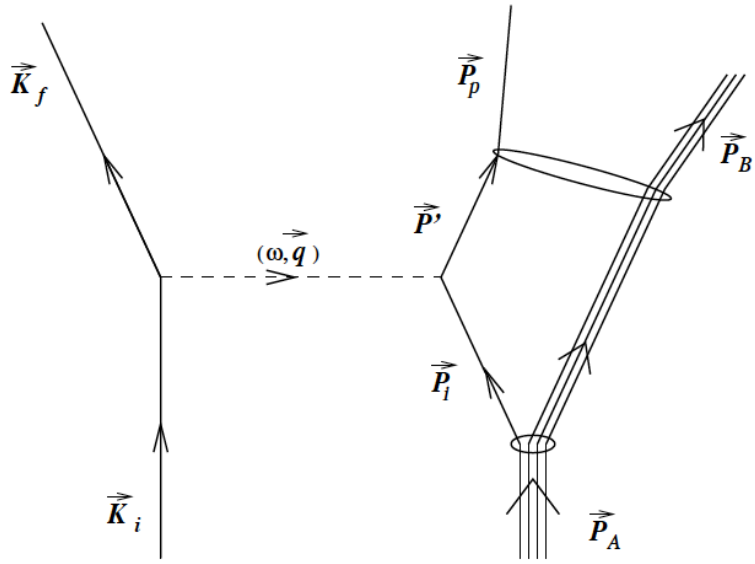

Figure 1.11: A diagram of the DWIA in (e,e′p) reaction [13].

$$\frac{d\sigma}{dE_f d\Omega_e dE_p d\Omega_p} = \frac{E_p p_p}{(2\pi)^3} \sigma_{ep} S^D(E_{miss}, \mathbf{p}_{miss}, \mathbf{p}_p). \tag{1.58}$$

Besides the E_{miss} and $\mathbf{p}_{miss}$, S^D also depends on the proton momentum $\mathbf{p}_p$, since the FSI are different for the knocked out nucleons depending on their momenta.

The typical effects of FSI depends slightly on the kinematic, in general they will result in (1) a slight shift of the PWIA momentum distribution towards smaller values (∼2-5 MeV), (2) a reduction of the PWIA double differential cross section between 30% and 80% depending on the shells and the target nuclei in a fairly systematic way and (3) broadening the missing energy spectrum [14].

Chapter 2

Experimental Setup

The E12-14-012 [18] experiment performed a high precision measurement of the inclusive (e,e′) and exclusive (e,e′p) double differential cross sections for multiple nuclear targets. The data taking took place in Hall A of the Thomas Jefferson National Accelerator Facility (Jefferson Lab) between February and March of 2017. In this chapter, we will give an overview of the apparatus in Hall A, together with the details of the data taking.

2.1 Jefferson Lab Hall A - Overview

Figure 2.1 shows the basic configuration of Jefferson Lab Hall A. The electron beam is delivered from the Continuous Electron Beam Accelerator Facility (CEBAF) to the hall. The beam intensity is measured using two beam current monitors (BCMs), where the beam current is determined. After that the beam passes through a quadrupole magnet that increase the beam size to a 2×2 mm square before hitting a cryogenic target system.There are also two beam position monitors (BPMs) installed along the beamline to give accurate information on the position and direction of the beam. After the beam hits the target, the outcome particles are detected by two high resolution spectrometers (HRSs). The two HRSs are almost identical to each other, and they can be rotated around the central point that coincides with the center of the cryogenic target.

In the E12-14-012 experiment, the left and right arm spectrometers were used to detect,

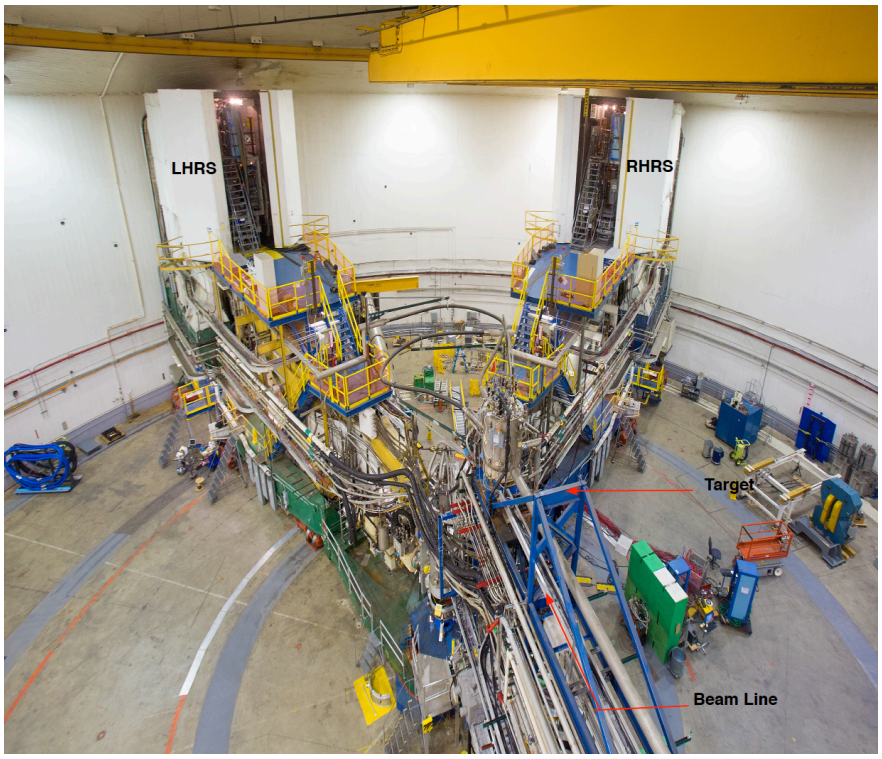

Figure 2.1: A picture of Hall A [15].

respectively, electrons and protons.

2.2 Hall A Beamline

2.2.1 Beam Energy Measurements

The absolute beam energy is measured with two different methods, the ARC method and the eP method. These two measurements agree well with each other and they both have an accuracy ($\Delta E/E$) of 2×10^{-4}.

In the ARC method [17], the beamline is bent by the magnetic field as it passes through the ARC section. As shown in Fig. 2.2, the ARC section consists of eight dipoles that are carefully arranged so that the beam can pass through all of them. The nominal bending

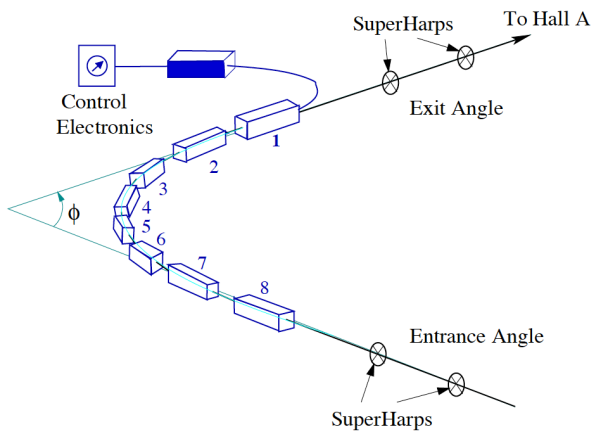

Figure 2.2: The CEBAF ARC section [24].

angle is $\theta = \pi - \phi = 37.5°$. The electron beam momentum is determined by measuring the actual bending angle θ and the integral of the magnetic field of the eight dipoles:

$$p = k\frac{\int \vec{B} \cdot \vec{dl}}{\theta}, \tag{2.1}$$

where p is in GeV/c, $\int \vec{B} \cdot \vec{dl}$ is in $\mathrm{T} \cdot \mathrm{m}$, θ is in rads, and $k = 0.299792\mathrm{GeV} \cdot \mathrm{rad} \cdot \mathrm{T}^{-1} \cdot \mathrm{m}^{-1}/c$. The bending angle is measured by a set of wire scanners and the field integral is determined using a 9th identical dipole as the reference magnet.

The eP method determines the beam energy based on the $^1H(e, e'p)$ elastic-scattering reaction [17]. In this method, there is a eP device located 17 m upstream of the target. Fig. 2.3 shows the schematic diagram of the eP system. The incident electron is scattered by a CH_2 target, after which the scattered electron and recoil proton are detected by two identical detector arms, each of which consists of an electron and a proton detector package. The two arms are placed symmetrically with respect to the beamline. The proton detector is at a fixed angle while the electron detector can be set to a range of angles corresponding to a beam energy range of 0.5 to 6.0 GeV. By measuring the scattered electron angle θ_e and the

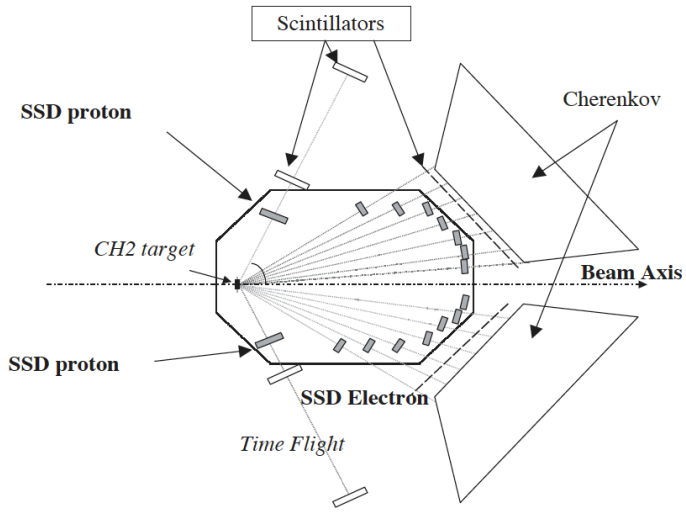

Figure 2.3: Schematic layout of the eP energy measurement system [17].

recoil proton angle θ_p, we can determine the beam energy by:

$$E = M_p \frac{\cos(\theta_e) + \sin(\theta_e)/\tan(\theta_p) - 1}{1 - \cos(\theta_p)} + O(m_e^2/E^2), \tag{2.2}$$

where M_p is the mass of the proton and m_e is that of the electron.

2.2.2 Beam Current Monitors

Along the beamline, the beam current monitor (BCM) is installed 25 m upstream of the target location. It provides a stable, low-noise and non-interfering measurements of the beam current [17]. The BCM consists of a parametric current transformer (Unser monitor), two RF cavities, associated electronics, and a data-acquisition system represented in Fig. 2.4)

The two RF cavities are stainless steel cylindrical high frequency waveguides, when the frequency is tuned to match the that of the beamline, they can provide output signal that is proportional to the beam current.

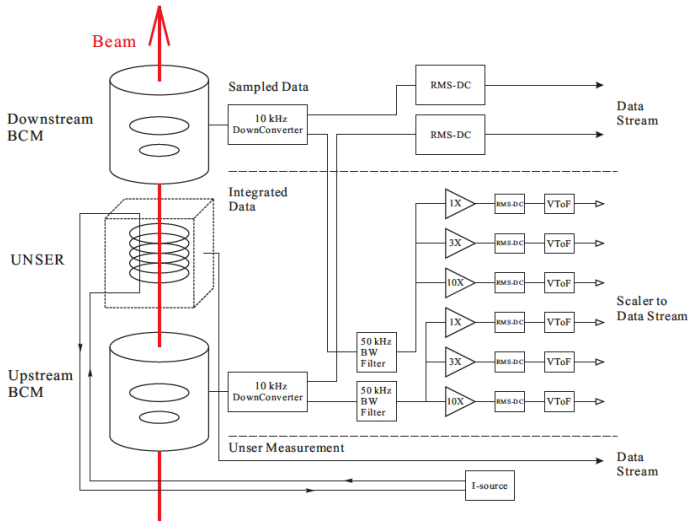

Figure 2.4: Schematic diagram of the Hall A beam current monitor system.

The Unser monitor is used to provide an absolute reference for the calibration of the RF cavities [28]. To calibrate the Unser monitor, we pass a known current through a wire inside the beam pipe, so that the gain and offset can be determined. The gain of the Unser is stable while the offset drifts significantly on a time scale of several minutes, thus we will not use the Unser monitor to continuously monitor the beam current when taking data. However, the two RF cavities are very stable, after being calibrated using the Unser monitor, they can be used to determine the beam current and integrated charge.

The output signal of the RF cavities is split into two copies, one is sent to an AC voltmeter to provide an average beam current measurement every one second, the other copy is converted into an analog DC voltage level by passing through an RMS-to-DC converter.

There is a linear relationship between the output signal of the RF cavities and the converted analog DC voltage level, and that relationship holds when the beam current is from 10 μA and 200 μA, so to include low current in this range, each RF cavity output signal is split into three copies before being sent to the RMS-to-DC converter, two of them are amplified

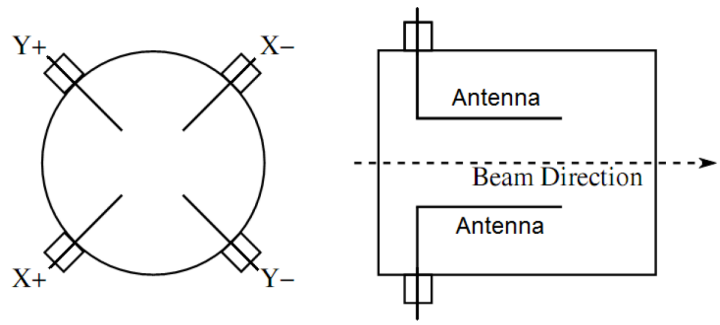

Figure 2.5: Diagram of a BPM. Left view is along the beam axis [24].

by 3 times and 10 times. Thus the BCM can produce six signals in total which are further counted by scalers in both HRSs.

2.2.3 Beam Position Monitors

The beam position monitors (BPMs) are used to provide the information of the position and direction of the beam at the target. The two BPMs, BPMA and BPMB, are located at 7.524 m and 1.286 m upstream of the target [17, 19, 20]. Each BPM contains a cavity with a 4-wires antenna oriented parallel to the electron beam pipe, the 4 wires are rotated $\pm 45°$ from the horizontal and vertical directions (see Fig. 2.5). When the electron beam passes through the cavity, there are induced signals in the wires and the amplitude of the signals are related to the distance between the electron beam and the wires. By comparing the signals in two opposite wires, the x and y position of the beam can be obtained. Knowing the beam positions at two BPMs, one can easily calculate the direction of the beam. In order to obtain the absolute position of the beam, The BPMs need to be calibrated using two pre-surveyed wire scanners called ”super-harps” placed near the BPMs.

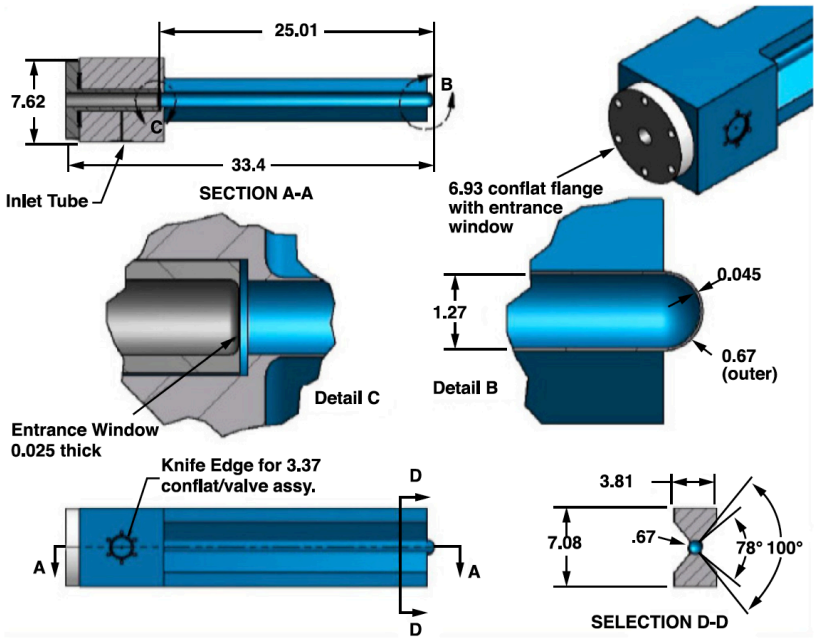

Figure 2.6: Design of the gas cell, units are in cm [27].

2.3 Target System

In the E12-14-012 experiment, five different targets were used, they were respectively argon, carbon, titanium, aluminum, and carbon optical targets.

The argon target is a closed gas cell, it is the same design as the target cell used in the MARATHON experiment E12-10-103 [26]. It is a cylindrical cell made of aluminum. Fig. 2.6 shows the configuration of the cell. The length and the diameter if the cell are 25 cm and 12.7 mm, respectively. The density of the argon gas without beam on target is 58.2 kg/m^3. Fig. 2.7 is a photo of the argon target installed on the standard Hall A cryogenic target system. The target density will decrease when there is a beam passing through it because the beam can deposit heat to the gas and cause it to expand locally. We will call that the "boiling effect". A detailed description of the method we used in determining the relation between the beam current and the target density can be found in Ref. [27]. At a beam

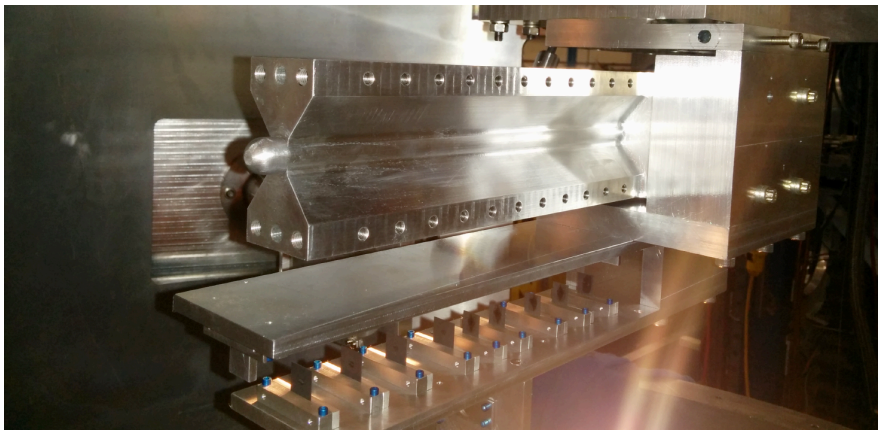

Figure 2.7: A photo of the argon target installed on the standard Hall A cryogenic target ladder, at the bottom is the optical target, the Dummy target is right above the optical target.

current of 20 μA, the "boiling effect" is 27.5±0.3% for the argon target, which means the target density decreases by 27.5% when the beam was on the target.

The dummy target contained two separate aluminum blocks. They were placed at the same positions corresponding to the argon target entrance and exit windows. The thickness of the two blocks was 0.889 cm, which corresponded to the total thickness of the argon target in radiation length. We use the dummy target to estimate the background events induced by electron interactions in the entrance and exit window of the argon target cell.

The optical target is a series of nine carbon foils, which is used for measuring and calibrating the spectrometer optics. The thickness of each carbon foil was 0.3495 g/cm^2. The dummy target and optical target can also been seen in Fig. 2.7.

The titanium target is simple foil target, with a thickness of 0.729 g/cm^2. The reason why we have titanium target is that in neutrino oscillation experiments, neutrinos interact with both protons and neutrons, the spectral function of protons can be extracted from the (e,e′p) experiment, while it's hard to measure (e,e′n) process. Since the shell structure of the protons in titanium is nearly the same as that of neutrons in argon (see Fig. 2.8), the

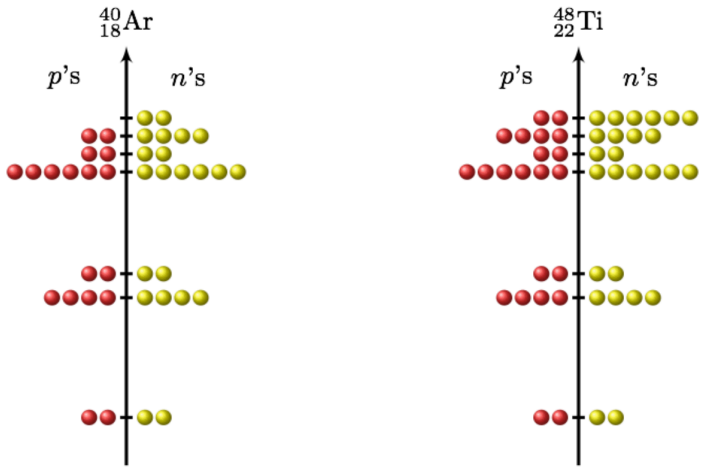

Figure 2.8: Shell model structures of argon and titanium.

spectral function of protons in titanium could be used to estimate the spectral function of neutrons in argon.

The carbon target is a foil target, with a thickness of 0.167 g/cm^2. The measured carbon cross section is used to compare with previous results and to verify the validity of our analysis methods.

All the targets are mounted on the Hall A target ladder (Fig. 2.9). To select a specific target, one can move the ladder using a remote automatic system vertically up and down until the beam and the target center are aligned.

2.4 High Resolution Spectrometers (HRSs)

In the E12-14-012 experiment, the scattered electrons and the knocked out protons are detected using the left and right arm high resolution spectrometers in Hall A. The two spectrometers are nearly identical, and have a good resolution in the measurement of particle momentum, position and angles. The momentum ($\mathrm{d}p/p$) resolution can reach 2×10^{-4} and

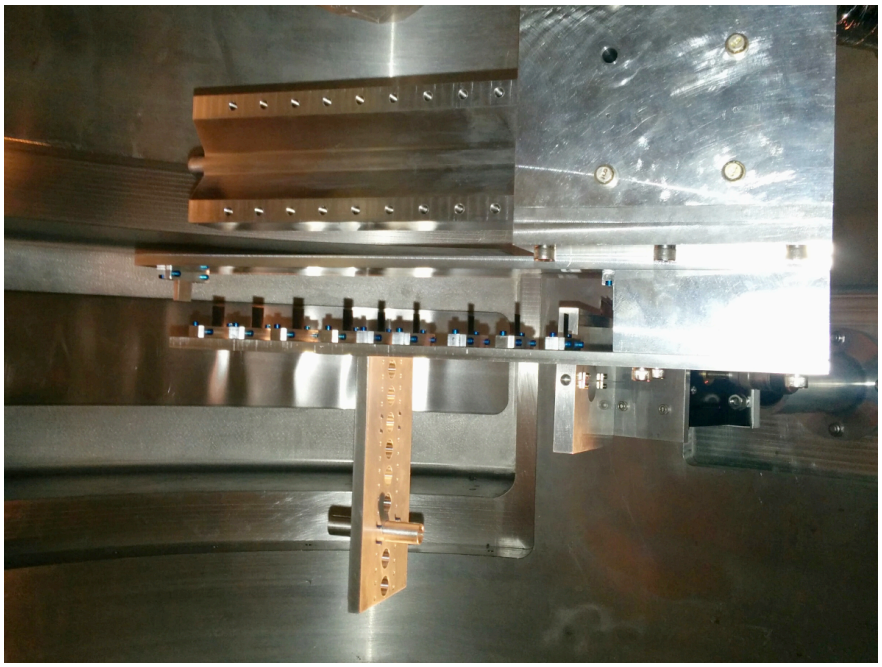

Figure 2.9: Picture of the Hall A target ladder system.

the horizontal angular resolution is better than 2 mrad at a designed maximum central momentum of 4 GeV/c. The main characteristics of the spectrometers are listed in Tab. 2.1 [17].

Table 2.1: Main characteristics of the Hall A HRSs [17].

Configuration	QQD$_n$Q Vertical bend
Bending angle	45°
Optical length	23.4 m
Momentum range	0.3 - 4.0 GeV/c
Momentum acceptance	-4.5% < δp/p <+4.5%
Momentum resolution	2×10^{-4}
Angular acceptance (Horizontal)	±30 mrad
Angular acceptance (Vertical)	±60 mrad
Angular resolution (Horizontal)	0.5 mrad
Angular resolution (Vertical)	1.0 mrad
Solid angle at δp/p = 0, y$_0$ = 0	6 msr
Transverse length acceptance	±5 cm
Transverse position resolution	1 mm

Each HRS consists of a QQDQ magnet configuration, which contains three superconducting quadrupoles and one non-superconducting dipole. Figure 2.10 shows the layout of this

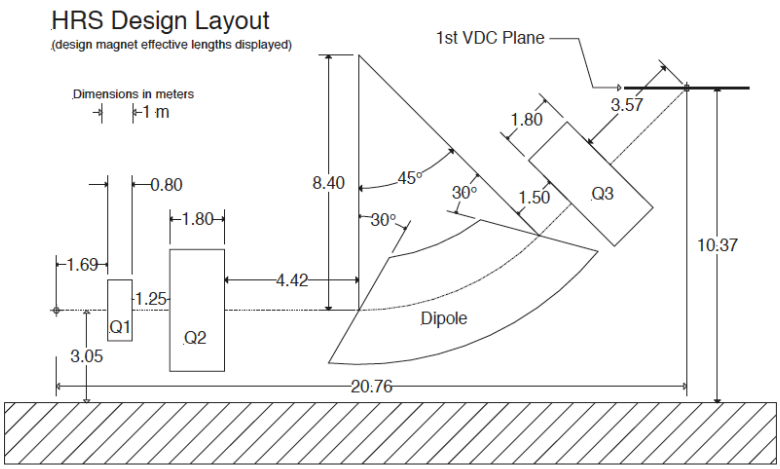

Figure 2.10: Schematic layout of the spectrometer magnet configuration (QQDQ) [17].

configuration. The quadrupoles are used to focus the particles to the focal plane, the dipole can (1) bend the charged particles up for 45°, (2) select charged particles of a specific momentum and (3) provide a focusing effect at its entrance and exit.

2.5 Detector Package

Figure 2.11 shows the side view of the detector packages for the two high resolution spectrometers (HRSs). Both arms uses the vertical drift chambers for the tracking information and a pair of scintillators (S0 and S2m) to form the triggers to activate the data-acquisition electronics. The electron arm detector package also uses a gas Cerenkov detector and a lead glass calorimeter for particle identification.

2.5.1 Vertical Drift Chambers

Each spectrometer contains a pair of vertical drift chambers(VDCs) [22], which can provide the tracking information (position and angle). The two VDCs are identical and parallel to

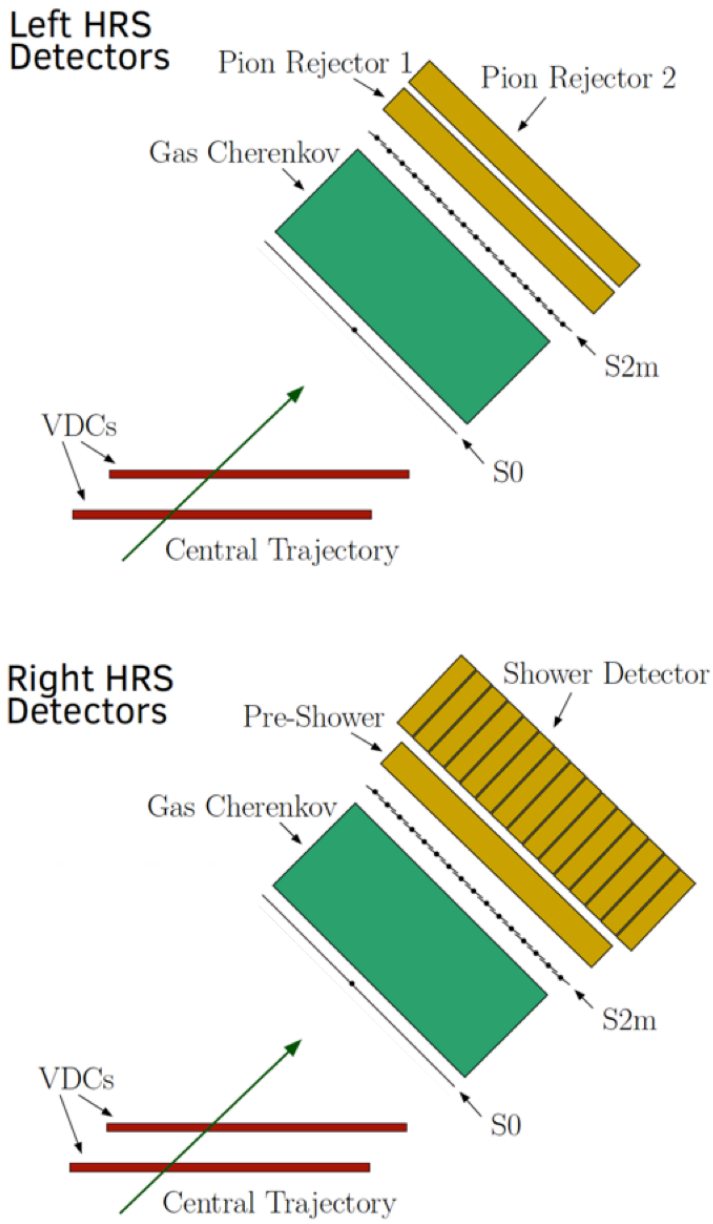

Figure 2.11: Sideview of the detector stacks, on the top(bottom) is the left(right) arm.

each other. The lower VDC is placed near the spectrometer focal plane, and the upper VDC is 335 mm above the lower one (see the plot on top in Fig. 2.12).

In each VDC, there are two wire planes, and each wire plane contains 368 signal wires, spaced 4.24 mm apart. The two wire planes are in a standard UV configuration, where the

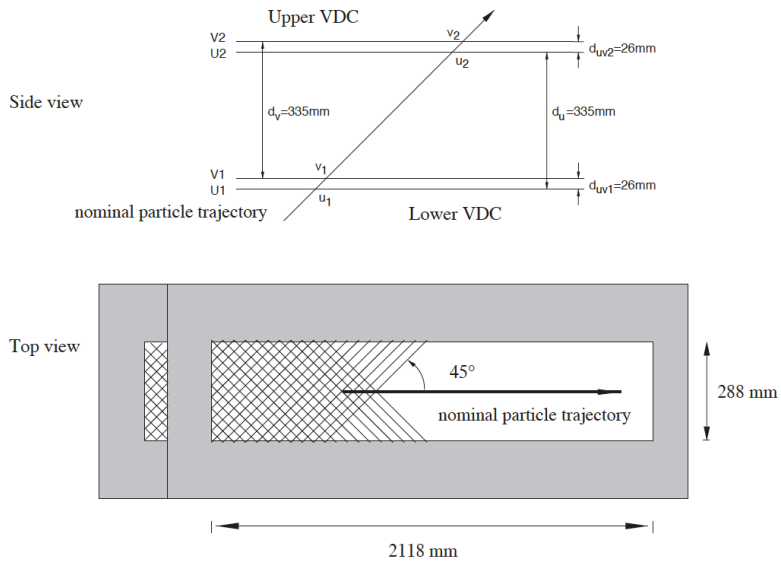

Figure 2.12: Schematic diagram of the Hall A spectrometers VDCs [17].

U and V wires are orthogonal to each other (see the plot at bottom in Fig. 2.12).

There are two gold-plated Mylar planes above and under each wire plane, by applying a high voltage of -4 kV to the Mylar planes and keeping the wire plane to the ground, we can create an electric field that can cause electrons to accelerate towards the near wires. The chambers are filled with gas mixture of argon (62%) and ethane (38%) [17].

Figure 2.13 shows a typical track through the VDC resulting in a five-cell event. When a charged particle passes through the chamber, the gas gets ionized and the electrons generated from the ionization are accelerated by the electric field and drift to the closest wires. The drift time can be measured using a time-to-drift digital converter (TDC) and it is related to the distance from the wire to the trajectory. Normally five or six distances are collected for one particle. Knowing the drift distances of all wires that have been hit, the cross-over point can be easily determined by a linear fit of drift distances versus wire positions. The particle trajectory is reconstructed by using the location information provided by all the four wire planes. The position and angular resolution of the trajectory in the focal plane can reach

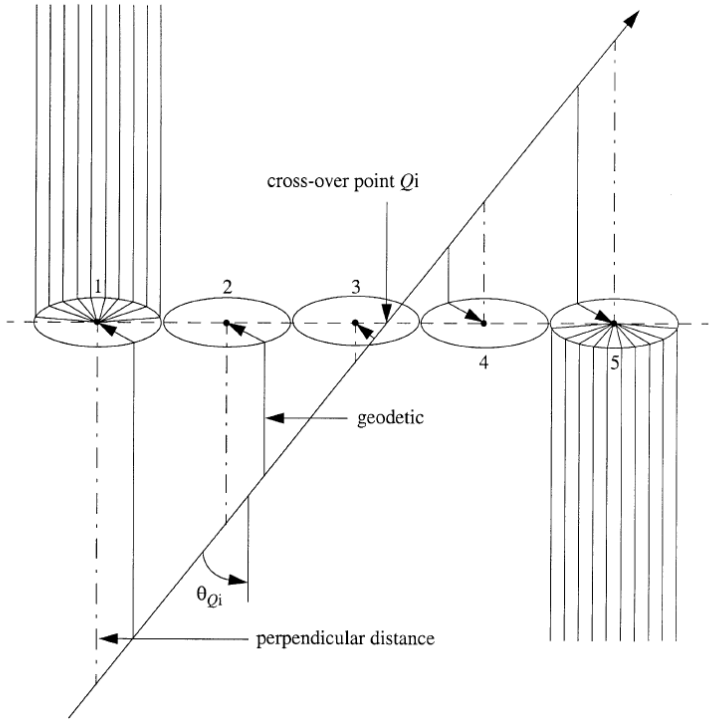

Figure 2.13: A typical VDC track example resulting in a five-cell event [22].

around 100 μm and 0.5 mrad, respectively.

2.5.2 Scintillators

Each spectrometer contains two scintillator planes S0 and S2m. They are placed parallel to each other and perpendicular to the central ray (Fig. 2.11). The distance between S0 and S2m is about 1.6 m. S0 and S2m can provide the time-of-flight information with good resolution (0.3 ns) and are used to form the triggers for events. We will discuss different triggers we have in our experiment in Sec. (2.6).

The S0 is a single scintillator paddle viewed by two photomultiplier tubes (PMTs), the active area of S0 is about 0.25 m along the non-dispersive direction and 1.7 m along the dispersive direction. The S2m consists of 16 overlapping paddles made of thin plastic scintillators

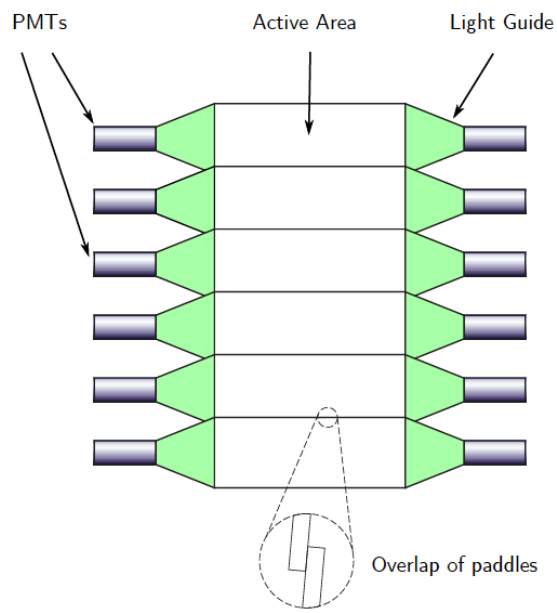

Figure 2.14: Schematic of the S2m scintillator plane, only 6 out of 16 paddles are shown here.

to minimize hadron absorption. There is a 5 mm overlap between adjacent paddles. A photomultiplier tube (PMT) is attached at both ends of each paddle (see Fig. 2.14). S2m is 43.2 cm long and 14 cm wide. When a charged particle passes into a paddle, the atoms of the scintillator material get excited, then they go back to their normal state quickly by producing a multitude of photons which can be collected by the PMTs at the paddle ends.

2.5.3 Gas Čerenkov

The Gas Čerenkov (GC) [25] counter is mounted between the S0 and S2m scintillator planes. It is filed with CO_2 at atmospheric pressure. The operation principle of the Gas Čerenkov is based on the fact that when a charged particle travels faster than the speed of light in a medium, it can emit photons (Čerenkov light) [23]. The momentum threshold for a particle to produce the Čerenkov light is

$$p_{threshold} = \frac{mc}{\sqrt{n^2 - 1}}, \tag{2.3}$$

the angle between the emitted Čerenkov light and the travel path of the charged particle is given by

$$\cos\theta = \frac{1}{\beta n}, \tag{2.4}$$

where n is the index of refraction of the medium ($n = 1.00041$ for the CO_2 in GC), and $\beta = v/c$ is the speed of the particle. The momentum threshold for producing Čerenkov light is 0.017 GeV/c for electrons and 4.8 GeV/c for pions, and given the momentum range of the HRS is from 0.3 to 4.0 GeV/c, only electrons can cause signals. Thus the Gas Čerenkov has excellent potential to distinguish between electrons and pions.

Inside the Čerenkov box, as shown in Fig. 2.15, there are ten spherical mirrors [21], which can reflect and focus the Čerenkov light to the associated ten PMTs, the signals from the PMTs can be used for forming the trigger during data taking and particle identification cuts in the analysis.

2.5.4 Lead Glass Calorimeter

The calorimeter is mounted behind the S2m scintillator plane in each HRS to provide the energy information of the particles passing through it. Each calorimeter is composed of two layers of lead glass blocks and associated PMTs. When a high energy electron passes through a dense material, i.e. lead glass, it loses energy by emitting photons through the Bremsstrahlung radiation. The emitted photon is converted to an electron and a positron through pair production. This process repeats and develops a shower of photons along the

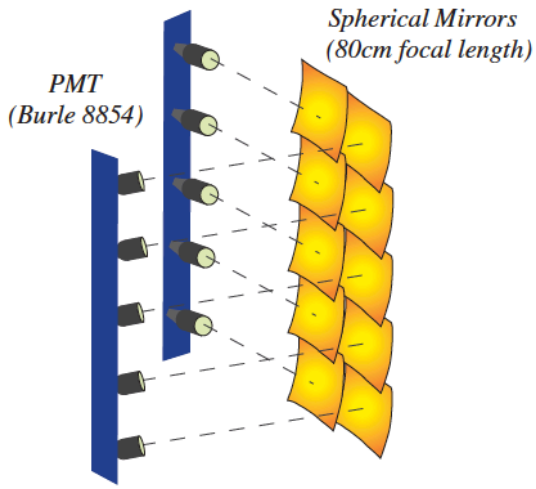

Figure 2.15: A diagram showing the spherical mirrors and PMTs inside the Gas Čerenkov [29].

traveling path in the material, the photons can be detected by the PMTs. Electrons deposit all of their energy in the calorimeter, while pions cannot develop a shower like electron due to their long nuclear interaction length. The calorimeter, together with the Gas Čerenkov, can be used to provide the information for electron/pion separation (particle identification).

The configuration of the calorimeters in the left and right arm HRS are slightly different (see Fig. 2.16). In the left HRS, both layers are composed of 34 lead glass blocks, the dimension of each block is 15 cm $\times$ 15 cm $\times$ 30 cm. The blocks in both layers are oriented perpendicular to the particle tracks. In the right HRS, the first layer is composed of 48 lead glass blocks, oriented perpendicular to the particle tracks, the dimension of each block is 10 cm $\times$ 10 cm $\times$ 35 cm. The second layer consists of 80 lead glass blocks, each block is 15 cm $\times$ 15 cm $\times$ 35 cm and oriented parallel to the particle tracks.

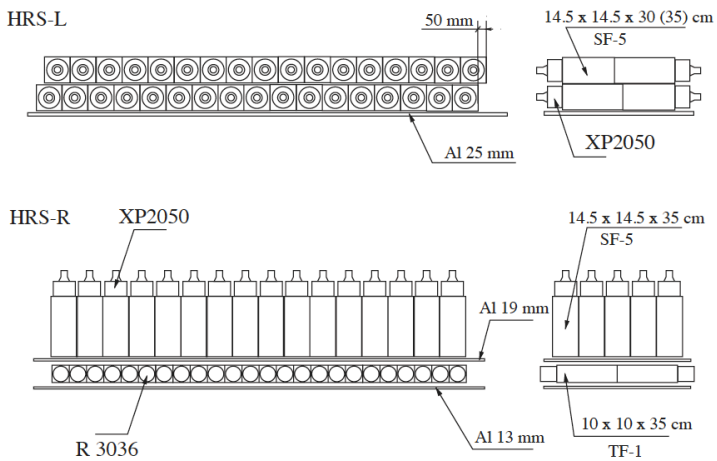

Figure 2.16: Schematic layout of the calorimeters in both the LHRS and the RHRS [17].

2.6 Trigger Design

In the E12-14-012 experiment, the scattered electrons and knocked out protons are detected by the left and right arm HRSs, respectively. The triggers are created from the signals of different detectors, including the S0 and S2m in both HRSs and Gas Čerenkov and calorimeter in the left arm HRS. We have 6 triggers in total, the design of trigger system is shown in Fig. 2.17 and Eq. (2.5) .

T3 is define as the left arm trigger, it is formed by the logical AND of S0, S2m and either a hit in the Gas Čerenkov or the calorimeter. To measure the trigger efficiency of T3, T5 is formed by a hit in either S0 or S2m and a hit in either the Gas Čerenkov or the calorimeter. T4 is the right arm trigger, it is created by the coincidence signal of the S0 and S2m. T6 is designed to evaluate the trigger efficiency of T4. T1 is the coincidence signal of T3 and T4, which is the production trigger in this experiment. T2 is the efficiency trigger for T1.

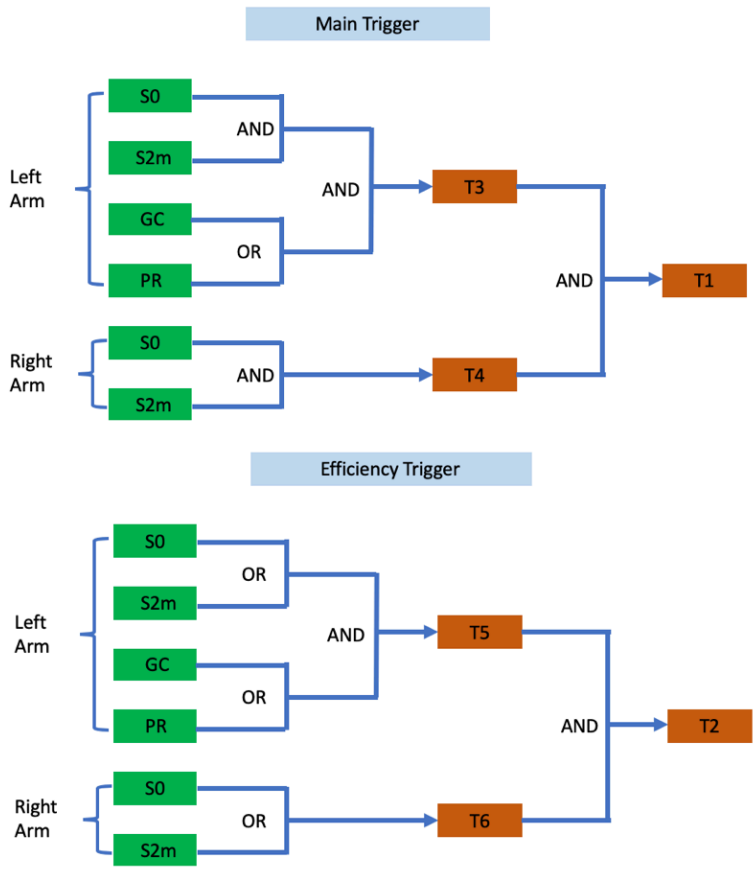

Figure 2.17: Layout of the trigger design for the E12-14-012 experiment.

$$
\begin{aligned}
\mathrm{T3} &= (L_S0 \ \&\ L_S2m) \ \&\ (L_GC \ ||\ L_PR), \\
\mathrm{T5} &= (L_S0 \ ||\ L_S2m) \ \&\ (L_GC \ ||\ L_PR), \\
\mathrm{T4} &= R_S0 \ \&\ R_S2m, \\
\mathrm{T6} &= R_S0 \ ||\ R_S2m, \\
\mathrm{T1} &= ((L_S0 \ \&\ L_S2m) \ \&\ (L_GC \ ||\ L_PR)) \ \&\ (R_S0 \ \&\ R_S2m), \\
\mathrm{T2} &= ((L_S0 \ ||\ L_S2m) \ \&\ (L_GC \ ||\ L_PR)) \ \&\ (R_S0 \ ||\ R_S2m).
\end{aligned}
\tag{2.5}
$$

2.7 E12-14-012 Data Taking Summary

In the E12-14-012 experiment, a beam of energy 2.222 GeV was used. There are 5 kinematic settings for (e,e′p) measurement in total. We took data on argon, titanium and aluminum targets at all five kinematic settings. Optics and carbon data were also taken at some of the kinematic settings. The inclusive (e,e′) double differential cross section was measured on carbon, aluminum, argon and titanium targets.

Table 2.2 shows a summary of the data taking summary and Tables 2.3 and 2.4 contains detailed information about the kinematic settings.

Table 2.2: Data taking summary

Kin1			Kin3		
Target Type	Hours	Events(k)	Target Type	Hours	Events(k)
Ar	29.6	43,955	Ar	13.5	73,176
Ti	12.5	12,755	Ti	8.6	28,423
Dummy	0.75	955	Dummy	0.6	2,948
Kin2			**Kin4**		
Target Type	Hours	Events(k)	Target Type	Hours	Events(k)
hline Ar	32.1	62,981	Ar	30.9	158,682
Ti	18.7	21,486	Ti	23.8	113,130
Dummy	4.3	5,075	Dummy	7.1	38,591
Optics	1.15	1,245	Optics	0.9	4,883
C	2.0	2,318	C	3.6	21,922
Kin5			**Inclusive**		
Target Type	Hours	Events(k)	Target Type	Minutes	Events(k)
Ar	12.6	45,338	Ar	57	2,928
Ti	1.5	61	Ti	50	2,993
Dummy	5.9	16,286	Dummy	56	3,235
Optics	2.9	160	C	115	3,957

Table 2.3: Kinematic settings for (e,e′p) measurements, the central kinematic variables include beam energy (E_e), central momenta ($E_{e'}$, P_p), central angles (θ_e, θ_p), momentum transfer ($|\vec{q}|$) and central missing momentum (p_m).

(e,e′p)	$E_e(MeV)$	$E_{e'}$(MeV)	$\theta_e(°)$	$P_p(MeV/c)$	$\theta_p(°)$	$\|\vec{q}\|$(MeV/c)	p_m(MeV/c)
kin 1	2,222	1,777	21.5	915	-50.0	857.5	57.7
kin 3	2,222	1,799	17.5	915	-47.0	740.9	174.1
kin 4	2,222	1,799	15.5	915	-44.5	658.5	229.7
kin 5	2,222	1,716	15.5	1,030	-39.0	730.3	299.7
kin 2	2,222	1,716	20.0	1,030	-44.0	846.1	183.9

Table 2.4: Kinematic settings for (e,e′) measurements, the central kinematic variables include beam energy (E_e),central momentum ($E_{e'}$), central angle (θ_e).

$E_e(MeV)$	2,222								
$\theta_e(°)$	15.54								
$E_{e'}(MeV)$	1,317	1,401	1,490	1,585	1,686	1,794	1,909	2,030	2,160

Chapter 3

First Measurement of the Ti$(e, e')X$ Cross Section at Jefferson Lab

The work described in this chapter was published as:

Hongxia Dai, Matt Murphy, Vishvas Pandey, et al, (The Jefferson Lab Hall A Collaboration), "First measurement of the Ti$(e, e')X$ Cross Section at Jefferson Lab," *Phys. Rev. C*, **98**, 014617 (2018) [83].

Reproduced with permission from the American Physical Society. Copyright (2019) by the American Physical Society.

I contributed the main data analysis work in this paper under Professor Camillo Mariani's supervision.

3.1 Introduction

The interpretation of the data collected by experimental studies of neutrino oscillations demands a fully quantitative description of neutrino interactions with the atomic nuclei comprising the detector [30]. Current and future neutrino experiments, such as the short- (SBN) [31] and the long-baseline (DUNE) [32] neutrino programs, will use detectors based on the liquid-argon time-projection chambers (LArTPCs) technology. In order to achieve

the precision goals of these programs, the treatment of nuclear effects, which has been recognized as a major source of systematic uncertainty in ongoing experiments [33], has to be addressed. Realistic models of both neutrino- and antineutrino-argon interactions will be even more critical to future experiments, such as DUNE, aimed at pinning down charge-parity (CP) symmetry violation in the leptonic sector, because its determination with few percent precision requires accurate measurements of both neutrino and antineutrino oscillations. Failing to achieve this goal in a timely manner will deeply affect the sensitivity of DUNE to measure the CP violating phase (δ_{CP}), as discussed in [34].

Since the description of nuclear effects in a non isospin-symmetric nucleus, such as argon, must take into account the differences in the shell-model states occupied by protons and neutrons, and the information on neutrons cannot be directly extracted, one has to resort to studies of titanium nucleus. Owing to the fact that the neutron spectrum of $^{40}_{18}$Ar is mirrored by the proton spectrum of Ti, the Ti data will give access to the neutron spectral function of argon. Given the scarcity of electron-argon scattering experiments—the only available data on argon being the inclusive spectrum measured at Frascati National Laboratory using the electron-positron collider ADONE and a jet target [35]—we performed a dedicated experiment at Jefferson Lab (JLab), aimed at measuring inclusive and exclusive cross-sections on both argon and titanium targets, and extracting the proton [via Ar$(e, e'p)$] and neutron [via Ti$(e, e'p)$)] spectral functions of the argon nucleus in the kinematical region in which shell-model dynamics is dominant [18].

Electron-scattering experiments have provided a wealth of information on the nuclear response to electromagnetic interactions over a broad kinematic regime. Static form factors and charge distributions have been extracted from elastic scattering data, while measurements of inelastic cross sections have allowed for systematic studies of the dynamic response functions, which shed light on the role played by different reaction mechanisms. Finally, with

the advent of continuous beam accelerators, a number of exclusive processes have been analyzed to unprecedented precision. The availability of the body of electron-nucleus scattering data has been essential to the development of theoretical models. Most notably, experimental studies of the $(e, e'p)$ process—in which the scattered electron and the knocked-out proton are detected in coincidence—have provided detailed information on proton spectral functions [36, 37, 38, 39], the knowledge of which is needed to obtain the nuclear cross sections within the factorization scheme underlying the impulse approximation (IA). The description based on the IA and the spectral function formalism [40] has been successful in describing inclusive electron-scattering data in a variety of kinematic regimes [41, 42, 43], and has recently been be extended to the analysis of neutrino scattering [44, 45, 46, 47]. However, due to the scarcity of available inclusive cross sections for argon and titanium, theoretical models of nuclear effects in electroweak interactions [48, 49, 50, 51, 52, 53, 54] cannot be currently validated in the kinematical region relevant for neutrino experiments.

The experiment E12-14-012 planned to perform a combined analysis of Ar and Ti inclusive and exclusive reactions collected high statistics data in JLab Hall A during February-March 2017. Here, we report the first results of the experiment, including the $\mathrm{Ti}(e, e')X$ cross section at beam energy $E = 2.222$ GeV and electron scattering angle $\theta = 15.541$ deg and the corresponding electron-carbon cross section. Note that this is the first double differential $\mathrm{Ti}(e, e')X$ cross section measured at the kinematics relevant for neutrino experiments, the previous studies on titanium target include [55, 56, 57]. The measurement of the $\mathrm{C}(e, e')X$ cross section allowed a comparison with previous experiments, as well as a careful study of systematic uncertainties. In the (e, e') process $e + A \to e' + X$, an electron of four-momentum $k \equiv (E, \mathbf{k})$ scatters off a nuclear target A. The energy and emission angle of the scattered electron of four-momentum $k' \equiv (E', \mathbf{k}')$ are measured, while the hadronic final state is left undetected. The squared four-momentum transfer in the process is $q^2 = -Q^2$, with

$q = k - k' \equiv (\omega, \mathbf{q})$.

3.2 Experimental Setup

The electron beam was provided by the Continuous Electron Beam Accelerator Facility (CEBAF) at JLab, with currents in excess of 10 μA. The beam current was monitored using two Beam Current Monitors (BCMs), which are resonant radio-frequency cavities. The position of the beam was monitored by two similar cavity types, Beam Position Monitors (BPMs). Beam size was measured with harp scanners, which also allowed the cavity monitor calibration. Beam position determination is important for vertex reconstruction and momentum calculation of the scattered electron. The beam was rastered, with a 2 mm $\times$ 2 mm raster system, in both vertical and horizontal directions, to reduce the beam current density and hence eliminate the possibility of melting the solid foil targets and minimize the local heating of the cryogenic hydrogen target. Both the carbon and titanium targets were foils of natural isotope composition, with a thickness of 0.167$\pm$0.001 g/cm^2 and 0.729$\pm$0.001 g/cm^2, respectively.

The scattered particles were momentum analyzed by two nearly identical spectrometers—the Left and a Right High-Resolution Spectrometers (HRSs)—equipped with detectors for tracking, timing and particle ID. The HRSs consist of 4 magnets (3 superconducting and 1 resistive) in a QQDQ configuration, where the Q indicates a quadrupole magnet and the D indicates a dipole magnet. This arrangement provided a large acceptance for both the angle and momentum, with a relative momentum resolution of $\sim 10^{-4}$, and pointing accuracy and angular resolution of $\sim 10^{-4}$ m and $\sim$10 mrad, respectively. The detector package, slightly updated with respect to the one in Ref. [17], consisting of vertical drift chambers (VDCs), threshold Čerenkov counters, scintillator detectors and a lead-glass calorimeters, provides

data-acquisition triggering, tracking, and particle identification.

The scattered electrons were detected in the Left HRS positioned at $\theta = 15.541$ deg. The data acquisition was triggered, with an efficiency of 99.9%, when an electron fired the two scintillator detectors planes (with a logical AND) simultaneously with a signal in the gas Čerenkov detector. The electrons were identified by a gas threshold Čerenkov detector, mounted between two scintillator detector planes, with 99.9% efficiency and negligible pion contamination. The track trajectories were reconstructed in the detector stack using the VDCs with efficiencies of $\sim 95\%$ for C and $\sim 92\%$ for Ti, and then transported to the target utilizing a fitted reconstruction matrix obtained from a special optics calibration run. We required only one VDC track reconstructed in the final state for simplicity and purity purposes. The number of VDC reconstructed tracks in the case of the Ti target is slightly higher than for the C target, the difference in respective VDC efficiencies was as expected.

3.3 Data Analysis

The cross section is extracted first computing the yield defined in both data and simulation as:

$$\text{Yield}^i = (N_S^i \times \text{DAQ}_{\text{pre-scale}})/(N_e \times LT \times \epsilon). \tag{3.1}$$

Here, i is the ith bin in E', N_S^i represents the number of scattered electrons, N_e is the total number of electrons on the target, LT is the live-time, ϵ is the total efficiency and $\text{DAQ}_{\text{pre-scale}}$ is a factor that determines what fraction of the events gets recorded. The cross section in each bin i is computed as the product of the Monte Carlo (MC) cross section [58] times the ratio of the data to simulation yields. The MC cross section is a fit to existing data, including preliminary Hall C [59] data and includes radiative corrections computed using the peaking approximation [60] and Coulomb corrections implemented with an effective

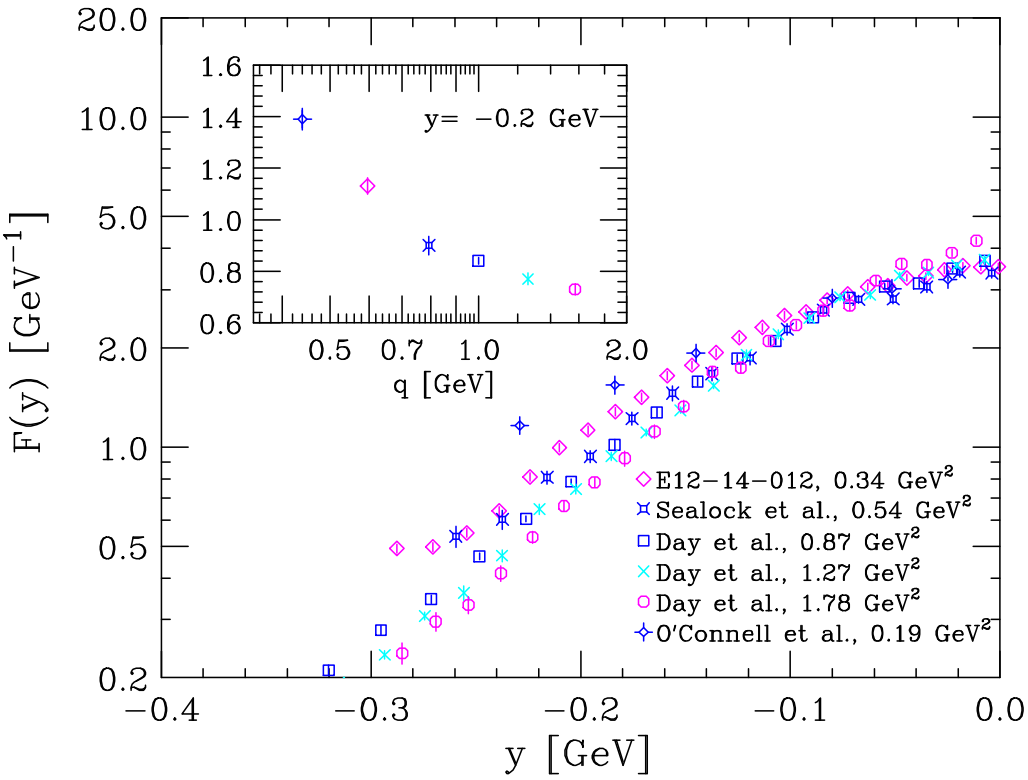

Figure 3.1: (color online). Comparison between the scaling function $F(y)$ obtained from the E12-14-012 data on C, represented by diamonds, and those obtained from the data of O'Connell *et al.* [65], Sealock *et al.* [66], and Day *et al.* [67]. The inset shows the momentum transfer dependence of $F(y)$ at fixed $y = -0.2$ GeV. The data sets are labeled by the value of Q^2 corresponding to the top of the quasielastic peak.

momentum approximation [61].

3.4 Experimental Results and Discussion

Over nearly five decades, a number of measurements of the electron-carbon cross section have been performed at different electron-scattering facilities around the world. A compilation of the available inclusive data can be found in Ref. [62]. In order to put our results in perspective, in Fig. 3.1 we compare the y-scaling function [63], $F(y)$, obtained from the

cross section measured by the E12-14-012 experiment to those obtained from the data of Refs. [65, 66, 67], spanning a kinematical range corresponding to $0.20 \lesssim Q^2 \lesssim 1.8$ GeV^2. The occurrence of scaling in the variable, i.e. the observation that $F(y)$ becomes independent of the momentum transfer $|\mathbf{q}|$ in the limit of large $|\mathbf{q}|$, indicates that quasielastic scattering is the dominant reaction mechanism and final state interactions (FSI) between the knocked out nucleon and the residual nucleus are negligible. The scaling variable y, whose definition is given in Ref. [63], can be loosely identified with the component of the initial nucleon momentum parallel to the momentum transfer.

The main panel of Fig. 3.1 clearly shows that the data exhibit a remarkable scaling behavior at $y \approx 0$, corresponding to $\omega \approx Q^2/2M$, where M is the nucleon mass, while sizable scaling violations, to be mainly ascribed to FSI, are observed at large negative values of y. The momentum transfer dependence of $F(y)$ at $y = -0.2$ GeV, illustrated in the inset, demonstrates that in the kinematical setup of our experiment, corresponding to $|\mathbf{q}| \approx 600$ MeV, the effects of FSI are still significant. Overall, Fig. 3.1 shows that our results are fully consistent with those of previous experiments.

Table 3.1: Contributions to the uncertainties associated with the measured C(e, e') cross sections. Numbers represents upper limit or range for the uncertainties that vary between kinematical regions.

1. Total statistical uncertainty	1.2%
2. Total systematic uncertainty	2.0–2.9%
a. Beam charge & Beam Energy	0.3%
b. Beam offset x&y	0.1%–0.4%
c. Target thickness	0.1%–0.4%
d. HRS offset x&y + Optics	1.3%–2.0%
e. Acceptance cut(θ,ϕ,dp/p)	1.0%–1.4%
f. Calorimeter & Čerenkov cuts	0.01%–0.02%
g. Cross Section Model	0.1%–0.2%
h. Radiative +Coulomb Corr.	1.0–1.3%

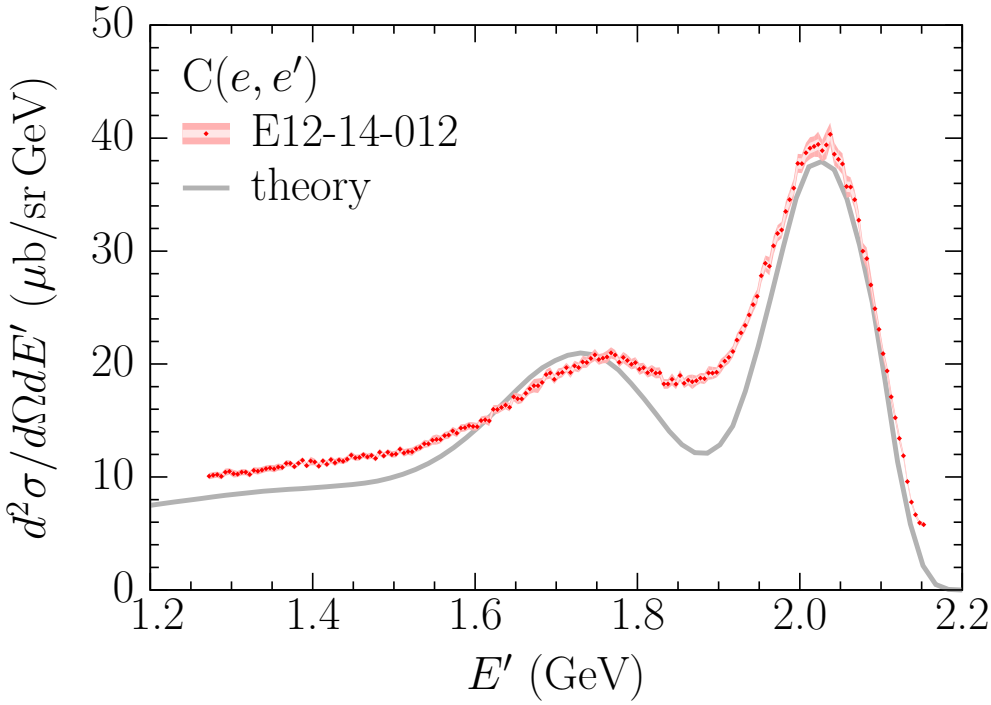

Figure 3.2: (color online). Double differential cross section for the C(e, e') process measured at beam energy of 2.222 GeV and scattering angle of 15.541 deg. The inner and outer uncertainty bars correspond to statistical and total uncertainties, respectively. The solid line represents the theoretical results obtained within the formalism described in Refs. [40, 42, 43, 72].

Figure 3.2 shows the measured C(e, e') cross section as a function of the energy of the scattered electron, ranging from ∼1.2 GeV to ∼2.2 GeV with error bars up to ∼2.5%, corresponding to the statistical (1.2%) and systematic (2.2%) uncertainties summed in quadrature. It can be seen that the kinematical coverage includes both the quasielastic and delta-production peaks, and extends to the region in which the contribution of deep-inelastic scattering becomes appreciable. The statistical uncertainty includes beam charge (0.03%), detector and trigger efficiencies (0.1%), DAQ live-time (0.02%), VDC, and VDC track reconstruction efficiencies (0.1%) and uncertainties due to the charge-symmetric background prediction [68] (0.01%). A detailed list of the systematic uncertainties is given in Table 5.2. All uncertainties are considered as fully uncorrelated. This new high precision C(e, e') data not only

allowed us to carefully test our analysis framework and study systematics but also provides a vital information for the neutrino experiments that use carbon targets such as the long-baseline neutrino experiment T2K [69], NOvA [70] and neutrino interaction experiment MINERvA [71].

The solid line of Fig. 3.2 represents theoretical results obtained within the scheme described in Refs. [40, 42, 43, 72], based on the factorization *ansatz* dictated by the IA and the spectral function formalism. Note that this approach does not involve any adjustable parameters, and allows for a consistent inclusion of single-nucleon interactions—both elastic and inelastic—and meson-exchange current (MEC) contributions. The effects of FSI on the quasielastic cross section has been taken into account following the procedure developed in Ref. [72]. A detailed account of the calculation of the electron-carbon cross section will be provided in a forthcoming paper [73].

Figure 3.3 presents the inclusive electron-titanium cross section, measured at the same kinematics as for carbon and with an error up to ∼2.75%, sum in quadrature of statistical (1.65%) and systematic (2.2%) uncertainties. In the absence of any previous electron-scattering studies carried out using a titanium target, we determined the Ti(e, e') cross sections using:

$$\left(\frac{d^2\sigma^{\text{Born}}}{d\Omega dE'}\right)^i_{\text{Ti}} = \left(\frac{d^2\sigma^{\text{Born}}}{d\Omega dE'}\right)^i_{\text{C}} \times \frac{\text{Yield}^i_{\text{Ti}}}{\text{Yield}^i_{\text{C}}} \tag{3.2}$$

where $\text{Yield}^i_{\text{C/Ti}}$ denotes the luminosity normalized yield respectively for C and Ti. By normalizing the yield ratio to published radiatively unfolded carbon cross sections $d\sigma^{\text{Born}}_C$, we are implicitly unfolding bremsstrahlung from the quoted Ti cross sections. In this approach, most of the systematic uncertainties are fully correlated between C and Ti, due to the fact that the data was collected in the same kinematical setup and analyzed using the same cuts of the carbon data. Uncertainties due to radiative corrections, target thickness and density

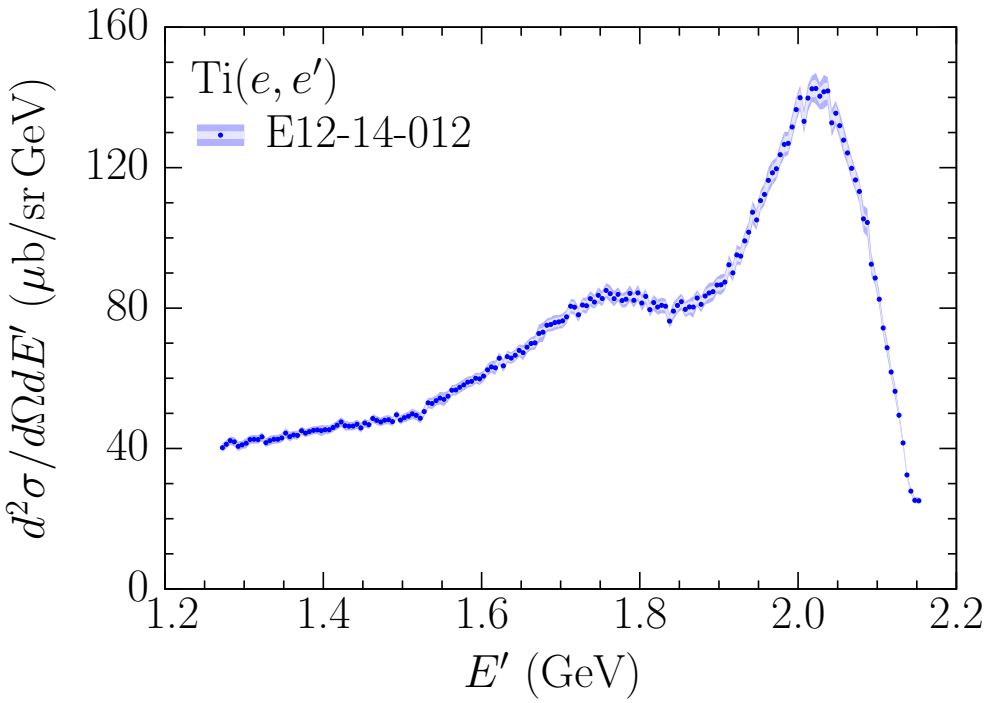

Figure 3.3: (color online). Double differential cross section for the Ti(e, e') process measured at beam energy of 2.222 GeV and fixed scattering angle of 15.541 deg. The inner and outer uncertainty bars correspond to statistical and total uncertainties, respectively. The maximum uncertainties in the full kinematical range are provided.

were evaluated independently for Ti, and added in quadrature to the uncertainties from C. Note that this is the first electron-titanium scattering data collected at the kinematics relevant for neutrino experiments. Therefore, the model of Refs. [40, 42, 43, 72], requiring as an input the target spectral function, could not be used to obtain theoretical results comparable to the data of Fig. 3.3.

Figure 3.4 shows the ratio

$$(d^2\sigma/d\Omega dE')/[Z\sigma_{ep} + (A - Z)\sigma_{en}] \ , \tag{3.3}$$

for carbon and titanium,. Here σ_{ep} and σ_{en} denote the elastic electron-proton and electron-neutron cross sections stripped of the energy-conserving delta function. The difference be-

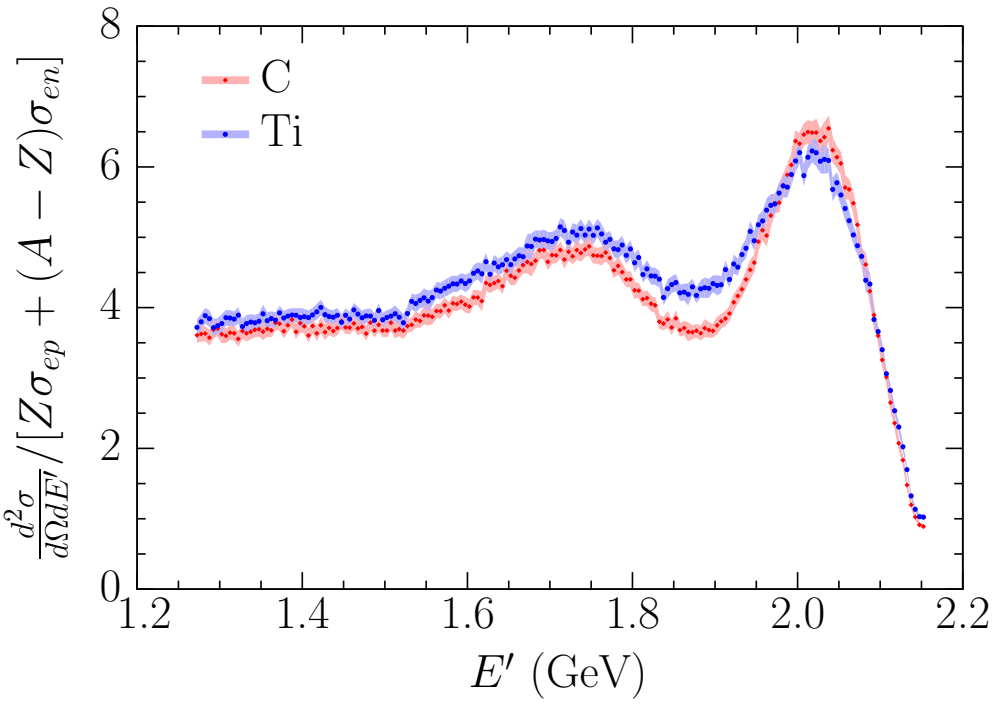

Figure 3.4: (color online). Ratios defined by Eq.(5.6), computed using the measured carbon and titanium cross sections.

tween the results obtained using the measured carbon and titanium cross sections reflect different nuclear effects, that can be conveniently parametrized in terms of a nuclear Fermi momentum exploiting the concept of scaling of second kind, or superscaling [74]. The superscaling analysis of our data, illustrated in Fig. 5.10, suggests that the Fermi momentum in titanium is ∼240 MeV, to be compared to 220 MeV in carbon [75].

3.5 Summary and Conclusions

In this Letter, we have reported the first results of JLab experiment E12-14-012, consisting of the Ti(e, e') and C(e, e') cross sections at beam energy $E = 2.222$ GeV and scattering angle θ =15.541 deg. The quality of the CEBAF electron beam and the excellent performances of the high resolution spectrometer and detector packages available in Hall A allowed for a

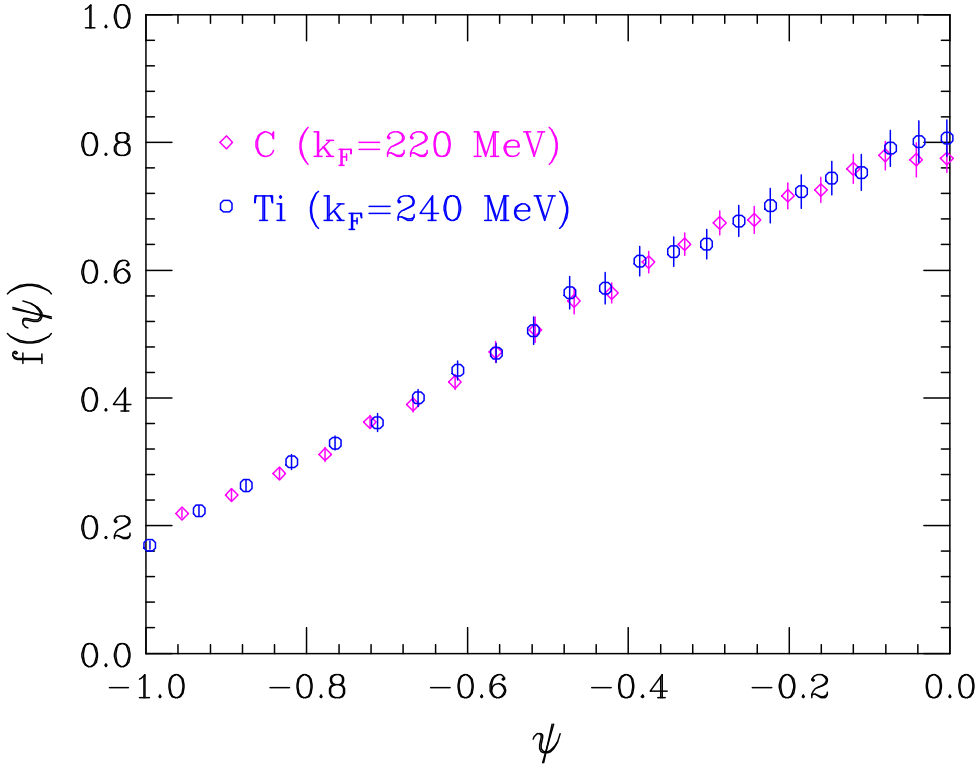

Figure 3.5: (color online). Comparison between the scaling function of 2nd kind, $f(\psi)$, obtained from the E12-14-012 data on C and Ti, represented by diamonds and circles, respsctively. The Fermi momentum of carbon has been fixed to the value obtained by Moniz *et al.* [75]. The data analysis for Ti sets the Ti Fermi momentum at ∼240 MeV.

quick and smooth data taking, and an accurate determination of the cross sections over the broad range of energy transfer in which quasielastic scattering—induced by both one- and two-nucleon currents—and resonance production are the main contributions to the inclusive cross sections.

Our titanium measurement, providing first electron-titanium scattering data at the kinematics relevant for neutrino experiments, will be of great value for the development of realistic models of the electroweak response of neutron-rich nuclei, which will be indispensable for the analysis of the next generation of neutrino oscillation studies employing argon detectors

such as DUNE. Our carbon measurements provide a high precision data that can be utilized in the neutrino experiments that use carbon targets such as T2K, NOvA and MINERvA. Comparison between the results of theoretical calculations and carbon data confirms that the approach based on the spectral function formalism, supplemented by the inclusion of MEC and FSI contributions, provides a consistent framework, capable of providing a *parameter free* description of electron-nucleus scattering in the kinematical regime in which the IA is expected to be applicable.

We acknowledge the outstanding support from the Jefferson Lab Hall A technical staff, target group and Accelerator Division. The authors are indebted to N. Rocco for carrying out the calculation of the MEC contribution to the electron-carbon cross section shown in Fig. 3.2. This experiment was made possible by Virginia Tech and the National Science Foundation under CAREER grant No. PHY−1352106. This work was also supported by the DOE Office of Science, Office of Nuclear Physics, contract DE-AC05-06OR23177, under which Jefferson Science Associates, LLC operates JLab, DOE contracts DE-FG02-96ER40950 and DOE contracts DE-AC02-76SF00515.

Chapter 4

First Measurement of the Ar$(e, e')X$ Cross Section at Jefferson Lab

The work described in this chapter was published as:

Hongxia Dai, Matt Murphy, Vishvas Pandey, et al, (The Jefferson Lab Hall A Collaboration), "First measurement of the Ar$(e, e')X$ Cross Section at Jefferson Lab," *Phys. Rev. C*, **99**, 054608 (2019) [92].

Reproduced with permission from the American Physical Society. Copyright (2019) by the American Physical Society.

I contributed the data analysis work in this paper under Professor Camillo Mariani's supervision.

4.1 Introduction

Precise determination of charge-parity (CP) symmetry violation in the lepton sector—necessary to shed light on the matter-antimatter asymmetry in the Universe—is among the highest priorities of particle physics. Over the next two decades, this issue will be a primary science goal of the Deep Underground Neutrino Experiment (DUNE) [76], together with a search for proton decay, measurement of the electron-neutrino flux from a core-collapse

supernova—should one occur in our galaxy during the lifetime of DUNE—and search for physics beyond the standard model.

In the next few years, the Short-Baseline Neutrino (SBN) program [31] at Fermilab will provide definitive answer to the question of existence of sterile neutrinos, which could be the source of electron-like events recently reported with statistical significance 4.8σ by the MiniBooNE collaboration [77].

Both DUNE and SBN program (will) employ liquid-argon time-projection chambers as their detectors, the advantages of which are low threshold momenta for particle detection and high spatial resolution, allowing (among others) for precise neutrino-energy reconstruction and distinguishing photons from electrons. As a consequence, the success of both programs in studying neutrino oscillations with unprecedented precision will greatly rely on the precision with which we understand the complexity of nuclear effects in argon and the precision with which we are able to estimate its response to electroweak probes.

It is important to realize that, although the near detector facilities of DUNE will play a fundamental role in the reduction of systematic uncertainties, yet alone they will not be sufficient to determine the cross sections with the precision necessary to achieve the objectives of DUNE [32]. At beam energies in the few-GeV region, the observed event kinematics cannot be readily translated to the true value of neutrino energy, owing to detector effects, and the procedure of energy reconstruction heavily relies on the nuclear model used in Monte Carlo (MC) simulations [78]. Even for functionally identical near and far detectors, the spectrum reconstructed in the near detector is very different from the one in the far detector. This is a consequence of not only neutrino oscillations, but also of differences in particle containment and angular acceptance, and of the strong angular dependence of the flux, which makes important the difference between the solid angle probed by near and far detectors, even in absence of the oscillations. As CP-violation sensitivity of DUNE critically

depends on systematic uncertainties, even their modest reduction has a meaningful impact on the running time necessary to achieve the physics objectives.

In the ongoing oscillation experiments [79, 80], the uncertainties related to nuclear effects in neutrino-nucleus interactions have become one of the major sources of systematics [30, 81], despite extensive use of near-detector data to constrain the nuclear models employed in MC simulations. As different probe's energies and reaction mechanisms are intertwined in neutrino-scattering data, it is difficult to identify, diagnose, and remedy potential shortcomings of nuclear models. On the other hand, electron-scattering measurements with targets and kinematics of interest to neutrino experiments give an excellent opportunity to validate and improve the description of nuclear effects [82]. Considering that there is a large body of electron-scattering data available for carbon (and limited availability of data for oxygen) the situation for argon is woefully inadequate, with only one dataset currently available: the inclusive electron-scattering spectrum measured at Frascati National Laboratory (LNF) using the electron-positron collider ADONE and a jet target at incident electron energy $E = 700$ MeV and scattering angle $\theta = 32$ deg [35]. Argon can be expected to be more challenging to describe than oxygen and carbon, as a significantly heavier nucleus that is additionally isospin asymmetric. This asymmetry is of fundamental importance for the CP-violation measurement in DUNE, to be based on analysis of the difference between the neutrino and antineutrino event distributions. Availability of a new precise dataset for electron scattering off argon is therefore vital, in order to provide a testbed and stimulate further development of theoretical models of nuclear response to electroweak interactions [42, 43, 47, 48, 49, 50, 51, 52, 53, 54] in the kinematic region of interest to neutrino experiments.

To address this issue, we performed a dedicated experiment at Jefferson Lab (JLab) to study electron scattering from argon and titanium nuclei [18]. The experiment, E12-14-012,

collected high statistics data in JLab Hall A during February-March 2017. We have recently reported Ti$(e, e')X$ and C$(e, e')X$ cross section results [83]. Here, we present the first argon results of the experiment, Ar$(e, e')X$ cross section at beam energy $E = 2.222$ GeV and electron scattering angle $\theta = 15.541$ deg, and its comparison with our previously reported cross sections for the titanium and carbon nuclei in the same kinematics [83].

In the analyzed (e, e') process, $e + A \to e' + X$, an electron of four-momentum $k \equiv (E, \mathbf{k})$ scatters off a nuclear target A. The energy and scattering angle of the outgoing electron of four-momentum $k' \equiv (E', \mathbf{k}')$ are measured while the hadronic final state remains undetected. The squared four-momentum transfer in the process is $q^2 = -Q^2$, with $q = k - k' \equiv (\omega, \mathbf{q})$.

4.2 Experimental Setup

A continuous-wave electron beam of energy $E = 2.222$ GeV was supplied by the Continuous Electron Beam Accelerator Facility (CEBAF) at JLab. The current and position of the beam, the latter being critical for vertex reconstruction and momentum calculation of scattered electrons, were monitored by resonant radio-frequency cavities (Beam Current Monitors or BCMs) and cavities with four antennae (Beam Position Monitors or BPMs), respectively. Harp scanners, which moved a thin wire through the beam, were used to measure its size. To eliminate the possibility of overheating the target by the deposited beam energy, the beam was rastered with a 2 mm $\times$ 2 mm raster system, to increase the effective spot size and reduce the energy density.

The gaseous argon target, with a thickness of 1.455 ± 0.005 g/cm^2, was contained in a 25 cm long cell with thin aluminum entry and exit windows of respectively 0.25 mm and 0.28 mm thickness. In order to account for the background contribution from electrons scattered from the wall of the argon target cell measurements were also performed on a dummy tar-

get, aluminum foils mounted on separate frames located at positions corresponding to the entry and exit windows of the cell. The thickness of the entry and exit aluminum foils was 0.8886±0.002 g/cm^2 and 0.8893±0.002 g/cm^2, respectively and matched the radiation length of the argon target.

The scattered electrons were detected in the Left High-Resolution Spectrometer (LHRS) positioned at $\theta = 15.541$ deg. The LHRS was equipped with superconductive magnets and a detector package for tracking, timing and particle identification [17, 84]. The scattered electrons first passed through three superconducting quadrupole magnets (Q) and one dipole magnet (D) arranged in QQDQ configuration. This arrangement provided a large acceptance in both angle and momentum, and good resolution in momentum ($\sim 10^{-4}$), position ($\sim 10^{-3}$ m) and in angle ($\sim$1.0 mrad). The electrons then entered the detector package consisting of vertical drift chambers (VDCs), threshold Čerenkov counter, scintillator detectors and a lead-glass calorimeter. The data-acquisition (DAQ) electronics was triggered when an electron passes through two scintillator detectors planes (with a logical AND) and simultaneously produces a signal in the gas CO_2 Čerenkov counter, mounted between the two scintillator planes. Electron/pion separation is achieved with the combined amplitude response of the gas Čerenkov and Pb-Glass shower counters. The tracking information (position and direction) was reconstructed in the VDCs utilizing a reconstruction matrix obtained from special optics-calibration runs.

4.3 Data Analysis

The electron yield (Y) for ith bin in scattered electron energy (E') is obtained as

$$Y^i = (N_S^i \times DAQ_{\text{pre-scale}})/(N_e \times LT \times \epsilon). \tag{4.1}$$

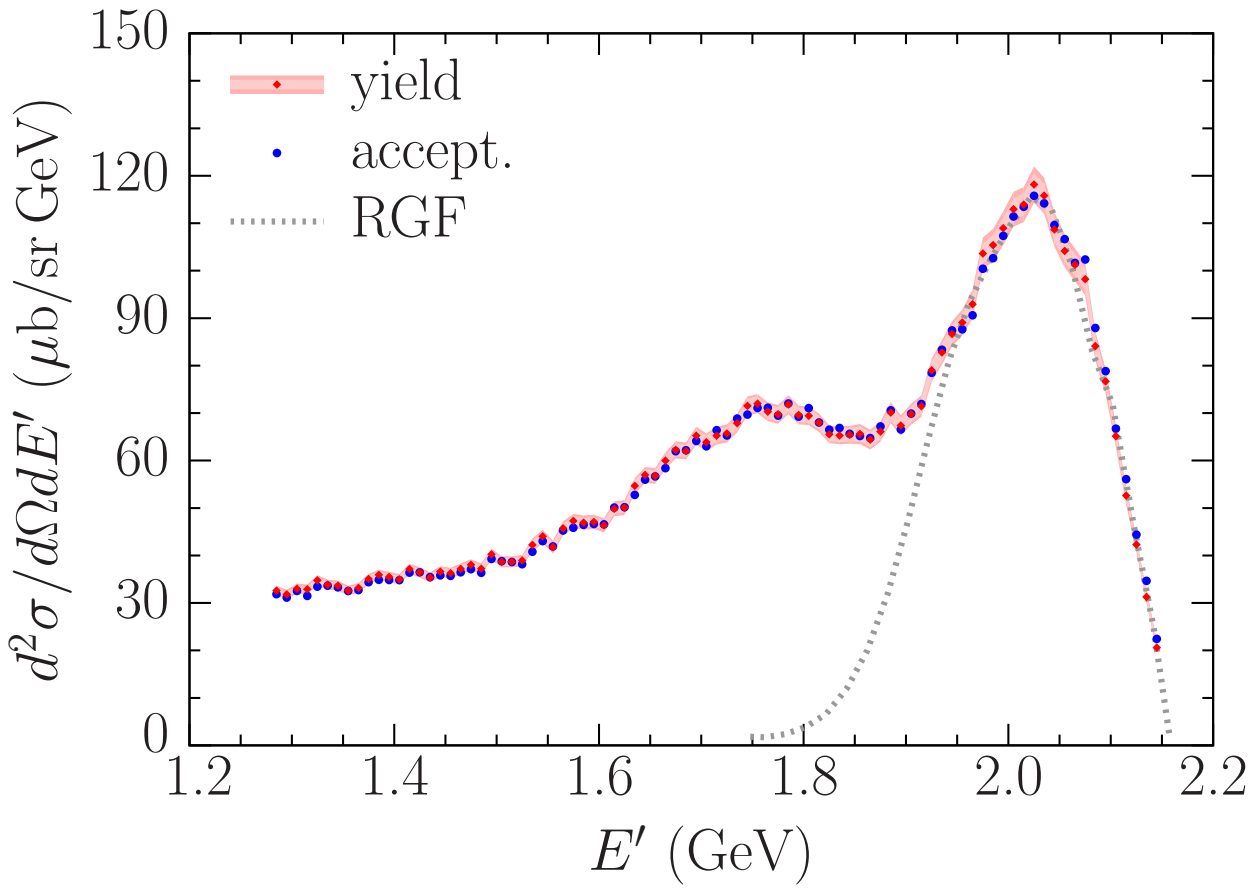

Figure 4.1: (color online). Double differential cross section for the Ar(e, e') process, extracted with two different methods, at beam energy of 2.222 GeV and scattering angle of 15.541 deg. The inner and outer bars correspond to the statistical and total uncertainty, respectively. The dotted curve represents the quasielastic calculations obtained within the relativistic Green's function (RGF) formalism described in Ref. [85].

Here, N_S^i is the number of scattered electrons recorded, N_e is the total number of electrons incident on the target, LT is the live-time fraction, ϵ is the total detection efficiency. The hardware trigger is configured to accept only every $n = DAQ_{\text{pre-scale}}$ raw triggers. The $\sim$10μA beam rastered over 2$\times$2 mm^2 deposits enough energy into the target that its density change must be taken into consideration when extracting the cross section. This is done through a *target-boiling effect* study in which the beam current is ramped in steps from zero current to $\sim$20 μA and the scattering yield determined [27]. From this a correction to the

zero current density can be made and applied to all the runs. The yield is also corrected for the background (∼0.2%) remaining after the dummy cell is subtracted. Once the yield is determined, the cross section can be extracted either by the *acceptance-correction method* or by the *yield-ratio method*.

In the acceptance-correction method, for each bin in $\Delta E \Delta\Omega$, the cross section is obtained as

$$d^2\sigma/d\Omega dE' = Y(E', \theta)/[(\Delta E \Delta\Omega)A(E', \theta)L]. \tag{4.2}$$

Where, $Y(E', \theta)$ and $A(E', \theta)$ are yield and acceptance for a given bin, respectively, and L is the integrated luminosity obtained using a MC and validated with the solid Al target (dummy cell) and C foils (the optics target). In the yield-ratio method, the cross section for each bin is computed as the product of the MC cross section [58] times the ratio of the data to simulation yields

$$d^2\sigma/d\Omega dE' = (d^2\sigma/d\Omega dE')_{\mathrm{MC}} \times [Y(E', \theta)/Y_{\mathrm{MC}}(E', \theta)]. \tag{4.3}$$

The MC cross section is a fit to the existing data including preliminary Hall C data [59]. The MC includes the radiative corrections computed using the peaking approximation [60] and Coulomb corrections implemented with an effective momentum approximation [61], further accounted for the change in radiation length of the target due to the target-boiling effect.

4.4 Experimental Results and Sacling Analysis

Figure 4.1 shows the measured Ar(e, e') double differential cross section as a function of the energy of the scattered electron, E', extracted with the yield-ratio and the acceptance-correction method. Both methods yield the cross-section results in very good agreement,

with marginal differences observed only in the region of E' above the quasielastic peak (i.e. ω below the peak), where the event statistics are limited and the systematic uncertainties of the acceptance method are larger. The primary difference between the two methods is the fact that the yield-ratio method relies more on the predictions of the cross section model in the MC but the agreement of the two methods strengthens our confidence in both procedures. The measured cross section covers a broad range of scattered electron energy ranging from ∼1.3 GeV to ∼2.2 GeV. The kinematical coverage includes both the quasielastic and delta-production peaks, and further extends to the deep-inelastic scattering region. The total uncertainties remain below ∼4.0% corresponding to the statistical (1.7%–2.9%) and the systematic (1.8%–3.0%) uncertainties summed in quadrature. A detailed list of the uncertainties is given in Table 5.2.

Table 4.1: Uncertainties associated with the presented Ar(e, e') cross section. Numbers represent upper limits or the range for the uncertainties that vary between different kinematical regions.

1. Total statistical uncertainty	1.7%–2.9%
2. Total systematic uncertainty	1.8%–3.0%
a. Beam charge & beam energy	0.3%
b. Beam offset x&y	0.4%–1.0%
c. Target thickness and boiling effect	0.7%
d. HRS offset x&y + optics	0.6%–1.2%
e. Acceptance cut (θ,ϕ,dp/p)	0.6%–2.4%
f. Calorimeter & Čerenkov cuts	0.01%–0.03%
g. Cross section model	1.3%
h. Radiative & Coulomb corrections	1.0%

The dotted curve of Fig. 4.1 represents the theoretical results obtained from the relativistic Green's function (RGF) approach described in Ref. [85]. In the RGF formalism, following assumptions based on the impulse approximation, the components of the nuclear response

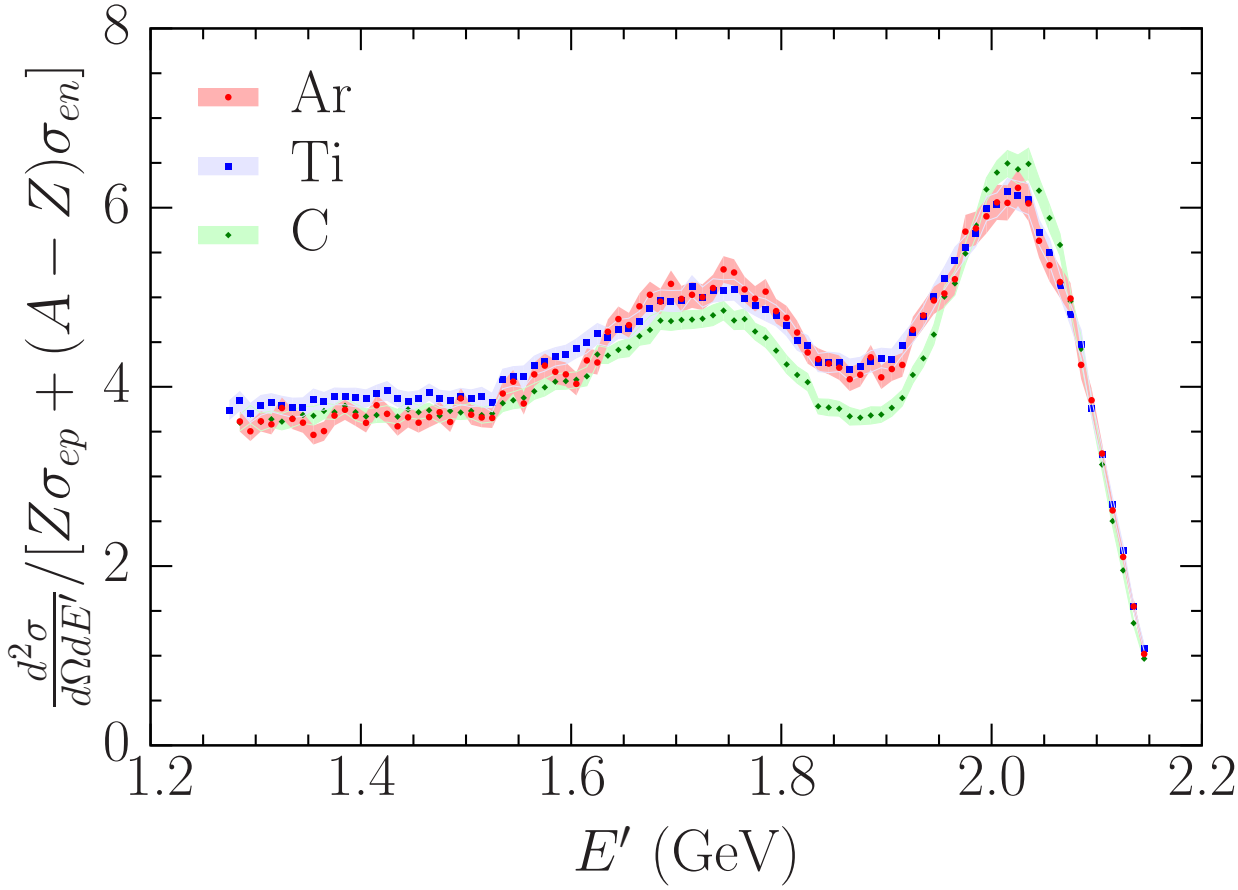

Figure 4.2: (color online). Comparison of Ar(e, e') cross section of Fig. 4.1, and Ti(e, e') and C(e, e') cross sections of Ref. [83], all in the same kinematics, presented in terms of the ratio defined by Eq.(5.6).

are written in terms of the single-particle optical-model Green's function. Final-state interactions are accounted for, consistently with the approach used in the exclusive $(e, e'p)$ reaction, by the same complex optical potential but the formalism translates the flux lost towards inelastic channels, represented by the imaginary part of the optical potential, into the strength observed in inclusive reactions. It is apparent that this procedure leads to a remarkably good description of both shape and normalization of the data in the the quasielastic region. However, it does not include two-body currents and delta-excitation mechanisms which are clearly visible in the region of lower E' values (i.e. larger energy transfers).

In Fig. 4.2, we compare the argon data to the titanium and carbon data of Ref [83], taken in the same kinematical setup, corresponding to incident electron energy 2.222 GeV and scattering angle of 15.541 deg. The comparison is performed in terms of the ratio defined as

$$(d^2\sigma/d\Omega dE')/[Z\sigma_{ep} + (A - Z)\sigma_{en}] \ , \tag{4.4}$$

where A and Z are the nuclear mass number and charge, respectively, while σ_{ep} and σ_{en} denote the elastic electron-proton and electron-neutron cross sections stripped of the energy-conserving delta function [86]. The results of Fig. 4.2, showing that the ratios of Eq.(5.6) corresponding to argon and titanium are nearly identical to one another, appear to support the strategy underlying our experiment, aimed at exploiting titanium data to extract complementary information on nuclear effects in argon. On the other hand, the differences between the results for argon and carbon indicate significant differences in the ground-state properties of these nuclei, which are relevant in the context of MC simulations for DUNE.

To further elucidate the differences between the argon, titanium, and carbon cross sections, in Fig. 5.10, we show the corresponding scaling functions of the second kind, $f(\psi)$, displayed as a function of the dimensionless scaling variable ψ. The definitions of both $f(\psi)$ and ψ involve a momentum scale, which can be loosely interpreted as the nuclear Fermi momentum, k_F [74], providing a simple parametrization of nuclear effects. The results of Fig. 5.10 show that setting the carbon Fermi momentum to 220 MeV—the value resulting from the analysis of Moniz *et al.* [75]—scaling of titanium and argon data is observed for $k_F = 240$ and 245 MeV, respectively. Hence, the scaling analysis confirms the picture emerging from Fig. 4.2. For comparison, we also show the scaling function $f(\psi)$ obtained using the $\mathrm{Ar}(e, e')$ cross section at 700 MeV and 32 deg, measured at the LNF electron-positron storage ring ADONE using a jet target [35]. It turns out that scaling of the LNF data is only observed at $\psi \approx 0$ and prefers a much larger value of the Fermi momentum, k_F=375 MeV, than the

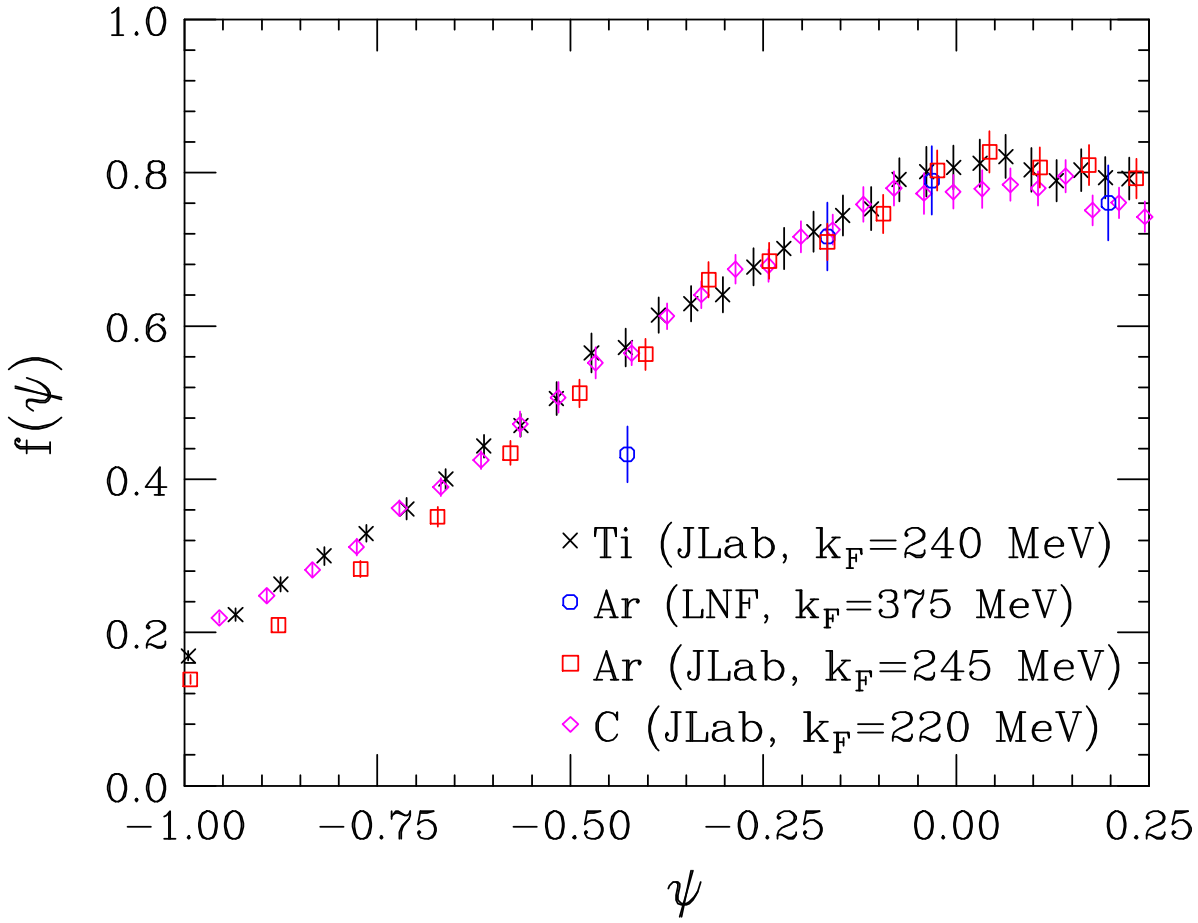

Figure 4.3: (color online). Comparison between the scaling function of the second kind, $f(\psi)$, obtained from E12-14-012 data on Ar, Ti, and C. The k_F of C is fixed to the value obtained by Moniz *et al.* [75] while the data analysis of Ti and Ar sets k_F at 240 MeV and 245 MeV, respectively. The circles are the Ar data from LNF [35], which turn out to prefer an inconsistently higher value of k_F.

one resulting from the analysis of the JLab data. This inconsistency may well be the result of the normalization issue that the authors of Ref. [35] found in their ^{16}O cross section as compared to the previously measured cross section at Bates Linear Accelerator Center [65] which was considered as a reference dataset by the authors of Ref. [35]. A normalization factor of 1.19 is then applied to the ^{16}O cross section to reproduce the Bates spectrum, as quoted in Ref. [35]. Note that the Bates data for oxygen was a result of subtracting cross

sections obtained for BeO and Be targets while the LNF oxygen target was a relatively *pure* jet target. The same normalization factor, 1.19, was then applied to the reported argon cross section leaving room for further disparity. A similar inconsistency is observed also with the analysis of the scaling of the first kind [63]—shown in Fig. 4.4, where the y-scaling function, $F(y)$, obtained from the argon, titanium, and carbon cross section measured by the E12-14-012 experiment, and the argon cross section measured at LNF are compared. Additionally, the RGF calculations of Ref. [85] encounter the same normalization issue with the LNF argon data while they successfully describe the LNF data on ^{16}O [85] and the E12-14-012 argon data in the quasielastic region (Fig. 4.1).

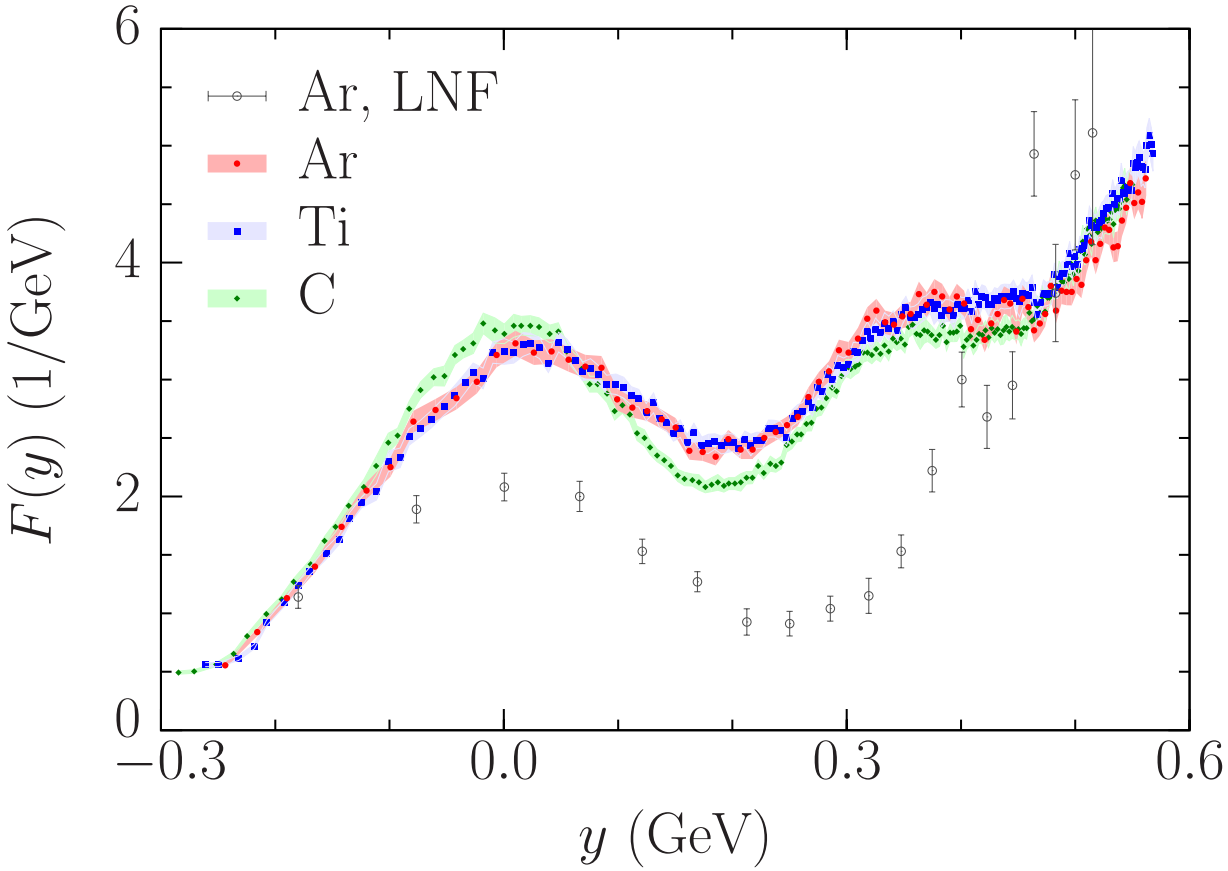

Figure 4.4: (color online). Comparison between the scaling function $F(y)$ obtained from the E12-14-012 data on argon, titanium and carbon, and the argon data obtained at LNF [35].

4.5 Summary

In this Letter, we have reported the first argon results of JLab experiment E12-14-012, as Ar(e, e') cross sections at incident electron energy $E = 2.222$ GeV and scattering angle θ =15.541 deg. The cross section covers a broad range of energy transfer in which quasielastic scattering and resonance production are the dominant mechanisms of interaction. We presented a comparison of Ar(e, e') cross section with previously reported Ti(e, e') and C(e, e') cross sections of our experiment. The new precise measurement on argon nucleus will be of great value for the development of realistic models of the electroweak response of neutron-rich nuclei, vital for the success of the current and next generation of neutrino oscillation studies employing liquid-argon based detectors.

We acknowledge the outstanding support from the Jefferson Lab Hall A technical staff, target group and Accelerator Division. This experiment was made possible by Virginia Tech and the National Science Foundation under CAREER grant No. PHY−1352106. This work was also supported by the DOE Office of Science, Office of Nuclear Physics, contract DE-AC05-06OR23177, under which Jefferson Science Associates, LLC operates JLab, DOE contract DE-FG02-96ER40950 and DOE contract DE-AC02-76SF00515.

Chapter 5

Measurement of the cross sections for inclusive electron scattering in the E12-14-012 experiment at Jefferson Lab

The work described in this chapter was contributed by: Matt Murphy, Hongxia Dai, Linjie Gu, et al, (The Jefferson Lab Hall A Collaboration). It has been submitted to Physical Review C.

I contributed part of the data analysis work in this paper under Professor Camillo Mariani's supervision.

5.1 Introduction

Electron scattering experiments have been shown to be the best tool for precise investigations of the structure of atomic nuclei [87]. The electromagnetic interaction of electrons with the target is weak compared with the strength of interactions that bind nucleons together, and can be treated as an exchange of a single photon. Allowing the nuclear response to be probed

at energy transfers varied independently from momentum transfers, electron beams can be used to investigate physics corresponding to various excitation energies with different spacial resolutions, exposing to different interaction mechanisms.

The existing body of electron-scattering data clearly shows that many important features of nuclear structure can be described assuming that nucleons forming the nucleus behave as independent particles bound in a mean field [88], but this picture is not complete without accounting for correlations between nucleons [89].

While analysis of electron scattering from nuclei is interesting in its own right, accurate description of nuclear effects in interactions of a few-GeV probes is now coming into sharp focus due to its relevance for neutrino physics. As neutrino oscillation parameters are extracted from collected event spectra, and neutrino energies have to be reconstructed from the observed kinematics of the products of their interactions with nuclear targets, nuclear effects play fundamental role in neutrino-oscillation analysis [82].

In neutrino experiments, nuclear models implemented in Monte Carlo (MC) simulations are employed to predict event rate in a near detector, perform its extrapolation to a far detector, estimate the energy carried by undetected particles, and obtain background estimates. While description of nuclear effects is already one of the largest sources of systematic uncertainties in ongoing oscillation studies [90], its importance will increase further in the next generation of oscillation experiments. In particular, to achieve their sensitivity goals, the Deep Underground Neutrino Experiment (DUNE) and Hyper-Kamiokande have to reduce uncertainties coming from nuclear cross sections to a few-percent level [32, 91].

As weak interactions of neutrinos probe nucleus in a very similar way as electromagnetic interactions of electrons, precise electron scattering data give unique opportunity to validate nuclear models employed in neutrino physics. A theory model unable to reproduce electron

measurements cannot be expected to provide accurate predictions for neutrino cross sections.

At the kinematics where the impulse approximation is valid—the process of scattering off a nuclear target can be described as involving predominantly a single nucleon, with $(A-1)$ nucleons acting as a spectator system—nuclear effects can be separated from the description of the elementary cross sections, differing between neutrinos and electrons, and the knowledge gained in electron scattering directly translates to neutrino interactions. In particular, measurements of the $(e, e'p)$ cross sections—in which knocked out protons are detected in coincidence with electrons—can be used to extract the information on the momentum and energy distributions (the spectral function) of protons in the nucleus, and on final-state interactions (FSI) of the struck protons propagating through the (excited) residual nucleus, which are intrinsic properties of the target and do not depend on the interaction mechanism.

In the simplest case of a symmetric nuclear target, with the proton number Z equal to the neutron number N, nuclear effects are expected to be largely the same in neutrino and electron interactions, up to small Coulomb corrections. For an asymmetric nucleus, one needs to additionally analyze electron scattering on its mirror nucleus, with Z and N swapped, to obtain a good approximation of information on the neutron structure, impossible to collect directly. In the case of DUNE, in addition to argon $(Z = 18, N = 22)$—employed as the target material—it is necessary to collect electron scattering data also for titanium $(Z = 22)$. While the exclusive $(e, e'p)$ cross sections give direct insight into the nuclear structure, they do not provide a complete picture of all interaction dynamics.

When the energy transferred by the interacting electron to the nucleon increases, the interaction mechanism changes from quasielastic (QE) scattering, in which the struck nucleon is removed from the nucleus, to nucleon resonance production, dominated by the excitation of the Δ resonance, and finally to deep-inelastic scattering on individual quarks forming nucleons. The inclusive (e, e') measurements, which yield the spectra of electrons scattered

at fixed angle, provide information on all interaction mechanisms, regardless of the composition of hadrons in the final state. As a consequence, a great deal can be learned from the inclusive (e, e') cross sections, particularly in the context of DUNE, in which $\sim$2/3 of events are expected to involve pions [32].

The features of the peaks observed in the inclusive spectrum—their width, position, shape, and height—provide information on the momentum and energy distributions of the nucleons in the nuclear ground state, as well as on the final-state interactions (FSI) between the struck-nucleons and the spectator system. The width of the QE peak, which in the nonrelativistic regime depends on both the momentum carried by the struck nucleon and the momentum transfer, $\mathbf{q}$, in the relativistic regime becomes largely independent of $\mathbf{q}$, and can be simply parametrized in terms of a Fermi momentum, k_F [75]. However, a kinematic-dependent broadening ascribed to FSI is also observed. The position of the QE peak is determined by the combined effects of nuclear binding and FSI, while its pronounced asymmetry is a consequence of multi-nucleon knockout processes, induced by short-range correlations between nucleons in the initial state and by two-body interaction mechanisms, such as those involving meson-exchange currents. The height of the QE peak depends on the number of nucleons probed by the interaction and the momentum and energy distributions of nucleons in the ground state.

The identification of nuclear effects shaping the peak corresponding to QE scattering largely applies to other interaction mechanisms as well. However, their contributions give rise to broader structures in the cross section, as they involve production of hadrons of finite lifetimes.

To provide a reliable foundation for the oscillation analysis of precise long-baseline neutrino experiment, a nuclear model employed in Monte Carlo simulations must be able to reproduce the features of the cross sections for electron scattering corresponding to the kinematics and

target of relevance. In the context of DUNE, beam energies between 2 and 4 GeV play the most important role, and argon is the target material.

Previously [83, 92], we have reported the inclusive cross sections for electron scattering off argon, titanium, and carbon, extracted for beam energy 2.222 GeV and scattering angle 15.54°. Here we present a new result for aluminum, and a complete scaling analysis of all the targets that we have analyzed. We also discuss in more details the procedures used to measure the inclusive cross sections, together with their uncertainty estimates. In Sec. 5.2 we describe the setup of the performed experiment. The methods of extracting the cross sections are presented in Sec. 5.3. The estimates of their uncertainties are covered in Sec. 5.4. In Sec. 5.5 we report and discuss the measured aluminum cross section, while Sec. 5.6 is devoted to the scaling analysis of our data. Finally, in Sec. 5.7 we summarize our findings and draw the conclusions.

5.2 Experimental Setup

Performed at Jefferson Lab, E12-14-012 took both exclusive electron scattering data $(e, e'p)$ in which the proton knocked out from the nuclear target is detected in coincidence with the scattered electron, and inclusive (e, e') data in which all final states contribute, for different targets: C, Ti, Ar and Al. The experiment E12-14-012 used an electron beam of energy 2.222 GeV provided by the Continuous Electron Beam Accelerator Facility (CEBAF), and took data in Spring 2017. The average beam current was 10 μA. Scattered electrons were measured using a high resolution spectrometer (HRS), equipped with two vertical drift chambers (VDCs) providing tracking information [22], two scintillator planes for timing measurements and triggering, double-layered lead-glass calorimeter, and a gas Čerenkov counter used for particle identification [17]. The HRS was positioned with a central scattering an-

gle of $\theta = 15.54°$. The data analysis for inclusive electron scattering is relatively simple, as it implies modest data acquisition (DAQ) rates and very small pion backgrounds. The beam current and position, the latter being critical for the electron-vertex reconstruction and momentum calculation, were monitored by resonant radio-frequency cavities (beam current monitors, or BCMs [17]) and cavities with four antennae (beam position monitors, or BPMs [17]), respectively. The beam size was measured using harp scanners, which moved a thin wire through the beam. The beam was spread over a 2×2 mm^2 area to avoid overheating the target.

The experiment employed a set of solid targets—aluminum, carbon (single foil and a multi-foil composed of 9 foils), and titanium—as well as a closed cell of gaseous argon [27]. The aluminum target consisted of two identical foils of the 7075 alloy, the thickness of which was 0.889 ± 0.002 g/cm^2. Details of the elementary composition of the Al-7075 alloy used in the E12-14-012 experiment are given in Table 5.1. The aluminum foils were positioned to match the entrance and exit windows of the argon target, separated by a distance of 25 cm. Their thickness was fixed to be the same as the radiation length of the argon target. The analysis presented here uses the data from one of the foils only, located upstream of the spectrometers at $z = -12.5$ cm. The data were taken in nine separate runs, modifying at each step the momentum of the spectrometer in order to cover the final electron energy E' from 1.285 to 2.135 GeV.

The VDCs' tracking information allowed the determination of the momentum and reconstruction of the direction (in-plane and out-of-plane angles) of the scattered electron, and reconstructing the interaction vertex at the target. The transformation between focal plane and target quantities was computed using an optical matrix, the accuracy of which was verified using the multi-foil target data. Possible variations of the magnetic field in the HRS magnets that could affect the optics are included in the analysis as systematic uncertainties.

Table 5.1: Composition of the Al-7075 alloy. For each element, we provide the number of protons Z and the average number of neutrons N calculated according to the isotopic abundances [93].

	weight (%)	Z	N
Al	89.72	13	14.00
Zn	5.8	30	35.45
Mg	2.4	12	12.32
Cu	1.5	29	34.62
Fe	0.19	26	29.91
Cr	0.19	24	28.06
Si	0.07	14	14.11
Mn	0.03	25	30.00
Ti	0.03	22	25.92
V	0.01	23	28.00
Zr	0.01	40	51.32
other	0.05		
average		14.26 ± 0.01	15.58 ± 0.01

We set up two types of hardware triggers:

$$T_3 = (S_0 \&\& S_2) \&\& (LC || GC),$$

$$T_5 = (S_0 || S_2) \&\& (LC || GC).$$

The T_3 (T_5) trigger type requires that the signal from the scintillator plane S_0 AND S_2 (S_0 OR S_2) is detected in coincidence with the signal from the lead calorimeter (LC) OR the gas Čerenkov counter (GC).

Electrons were selected in the HRS requiring, in addition, one reconstructed track. Further, they had to deposit 30% of their energy in the lead calorimeter ($E_{\text{cal}}/p > 0.3$). To select events in the central acceptance region of the spectrometer, the electron's track was required to be within ± 4 mrad of the in-plane angle and ± 6 mrad of the out-of-plane angle with respect to the center ray of the spectrometer and have a dp/p of ± 0.04. The spectrometers

were calibrated using sieve slit measurements and the position of the spectrometers and angles were surveyed before the start of the data taking. The survey precision for the angle and position measurements is respectively 0.01 mrad and 0.01 mm.

The efficiencies of the elements in the detector stack were studied by comparing rates in various combinations of secondary triggers. The scintillator efficiency, ($S_0 \& \& S_2$), was studied using the ratio of the events rates selected using T_3 and T_5 trigger types, requiring one reconstructed track, and applying the acceptance and calorimeter cuts. It was found to be 99%. The efficiency of the calorimeters was close to 100% for all runs, the efficiency of the Čerenkov detector was found to range from 99.9% for the highest E' runs down to 97.5% for the lowest E' run. The Čerenkov efficiency was evaluated by selecting a pure sample of electrons in the calorimeter and varying the Čerenkov cut by $\pm 10\%$. The live-time of the electronics, computed using the rates from scalers, which were independent of triggered events, was above 98% for all runs. The acceptance cuts efficiencies ($\sim$98%) and the dp cut efficiency ($\sim$99%) were computed using the MC simulation [58]. The overall efficiency (between 88 and 95% across all the kinematical regions) includes cuts on the calorimeters, both the lead and the Čerenkov counter, track reconstruction efficiency, livetime and acceptance.

5.3 Data Analysis

5.3.1 Yield-Ratio Method

The yield-ratio method of determining the cross section involves both the experimental data and simulated MC data. In this method, the yield Y is calculated for both sets of data as

$$Y^i = (N_S^i \times PS)/(LT \times \epsilon), \tag{5.1}$$

where i refers to the ith bin of the E' distribution, N_S^i is the total number of scattered electrons, PS is a pre-scale factor in the DAQ, ϵ is the total efficiency of the detector, and LT is the livetime of the electronics. The ratio of the yields for the actual and MC data is taken as a means of eliminating any impact of the acceptance on each bin, and then the measured cross section is determined by multiplying this ratio by the cross section calculated within the Monte Carlo model:

$$\frac{d^2\sigma_{\text{data}}}{d\Omega dE'} = \frac{d^2\sigma_{\text{MC}}}{d\Omega dE'} \times \frac{Y_{\text{data}}}{Y_{\text{MC}}}. \tag{5.2}$$

5.3.2 Acceptance Method

The cross section was also extracted via another method, the acceptance method, and both the yield ratio and acceptance methods were examined for agreement. In the case of the argon target, for which an accurate model of the nuclear response is not yet available, it is important to validate the MC simulation and results obtained using the yield ratio method using an alternative method less dependent on the input MC cross section model. The acceptance method will be described in the following of this section.

For each $(\Delta E, \Delta\Omega)$ bin, the number of detected electrons can be determined using

$$N_S^i = L \times \frac{d^2\sigma}{d\Omega dE'} \times \Delta E' \Delta\Omega \times \epsilon \times A^i(E', \theta, \phi) \tag{5.3}$$

where L is the integrated luminosity (number of beam electrons $\times$ number of targets / area), ϵ is the total detection efficiency, and θ and ϕ represent the in-plane and out-of-plane angles, respectively. The acceptance $A^i(E', \theta, \phi)$ is the probability that a particle passes through the spectrometer into the ith bin.

The electron yield corrected for the overall efficiency (product of individual efficiencies as described above) can be cast as

$$\begin{aligned} Y^i &= \frac{N_S^i}{\epsilon} \\ &= L \times \frac{d^2\sigma_{\text{data}}}{d\Omega dE'} \times \Delta E' \Delta\Omega \times A^i(E', \theta, \phi), \end{aligned} \tag{5.4}$$

and the cross section can be measured using

$$\frac{d^2\sigma_{\text{data}}}{d\Omega dE'} = \frac{Y^i}{\Delta E' \Delta\Omega \times A^i(E', \theta, \phi) \times L}. \tag{5.5}$$

The single-arm Monte Carlo simulation was used to generate events uniformly distributed in (θ, ϕ, E'). For a specific phase-space slice in $(\Delta\theta, \Delta\phi, \Delta E')$, we computed the ratio between the total number of events that reach the spectrometer and the number of generated events. The ratio of these two numbers represents the probability that a particle successfully passes through the magnets and the aperture to arrive at the detector package.

For an extended target, an acceptance matrix $A^i(E', \theta, \phi)$ was generated at various points along the target length. Each different target slice was associated with a different $A^i(E', \theta, \phi)$.

The number and size of the slices were optimized based on the statistics of the data. In

principle, an infinite number of matrices could be used in order to make events perfectly weighted, but this method would be inefficient and subject to large statistical fluctuations, if the number of events in each region was limited.

In this analysis, we used a single matrix for events along the entire target length to correct the data, and evaluated the residual variation along the beam direction z. For these studies we took advantage of the optical target data, collected in Spring 2017.

The optical target was a series of nine carbon foils, placed along the beam direction at $z = 0$ cm, ± 2 cm, ± 5 cm, ± 7.5 cm, ± 10 cm, respectively. The z distribution of the events reconstructed from the optical target is shown in Fig. 5.1, with the shaded regions representing the z-position cuts employed to identify the events coming from individual carbon foils. Because it would be difficult to select pure events from each foil, due to its finite thickness, we used the Monte Carlo simulation and the carbon cross-section model to generate single-foil carbon data for different z positions of the target.

Using the single-foil carbon data, we generated 9 acceptance matrices corresponding to the mean z position of each foil composing the multi-foil carbon target. We applied a weight of $1/A(E', \theta, \phi)$ to every event, and made a comparison between the events originating from individual foils. The obtained distribution of MC event yields from different foils, normalized to the one from the foil at $z = 0$ cm, is shown in Fig. 5.2. The results for the 9 regions, represented by the red dots lying inside the green shaded band, are in excellent agreement, with variations between them remaining below 0.5%.

When the same procedure is applied to the reconstructed data events, the obtained event yields—represented by the blue lozenges in Fig. 5.2—exhibit a dependence on the target z position. This behavior is expected due to the variation of the cross section as a function of the electron scattering angle, as foils at different positions have different acceptances,

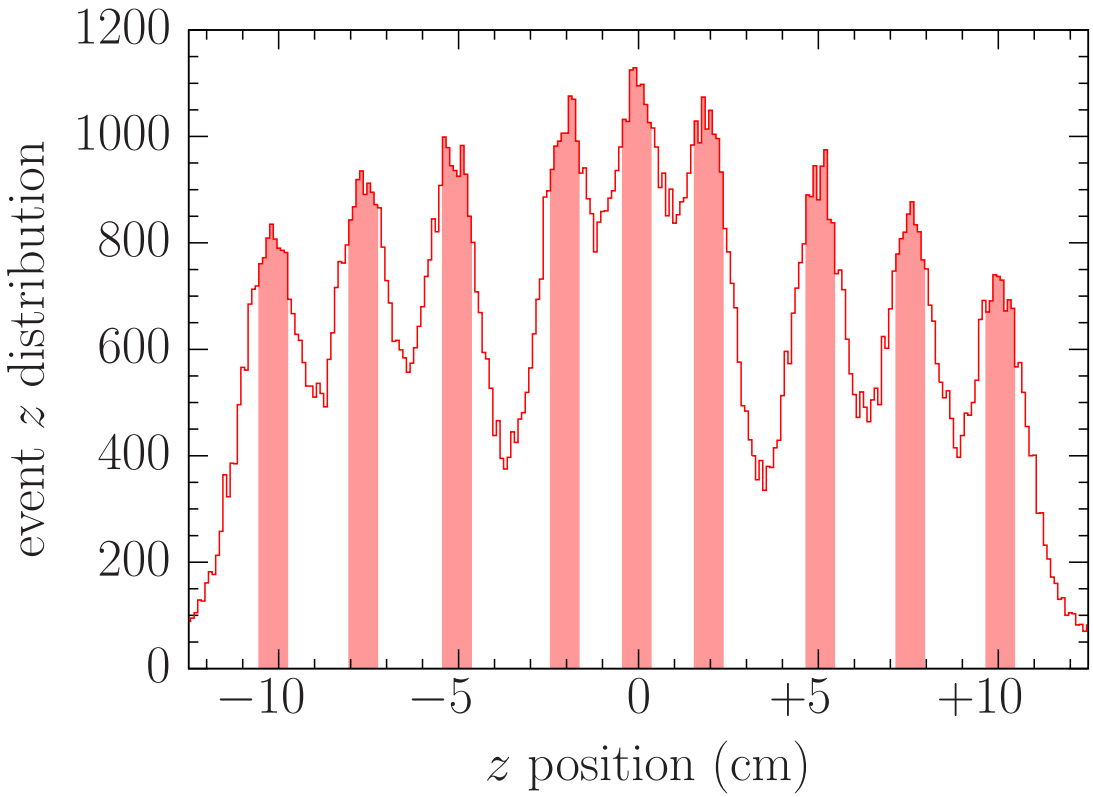

Figure 5.1: (color online). Distribution along the beam direction of reconstructed events for the multi-foil carbon target. The shaded regions represent the data selected to identify the events coming from individual carbon foils.

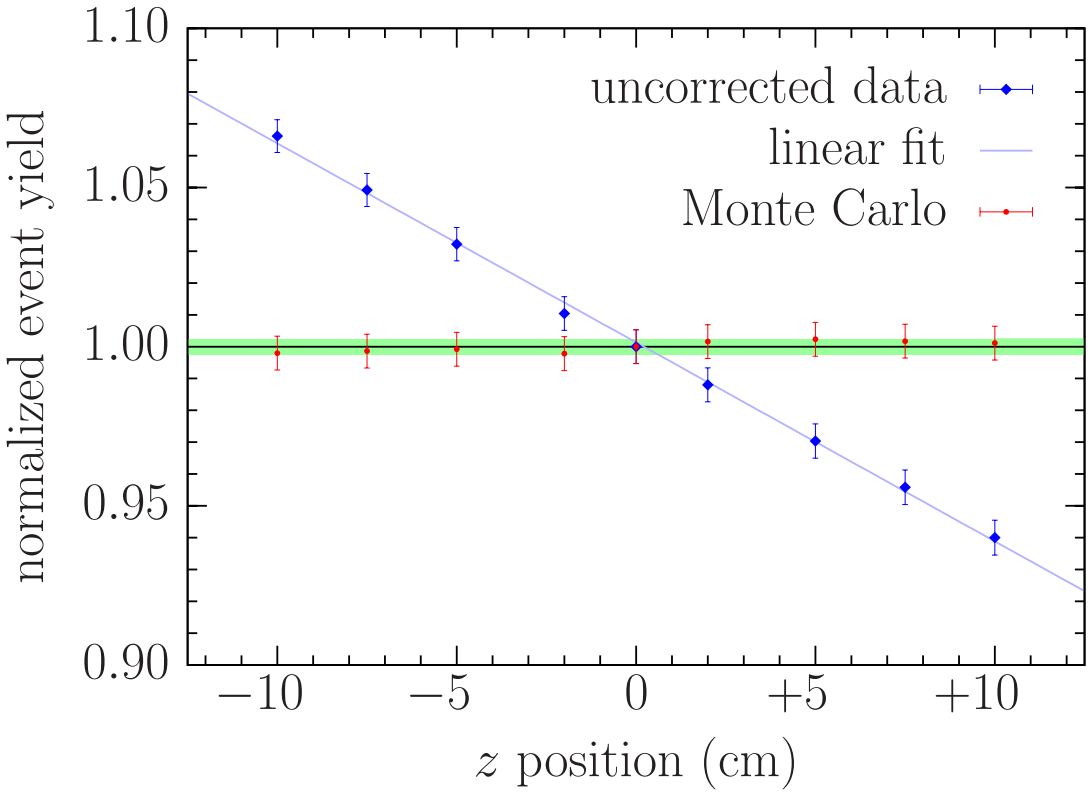

Figure 5.2: (color online). Event yields from carbon foils at different positions along the beam direction, normalized to the yield for the central foil, for the uncorrected data and the Monte Carlo simulation. The dependence of the cross section on the scattering angle, correctly taken into account in the Monte Carlo simulation, introduces a linear trend in the data that needs to be corrected for. All uncertainties are purely statistical.

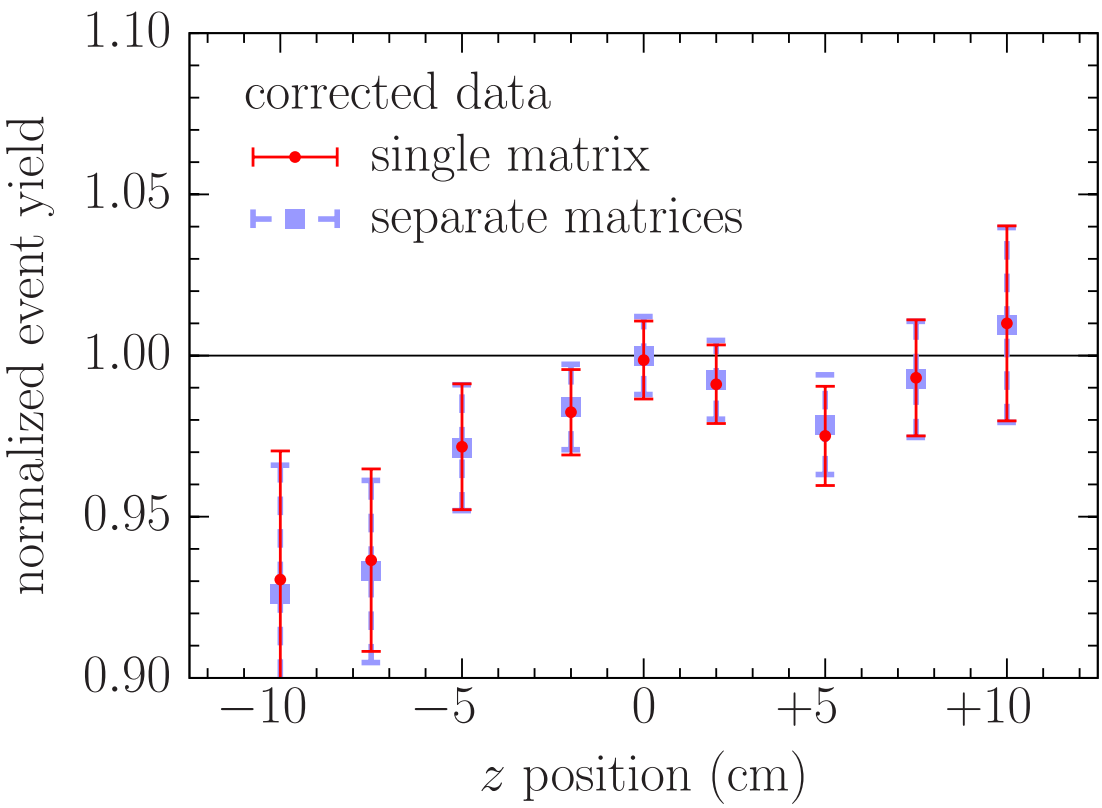

Figure 5.3: (color online). Event yields in the corrected data for the multi-foil carbon target surviving the z-position selection, normalized to the yield for the central foil. The outcomes of two correction procedures are compared. The error bars are symmetric and represent the total uncertainties, being the statistical and systematic uncertainties added in quadrature.

depending on the mean value of the scattering angle. The observed z dependence of the event yields is in a good agreement with a linear function ($\chi^2/\text{NDF} = 0.35$) and a correction is applied to the data. Note that this behavior is absent in the MC event yields (the red dots in Fig. 5.2), because the MC simulation takes into account differences in the acceptance for individual foils. In the data analysis, we relied on the reconstructed target z position to identify events coming from each of the 9 carbon foils, applying the selections represented by the shaded regions in Fig. 5.1. The selected events were then corrected using the acceptance matrix computed at $z = 0$ cm. In order to determine the sensitivity to this approximation, we repeated the same study using 9 different matrices (one for each carbon foil) and found a negligible variation, as shown in Fig 5.3. The obtained event yields are subject to the systematic uncertainties due to the z-position selection applied to identify events coming from individual foils.

As a final remark, we note that to acquire the inclusive data, we varied the momentum settings of the left-arm spectrometer in the MC to determine its effect on the acceptance matrix, and found that it is negligible.

5.4 Uncertainty Analysis

The total systematic uncertainty in this analysis was estimated by adding in quadrature the contributions listed in Table 5.2. Each of the uncertainties was considered completely uncorrelated. We determined the cuts ensuring that there are no dependencies on kinematical variables and, therefore, all the uncertainties affects only the normalization of the extracted cross sections. The kinematical cuts used in the analysis were varied by $\pm 10\%$ or by the resolution of the variable under consideration.

As the obtained results depend on the Monte Carlo calculation, it is important to estimate

Table 5.2: Contributions to systematic uncertainties in the yield-ratio method for aluminum and argon.

	Al	Ar
a. Beam energy	0.1%	0.1%
b. Beam charge	0.3%	0.3%
c. Beam x offset	$< 1.0\%$	$< 0.8\%$
d. Beam y offset	$< 1.0\%$	$< 0.9\%$
e. HRS x offset	$< 0.8\%$	$< 1.0\%$
f. HRS y offset	$< 0.6\%$	$< 0.8\%$
g. Optics (q1, q2, q3)	$< 1.8\%$	$< 1.0\%$
h. Target thickness	0.2%	0.7%
i. Acceptance cut $(\theta, \phi, dp/p)$	$< 1.0\%$	$< 2.4\%$
(i) dp acceptance cut	$< 0.32\%$	-
(ii) θ acceptance cut	$< 0.32\%$	-
(iii) ϕ acceptance cut	$< 0.79\%$	-
(iv) z acceptance cut	$< 0.45\%$	-
j. Calorimeter cut	$< 0.02\%$	$< 0.02\%$
k. Čerenkov cut	$< 0.12\%$	$< 0.07\%$
l. Cross section model	$< 0.2\%$	$< 1.3\%$
m. Radiative and Coulomb corr.	1.0%–1.3%	1.0%–1.3%
Total systematic uncertainty	1.7%–2.7%	1.8%–3.0%

uncertainties resulting from its inputs. To determine the uncertainties related to the target position, we performed the simulation with the inputs for the beam's and spectrometer's x and y offsets varied within uncertainties, and we recomputed the optical transport matrix varying the three quadrupole magnetic fields, one at the time. Each of these runs was compared to the reference run, and the corresponding differences were summed in quadrature to give the total systematic uncertainty due to the Monte Carlo. That summed uncertainty value varied from 1.1 to 2.2%, based on the momentum setting for each of the run, and was the largest single source of systematic error.

The systematic uncertainty due to the cuts on the calorimeter and Čerenkov detector was calculated in a similar way, by varying the cut by a small amount and calculating the

difference with respect to the nominal cut. Given the already high efficiency of these cuts, this resulted in a very small contribution to the uncertainty. The uncertainty due to the acceptance cuts on the angles and on dp/p was calculated in the same way. We included a fixed uncertainty relative to the beam charge and beam energy as in previous work on C and Ti [83].

The measured cross section is also corrected for the effects from internal and external radiative processes. Internal radiative process are vacuum polarization, vertex corrections, and internal bremsstrahlung. External radiative processes refer to electrons losing energy while passing through material in the target. We applied the radiative correction following the recipe of Dasu [94], using the approach of Mo and Tsai [60], which is subject to theoretical uncertainties and depends on the cross-section model. We consider a fixed 1% uncertainty due to the theoretical model for the radiative corrections over the full kinematical range. To account for the cross-section model dependence—the same for both the yield-ratio and acceptance methods—we added an additional uncertainty (fully uncorrelated), estimated by computing the difference in the final double differential cross section when the cross section model is rescaled by $\sqrt{(Q^2)}/2$, Q^2 being the four-momentum transfer squared. Coulomb corrections were included in the local effective momentum approximation, following Ref. [61]. A 10% uncertainty associated with the Coulomb potential was included as systematic uncertainty.

Near the quasielastic peak, there is a non-negligible contribution of the elastic cross section to the inclusive cross section, through the radiative processes. To estimate the corresponding uncertainty, we increased the tail of the elastic contribution by 20%, recalculated the radiative correction, and used its difference with respect to the reference correction as an estimate of the corresponding systematic uncertainty. Finally, we included a target thickness uncertainty.

5.5 Experimental Results

The cross section for inclusive scattering of electrons on the Al-7075 target, extracted using the yield-ratio method and normalized per nucleus, is shown in Fig. 5.4. Its total uncertainties—represented by the outer bands—are obtained by adding in quadrature statistical and systematic uncertainties. As in the case of the previously reported results [83, 92], the aluminum measurement is very precise and limited by the systematic uncertainties.

As a cross check, we also extracted the Al cross section using the acceptance method. Figure 5.5 shows that the results obtained using the two methods are in good agreement. Note

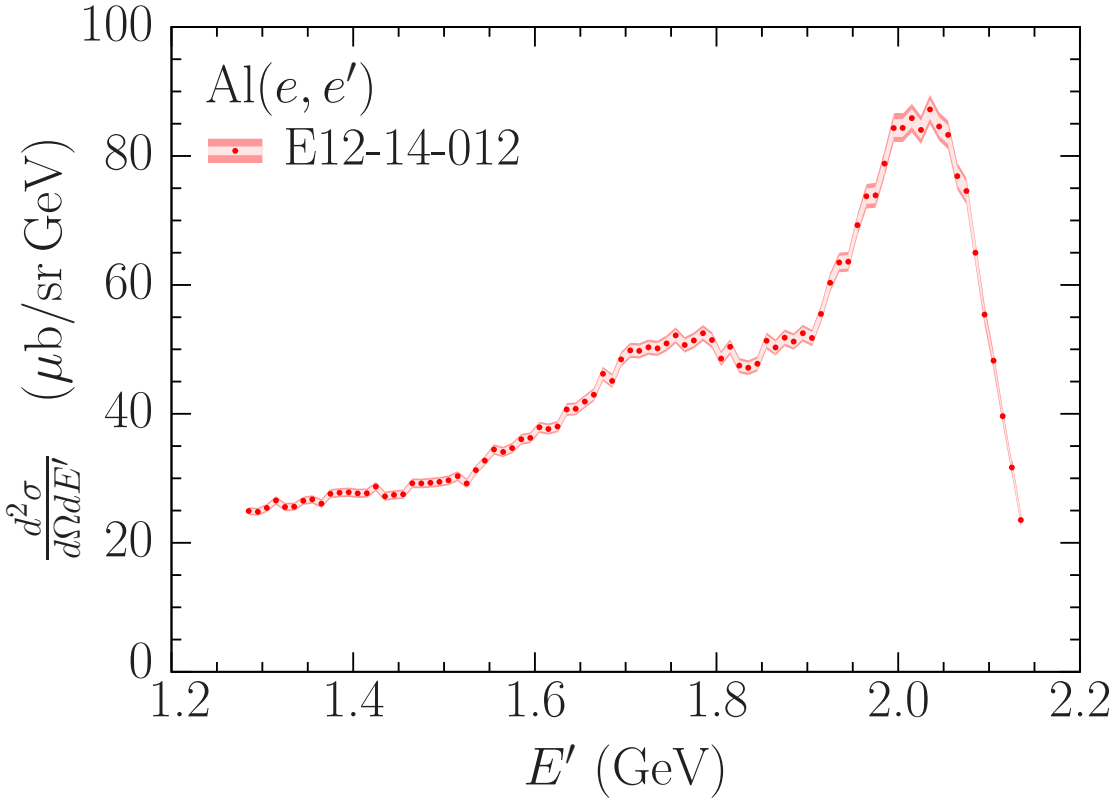

Figure 5.4: (color online). Double-differential cross section extracted for inclusive electron scattering off the Al-7075 target at beam energy 2.222 GeV and scattering angle 15.54°. The inner and outer uncertainty bands correspond to statistical and total uncertainties, respectively.

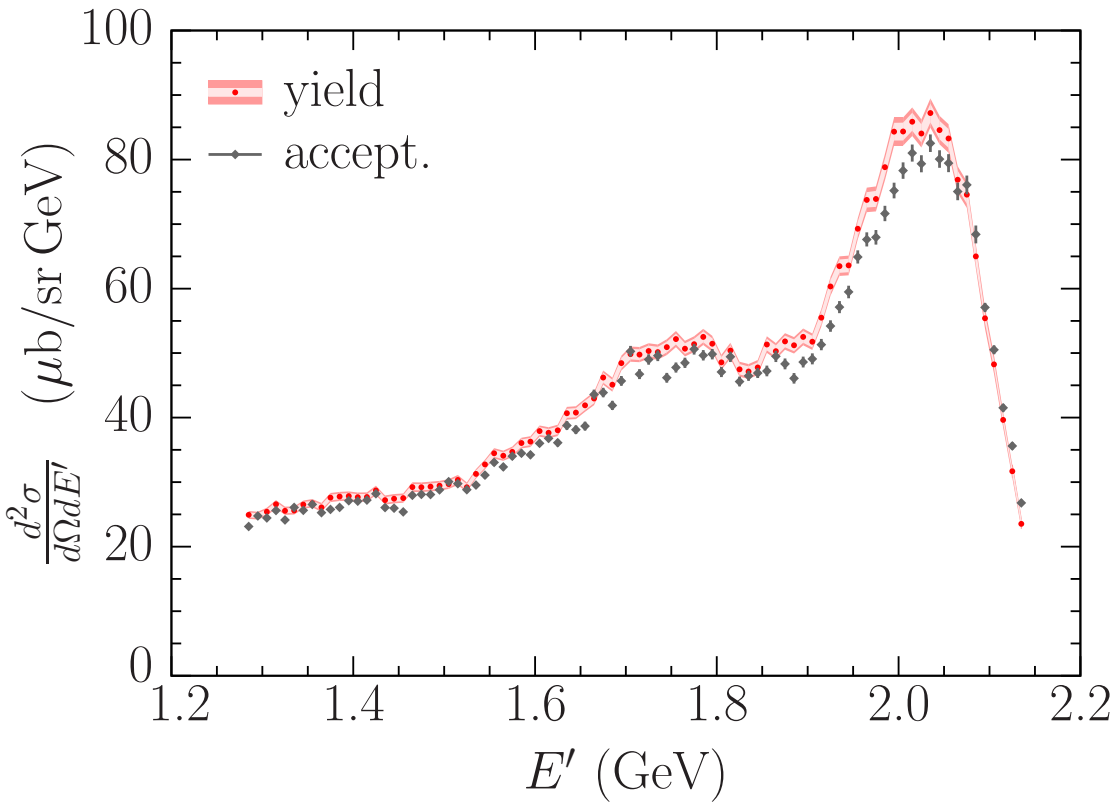

Figure 5.5: (color online). Comparison of the Al(e, e') cross sections extracted using the yield-ratio and acceptance methods. The inner (outer) bands for the yield-method show statistical (total) uncertainties. For the acceptance method only statistical uncertainties are shown.

that in the acceptance method we did not estimate systematic uncertainties, the error bars represent the statistical uncertainties only.

The agreement between the yield-ratio and acceptance results was observed for the carbon, aluminum, titanium, and argon targets and provides validation for the approximation employed in the acceptance method, namely using a single acceptance matrix computed at $z = 0$ cm, as explained in Sec. 5.3.2. The consistency between the yield and acceptance methods for all analyzed targets also indicates that the yield-ratio result exhibits only weak dependence on the input cross section used in the Monte Carlo simulation to correct the data for efficiency and acceptance. This issue is particularly important in the case of the titanium and argon targets, where the cross-section simulations cannot be validated against existing data. Note that the radiative corrections applied in both methods are the same and do depend on the input cross section. The related uncertainties are discussed in Sec. 5.4.

To illustrate how nuclear effects affect different interaction channels, in Fig. 5.6 we compare the per-nucleon cross sections for aluminum, argon, titanium, and carbon. While for every target we account for the abundances of naturally occurring isotopes [93], this effect is relevant only for the Al target. It is a consequence of the non-negligible contributions of elements heavier than $^{27}_{13}$Al to the Al-7075 alloy, detailed in Table 5.1. At the considered kinematics, corresponding to the beam energy 2.222 GeV and scattering angle 15.54°, the cross sections per nucleon for targets ranging from carbon ($A = 12.01$) to titanium ($A = 47.92$) turn out to be in very good agreement in the region where different pion production mechanisms dominate. While this finding is by no means obvious—due to asymmetry of the proton and neutron numbers for aluminum, argon, and titanium—it is consistent with the results of Refs. [65, 66] at energies ∼0.54–1.50 GeV and scattering angles ∼37°.

The influence of nuclear effects on QE interactions can be better illustrated in terms of the cross sections normalized to the elementary contributions of neutrons and protons that

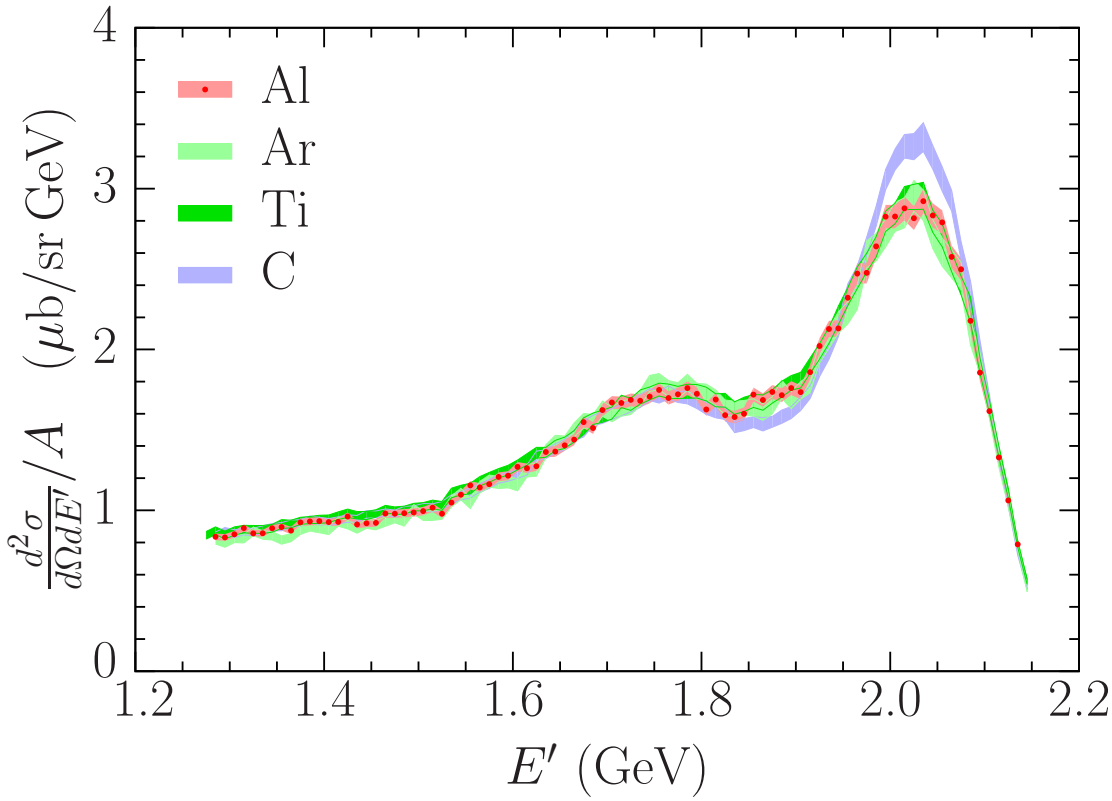

Figure 5.6: (color online). Comparison of the cross sections per nucleon for aluminum, argon [92], titanium [83], and carbon [83] measured at beam energy 2.222 GeV and scattering angle 15.54°. The average nucleon number for every target is calculated according to the natural abundances of isotopes, see details in the text. The bands represent the total uncertainties.

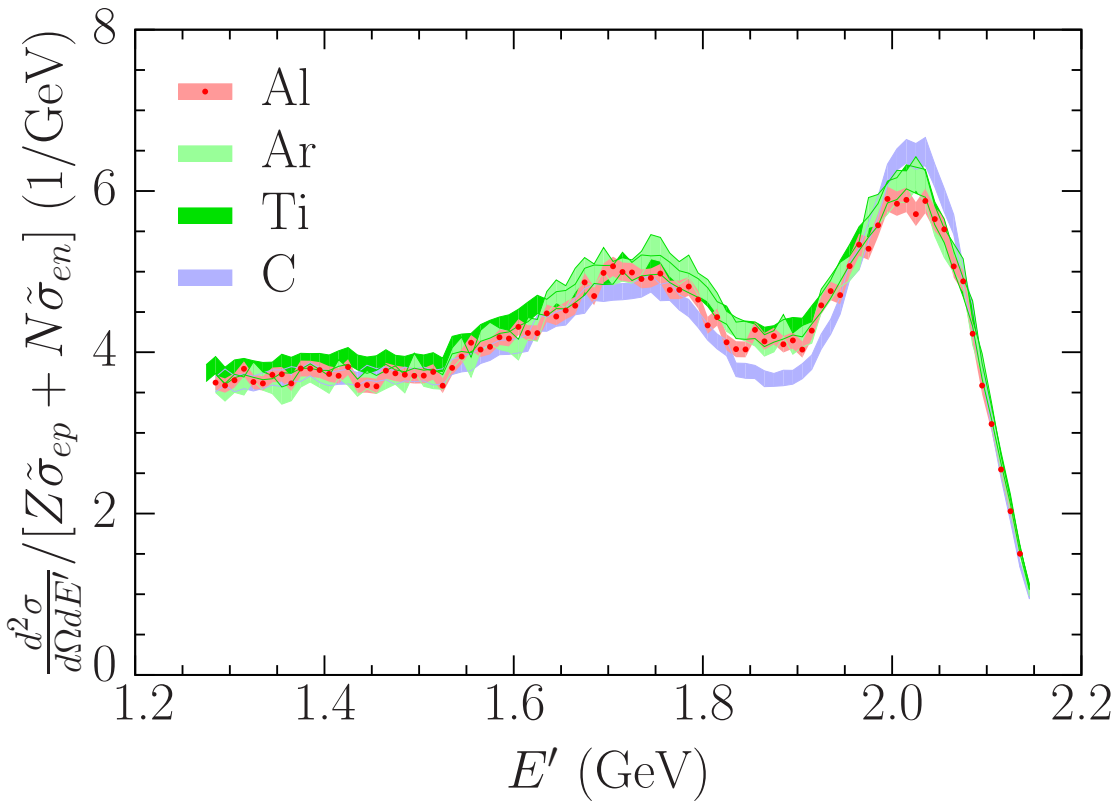

Figure 5.7: (color online). Same as in Fig. 5.6 but for the cross sections normalized by the combination of the elementary cross sections according to Eq. (5.6).

compose the nucleus, that is the quantity

$$\frac{d^2\sigma}{d\Omega dE'}/[Z\tilde{\sigma}_{ep} + N\tilde{\sigma}_{en}], \tag{5.6}$$

where Z and N are the proton and neutron numbers, respectively, while $\tilde{\sigma}_{ep}$ and $\tilde{\sigma}_{en}$ denote the elastic electron-proton and electron-neutron cross sections stripped of the energy-conserving delta function [86]. In the following, we use the average neutron numbers calculated according to the natural abundances of isotopes, that is 6.01 for carbon, 21.98 for argon, and 25.92 for titanium [93]. For the aluminum target, we employ $Z = 14.26$ and $N = 15.58$, due to its composition listed in Table 5.1.

As shown in Fig. 5.7, the results for titanium and argon are, within uncertainties, identical in the QE peak, but they differ from both those for carbon and aluminum. Near the maximum of the QE peak, the cross section defined in Eq. (5.6) is lower by ∼4% for aluminum, and higher by ∼5% for carbon, than the ones for argon and titanium. In the dip region, the results for aluminum (carbon) are lower by ∼2% (∼13%) compared with those for argon and titanium.

In QE scattering, the cross sections normalized according to Eq. (5.6) exhibit very weak target dependence only in the region of high E', corresponding to low energy transfers, as shown in Fig. 5.7. This is, however, not the case in the QE peak's maximum and for lower E', where the energy transferred by electrons to the nucleus is sufficiently high to probe deeply bound states and also to induce two-nucleon knockout.

The observed differences in the dependence on the atomic number of various interaction mechanisms—previously reported in Refs. [66, 95, 96]—can be expected to provide important clues for building models of nuclear effects valid over broad kinematic regimes and able to describe a range of targets. Such models are of great importance to long-baseline neutrino-

oscillation experiments.

5.6 Scaling and A-dependence

The scaling analysis allows to compare inclusive electron-scattering data taken in different kinematical conditions and using different targets.

Scaling of first kind, or y-scaling, is observed in the kinematical region of large momentum transfer, $|\mathbf{q}|$, and energy transfer $\omega < \sqrt{|\mathbf{q}|^2 + m^2} - m$, in which the beam particle interacts with individual nucleons and the dominant reaction mechanism is quasielastic scattering [63, 64]. Under these conditions, the target response, which in general depends on both momentum and energy transfers, reduces to a function of the single variable $y = y(|\mathbf{q}|, \omega)$, defined by the equation

$$\begin{aligned} \omega + M_A = &\sqrt{y^2 + (M_A - m + E_{\min})^2} \\ &+ \sqrt{(y + |\mathbf{q}|)^2 + m^2}. \end{aligned} \tag{5.7}$$

Here, m and M_A are the nucleon mass and the mass of the target nucleus, respectively, while $E_{\min}$ denotes the nucleon knockout threshold. The scaling variable y, having the dimension of energy, is simply related to the longitudinal component of the initial momentum of the struck nucleon, $k_{\parallel} = \mathbf{k} \cdot \mathbf{q}/|\mathbf{k}|$. The scaling function $F(y)$ is determined from the measured cross section, σ^{exp} through

$$F(y) = K \frac{\sigma^{\text{exp}}}{Z\tilde{\sigma}_{ep} + N\tilde{\sigma}_{en}}, \tag{5.8}$$

with K a kinematic factor.

In Fig. 5.8, the y-scaling function of aluminum, computed using the cross section displayed in Fig. 5.4 and the average proton and neutron numbers from Table 5.1, is compared to those

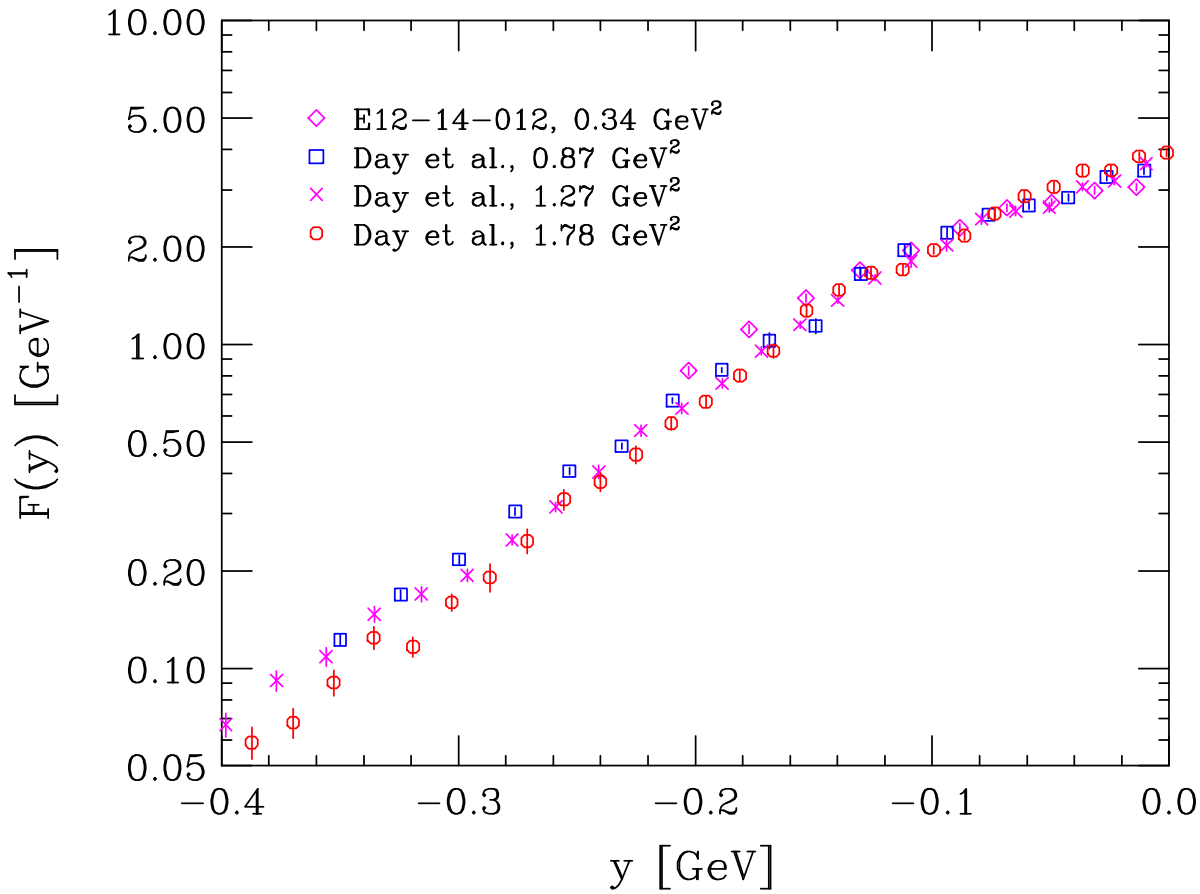

Figure 5.8: (color online) Comparison between the scaling function of aluminum obtained from the E12-14-012 data (this work), represented by diamonds, and those obtained from the data of Day *et al.* [67]. The data are labeled according to the value of Q^2 corresponding to quasi elastic kinematics.

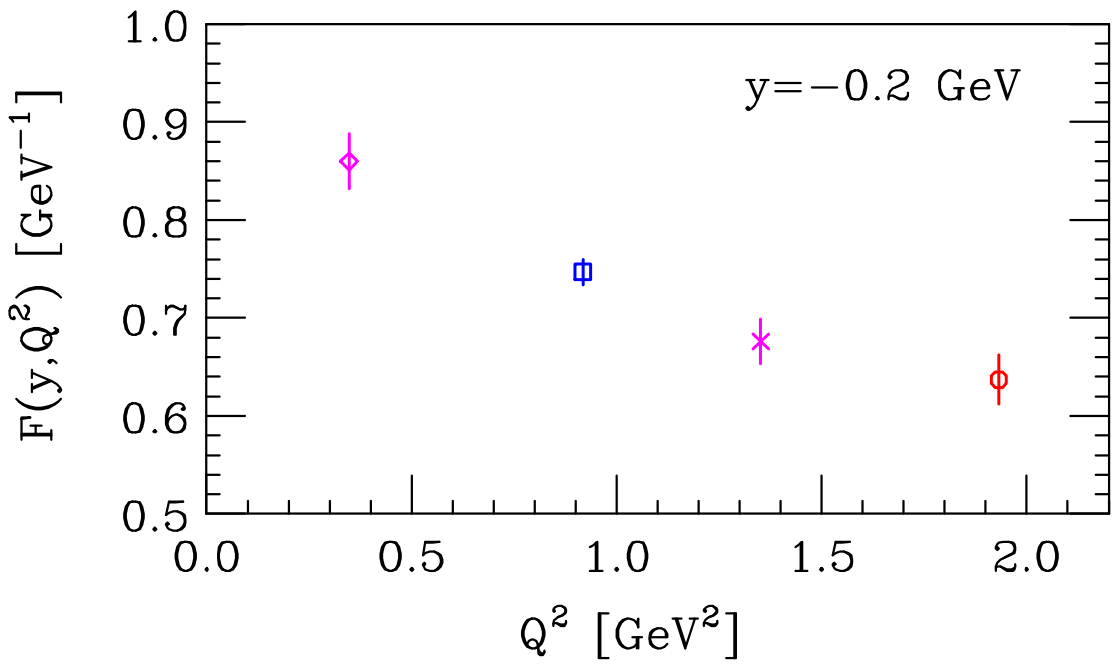

Figure 5.9: (color online) Q^2-dependence of the scaling functions $F(y, Q^2)$ obtained from the cross section displayed in Fig. 5.4 and from the data reported in Ref. [67]. The meaning of the symbols is the same as in Fig. 5.8.

obtained from the data of Day *et al* [67] using a $^{27}_{13}$Al target. The cross sections of Ref. [67] have been measured at fixed beam energy $E = 3.595$ GeV and scattering angle 16, 20 and 25 deg, with the values of Q^2 corresponding to quasi elastic kinematics being 0.87, 1.27 and 1.78 GeV^2, respectively.

Scaling behavior is clearly observed at $y \approx 0$, corresponding to region of the quasifree peak, or $\omega \approx Q^2/2m$. The sizeable scaling violations occurring at larger negative values of y are mainly to be ascribed to the effects of FSI between the knocked-out nucleon and the spectator particles. This feature is illustrated in Fig. 5.9, showing the Q^2-dependence of the scaling function $F(y, Q^2)$ at fixed $y = -0.2$ GeV. The approach to the scaling limit from above is a clear signature of FSI.

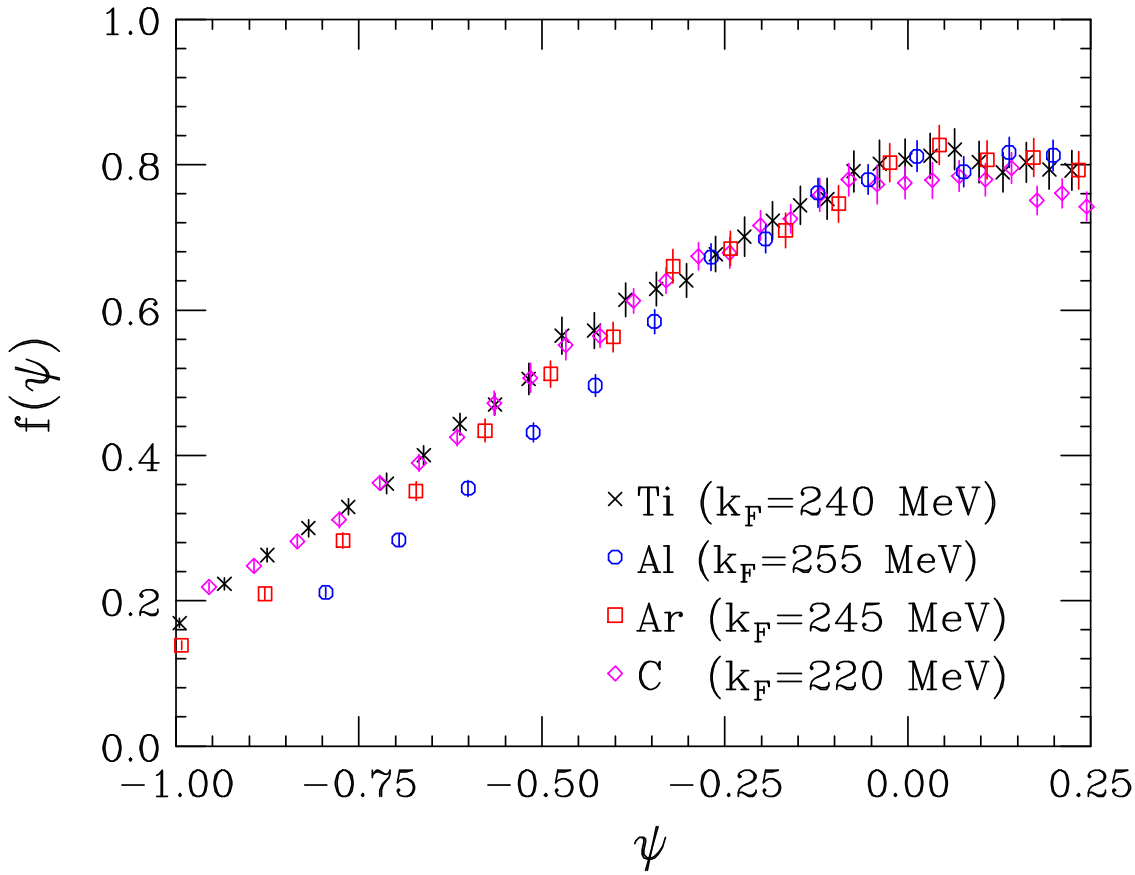

Figure 5.10: (color online) Scaling functions of second kind, obtained from the inclusive cross sections measured by the E12-14-012 experiment using carbon, aluminum, argon and titanium targets.

A more general form of scaling, dubbed scaling of second kind, permits a global analysis, combining data corresponding to different targets [74]. The definitions of the dimensionless scaling variable, ψ, and scaling function, $f(\psi)$, involve a momentum scale, loosely referred to as nuclear Fermi momentum, providing a parametrization of the target-mass dependence of the measured cross sections.

Figure 5.10 illustrates the scaling functions obtained from the inclusive cross sections measured by the E12-14-012 experiment using carbon, aluminum, argon and titanium targets.

The results shows that setting the carbon Fermi momentum to the value obtained from the independent analysis of Moniz *et al.* [75], $k_F = 220$ MeV, scaling of the second kind is shown when k_F values of 255, 245, and 240 MeV are taken for Al, Ar, and Ti respectively.

A different approach to describe the A-dependence of the nuclear inclusive cross section, inspired by the considerations underlying the local density approximation of the nucleus [97], has been proposed by the authors of Ref. [98]. Their analysis—aimed at obtaining the inclusive cross section per nucleon of isospin-symmetric nuclear matter from an extrapolation of the available data—shows that the ^{12}C, ^{27}Al, ^{56}Fe, and ^{197}Au cross sections at Q^2 ranging between 0.25 and 2.70 GeV^2 exhibit a striking linear behavior when plotted as a function of $A^{-1/3}$. The extension of this study to the data set collected by the E12-14-012 experiment is under way, and the results will be discussed elsewhere.

5.7 Summary and Conclusions

We have reported on the measurements of the cross sections for inclusive electron scattering over a broad range of energy transfers, extending from the particle-emission threshold to above the excitation of the first hadronic resonance. These high precision data were taken at Jefferson Lab in Hall A for a beam energy of $E = 2.222$ GeV and electron scattering angle $\theta = 15.54°$ from four nuclear targets: carbon, aluminum, argon, and titanium. The reported results give unique opportunity to validate nuclear models employed in Monte Carlo simulations of precise long-baseline neutrino-oscillation experiments, and to assess their contribution to uncertainties of the oscillation analysis in a rigorous manner.

We find (see Fig. 5.6) that the per-nucleon responses for the considered four targets are strikingly similar over the entire energy transfer range ($0.05 < \omega < 0.90$ GeV), save at the maximum of the quasielastic peak and the dip region. At the kinematics from the maximum

of the quasielastic peak to the onset of the Δ resonance, the result for carbon stands apart from those for aluminum, argon, and titanium. This finding shows that the momentum and energy distribution of nucleons in the nuclear ground state and final-state interactions—inducing the 'Doppler' broadening of the scattered electron's final energy—in carbon is not as pronounced as for the heavier nuclei. When accounting is made for the number of protons and neutrons in each nucleus, this feature does not disappear, as can be seen in Fig. 5.7.

When the aluminum data set along with higher Q^2 data from SLAC are presented in terms of the y-scaling analysis (Fig. 5.8) the set behaves as expected, and the scaling behavior is clearly observed at the kinematics corresponding to the quasi-free peak. While in the absence of FSI, the scaling function $F(y)$ is expected to converge from below with increasing Q^2, the effect of FSI—falling with Q^2—leads it to converge from above. These new data fit this pattern (Fig. 5.9).

Taken together this data set will allow us to predict the electromagnetic nuclear responses for nuclei between $A = 12$ and 48 by interpolation as a function of $A^{-1/3}$. Of particular interest will be oxygen, as water serves as the target and radiator in the large Čerenkov detector of T2K [90], and chlorine, as polyvinyl chloride composes the detectors of NOvA [99].

Chapter 6

Summary

The JLab E12-14-012 experiment performed a high precision measurement of the (e,e′) and (e,e′p) cross sections for a variety of targets, including argon, titanium, aluminum and carbon targets. In this thesis, after briefly reviewed the basic theory on neutrino oscillation and the experimental setup, we presented the results of the inclusive (e,e′) cross sections for argon, titanium, aluminum and carbon targets at a beam energy of 2.222 GeV and scattering angle of 15.54°. The inclusive kinematics cover a wide range of energy transfers, which include deep inelastic scattering, delta production, and quasielastic scattering. Our results are in good agreement with previous data sets and they have total uncertainties less than 5% over the entire kinematic range. Our results represent also the first and most precise measurements of the (e,e′) inclusive cross sections for argon and titanium. The results for the exclusive (e,e′p) cross sections are expected in the near future.

In the upcoming deep underground neutrino experiment (DUNE), Liquid Argon Time Projection Chambers (LArTPCs) will be used as the detector technology, and argon will be the neutrino target. The high precision electron-argon scattering data collected by the E12-14-012 experiment will allow for a detailed description of the argon nuclear structure, which will be important for developing a theory model for neutrino-nucleus interaction. In addition, with a more accurate theory model, the neutrino energy can be reconstructed more precisely and hence the uncertainties of the extracted oscillation parameters can be effectively reduced.

Bibliography

[1] S.L. Glashow, Nucl. Phys. **22**, 579 (1961).

[2] S. Weinberg, Phys. Rev. Lett. **19**, 1264 (1967).

[3] B. Pontecorvo, Sov. Phys. **JETP6**, 429 (1958).

[4] Z. Maki, M. Nakagawa, S. Sakata, Prog. Theor. Phys. **28**, 870 (1962).

[5] O. Benhar, N. Rocco, Adv. High. Energy. Phys. 2013, 912702 (2013).

[6] V.M. Lobashev, Nucl. Phys. A **719**, 153 (2003).

[7] T. Katori, M. Martini, J. Phys. G**45**, 1 (2016) arXiv:1611.07770 [hep-ph].

[8] F. Capozzi *et al.*, Prog. Part. Nucl. Phys. **102**, 48 (2018).

[9] URL https://www.dunescience.org.

[10] B. Abi *et al.*, arXiv preprint arXiv:1807.10334 (2018).

[11] A. Corey *et al.*, (DUNE Collaboration), arXiv preprint arXiv:1307.7335 (2013).

[12] T. de Forest, J.D. Walecka, Adv. Phys. **15**, 1 (1966).

[13] J. Gao, Ph.d. thesis, (1999).

[14] J. Mougey *et al.*, Nucl. Phys. A **262**, 461 (1976).

[15] URL https://hallaweb.jlab.org/photos/2015/Hall%20A/2_011.jpg.

[16] A. Himmel. Talk at FNAL, (2018).

[17] J. Alcorn *et al.*, Nucl. Instrum. Meth. A**522**, 294 (2004).

[18] O. Benhar, *et al.* (The Jefferson Lab E12-14-012 Collaboration), arXiv:1406.4080 [nucl-ex].

[19] W Barry *et al. JLab-TN-91-087*, (1991).

[20] WC Barry, JW Heefner, GS Jones, JE Perry, and R Rossmanith. Beam position measurement in the cebaf recirculating linacs by use of pseudorandom pulse sequences. Technical report, (1990).

[21] E Cisbani *et al.* Nucl. Instrum. Meth. A **496**, 305, (2003).

[22] K. G. Fissum *et al.*, Nucl. Instrum. Meth. A **474**, 108 (2001). doi:10.1016/S0168-9002(01)00875-0

[23] Dan Green. *High Pt physics at hadron colliders* **22**. Cambridge University Press, (2005).

[24] Joaquín López Herraiz. Study of the (e, e'p) quasi-elastic reaction in complex nuclei: theory and experiment. Technical report, Thomas Jefferson National Accelerator Facility, Newport News, VA (United States), (2010).

[25] Mo Iodice *et al.*, Nucl. Instrum. Meth. A **411**, 108 (1998).

[26] G. Petratos et al. Jlab experiment e12-10-103, (2010).

[27] SN. Santiesteban *et al.*, Nucl. Instrum. Meth. A (2001).

[28] K. Unser, *IEEE Transactions on Nuclear Science*, 28(3):2344–2346, (1981).

[29] Y. Zhihong, Ph.d. thesis. (2013).

[30] O. Benhar, P. Huber, C. Mariani and D. Meloni, Phys. Rept. **700**, 1 (2017).

[31] M. Antonello *et al.* (MicroBooNE, LAr1-ND, and ICARUS-WA104 Collaborations), arXiv:1503.01520 [physics.ins-det].

[32] R. Acciari *et al.* (DUNE Collaboration), arXiv:1512.06148 [physics.ins-det].

[33] K. Abe *et al.* (T2K Collaboration), Phys. Rev. D **88**, 032002 (2013).

[34] A. M. Ankowski *et al.*, Phys. Rev. D **92**, no. 7, 073014 (2015).

[35] M. Anghinolfi *et al.*, J. Phys. G**21**, L9 (1995).

[36] O. Benhar, Nucl. Phys. News **26**, 15 (2016).

[37] S. Frullani and J. Mougey, Adv. Nucl. Phys. **14**, 1 (1984).

[38] A. E. L. Dieperink and P. K. A. de Witt Huberts, Ann. Rev. Nucl. Part. Sci. **40**, 239 (1990).

[39] S. Boffi, C. Giusti, F. D. Pacati, Phys. Rept. **226**, 1 (1993).

[40] O. Benhar, N. Farina, H. Nakamura, M. Sakuda and R. Seki, Phys. Rev. D **72**, 053005 (2005).

[41] O. Benhar, D. Day, I. Sick, Rev. Mod. Phys. **80**, 189 (2008).

[42] A. M. Ankowski, O. Benhar, M. Sakuda, Phys. Rev. D **91**, 054616 (2015).

[43] N. Rocco, A. Lovato, O. Benhar, Phys. Rev. Lett. **116**, 192501 (2016).

[44] O. Benhar and D. Meloni, Nucl. Phys. A **789**, 379 (2007).

[45] O. Benhar, P. Coletti, and D. Meloni, Phys. Rev. Lett. **105**, 132301 (2010).

[46] O. Benhar and G. Veneziano, Phys. Lett. B **702**, 433 (2011).

[47] E. Vagnoni, O. Benhar, and D. Meloni, Phys. Rev. Lett. **118**, 142502 (2017).

[48] A. Lovato, S. Gandolfi, J. Carlson, S. C. Pieper and R. Schiavilla, Phys. Rev. Lett. **117**, 082501 (2016).

[49] A. Meucci and C. Giusti, Phys. Rev. D**89**, 117301 (2014).

[50] O. Lalakulich, U. Mosel and K. Gallmeister, Phys. Rev. C**86**, 054606 (2012).

[51] J. Nieves, F. Sanchez, I. Ruiz Simo and M. J. Vicente Vacas, Phys. Rev. D**85**, 113008 (2012).

[52] M. Martini, M. Ericson, G. Chanfray and J. Marteau, Phys. Rev. C**81**, 045502 (2010).

[53] V. Pandey, N. Jachowicz, T. Van Cuyck, J. Ryckebusch and M. Martini, Phys. Rev. C**92**, 024606 (2015).

[54] G. D. Megias, J. E. Amaro, M. B. Barbaro, J. A. Caballero, T. W. Donnelly and I. Ruiz Simo, Phys. Rev. D**94**, 093004 (2016).

[55] J. Heisenberg, J. S. Mccarthy and I. Sick, Nucl. Phys. A**164**, 353 (1971).

[56] A. M. Selig, C. De Vries, P. K. A. De Witt Huberts and I. E. Zacharov, Nucl. Phys. A**476**, 413 (1988).

[57] E. F. Romberg, N. S. Wall, D. Blum, J. W. Lightbody and S. Penner, Nucl. Phys. A**173**, 124 (1971).

[58] J. Arrington *et al.*, Phys. Rev. Lett. **82**, 2056 (1999).

[59] Hall C Collaboration, paper in preparation

[60] MO. L. W. and TSAI, Y. S., Rev. Mod. Phys. **41**, 205 (1969).

[61] A. Aste, C. von Arx, and D. Trautmann, Eur. Phys. J. **A26**, 167 (2005).

[62] O. Benhar, D. B. Day, and I. Sick, arXiv:0603032 [nucl-ex]. http://faculty.virginia.edu/qes-archive/index.html

[63] I. Sick, D. B. Day, and J. S McCarthy, Phys. Rev. Lett. **45** , 871 (1980).

[64] D. B. Day, J. S. McCarthy, T. W. Donnelly and I. Sick, Ann. Rev. Nucl. Part. Sci. **40**, 357 (1990).

[65] J. S. O'Connell *et al.*, Phys. Rev. C **35**, 1063 (1987).

[66] R. M. Sealock *et al*, Phys. Rev. Lett. **62** (1989) 1350.

[67] D. B. Day *et al.*, Phys. Rev. C **48**, 1849 (1993).

[68] V. Tvaskis, PhD Thesis, Vrije Universiteit, Amsterdam, 2004.

[69] K. Abe *et al.* (T2K Collaboration), Nucl. Instrum. Meth, A659, 106 (2011).

[70] P. Adamson *et al.* (NOvA Collaboration), Phys. Rev. Lett. **118**, no. 23, 231801 (2017).

[71] L. Ren *et al.* (MINERvA Collaboration), Phys. Rev. D **95**, 072009 (2017).

[72] O. Benhar, A. Fabrocini, S. Fantoni, G. A. Miller, V. R. Pandharipande, and I. Sick, Phys. Rev. C **44**, 2328 (1991).

[73] O. Benhar and F. Coppini, paper in preparation.

[74] T.W. Donnelly and I. Sick,, Phys. Rev. C **60**, 065502 (1999).

[75] E.J. Moniz *et al*, Phys. Rev. Lett. **26**, 445 (1971).

[76] B. Abi *et al.* (DUNE Collaboration), arXiv:1807.10334 [physics.ins-det].

[77] A. A. Aguilar-Arevalo *et al.* (MiniBooNE Collaboration), arXiv:1805.12028 [hep-ex].

[78] A. M. Ankowski, P. Coloma, P. Huber, C. Mariani, and E. Vagnoni, Phys. Rev. D **92**, 091301 (2015).

[79] K. Abe *et al.* (T2K Collaboration), Phys. Rev. Lett. **118**, 151801 (2017).

[80] M. .A. Acero (NovA Collaboration), Phys. Rev. D **98**, 032012 (2018).

[81] L. Alvarez-Ruso *et al.*, Prog. Part. Nucl. Phys. **100**, 1 (2018).

[82] A. M. Ankowski, and C. Mariani, J. Phys. G **44**, 054001 (2017).

[83] H. Dai, *et al.*, (The Jefferson Lab Hall A Collaboration), Phys. Rev. C**98**, 014617 (2018).

[84] In 2016, the Quadrupole magnet closest to the target (Q1) was replaced with a normal conducting quad, with similar magnetic properties.

[85] A. Meucci, F. Capuzzi, C. Giusti and F. D. Pacati, Phys. Rev. C **67**, 054601 (2003).

[86] T. de Forest, Nucl. Phys. **A392**, 232 (1983).

[87] S. Boffi, C. Giusti, F. D. Pacati, and M. Radici, *Electromagnetic Response of Atomic Nuclei* (Clarendon, Oxford, UK, 1996).

[88] P. K. A. de Witt Huberts, J. Phys. G **16**, 507 (1990).

[89] D. Rohe *et al.*, Phys. Rev. Lett. **93**, 182501 (2004).

[90] K. Abe *et al.* (T2K Collaboration), Phys. Rev. Lett. **121**, 171802 (2018).

[91] K. Abe *et al.* (Hyper-Kamiokande Proto-Collaboration), Prog. Theor. Exp. Phys. **2015**, 053C02 (2015).

[92] H. Dai *et al.* (Jefferson Lab Hall A Collaboration), Phys. Rev. C **99**, 054608 (2019).

[93] J. K. Tuli, Nuclear Wallet Cards, https://www.nndc.bnl.gov/wallet, 2011.

[94] S. R. Dasu, Precision Measurement of x, Q^2, and A-dependence of $R = \sigma_L/\sigma_T$ and F_2 in deep inelastic scattering, Ph.D. thesis, University of Rochester, 1988.

[95] J. S. O'Connell *et al.*, Phys. Rev. Lett. **53**, 1627 (1984).

[96] D. T. Baran *et al.*, Phys. Rev. Lett. **61**, 400 (1988).

[97] A. N. Antonov and I. Zh. Petkov, Nuovo Cimento A **94**, 68 (1986).

[98] D. B. Day *et al.*, Phys. Rev. C **40**, 1011 (1989).

[99] R. L. Talaga, J. J. Grudzinski, S. Phan-Budd, A. Pla-Dalmau, J. E. Fagan, C. Grozis, and K. M. Kephart, Nucl. Instrum. Meth. A **861**, 77 (2017).